IOWA STATE UNIVERSITY
Digital Repository

2013

Nightmare from which you will never awake: Electronic to vibrational spectra

Nuwan De Silva
Iowa State University

Follow this and additional works at: https://lib.dr.iastate.edu/etd

Part of the Physical Chemistry Commons

Nightmare from which you will never awake: Electronic to vibrational spectra

By

Nuwan De Silva

A dissertation submitted to the graduate faculty

in partial fulfillment of the requirements for the degree of

DOCTOR OF PHILOSOPHY

Major: Physical Chemistry

Program of Study Committee:
Mark S. Gordon, Major Professor
Theresa L. Windus
Thomas A. Holme
Emily A. Smith
Monica H. Lamm

Iowa State University

Ames, Iowa

2013

DEDICATION

This work is dedicated to my wife Chamila, daughter Amelia, and son Jaden.

TABLE OF CONTENTS

ACKNOWLEDGMENTS

I would like to express my utmost gratitude to my research advisor, **Professor Mark Gordon**, for his noble support and valuable advice during my research. Professor Gordon's mentorship has exposed me to a broad range of research topics and has also bestowed upon me many invaluable research experiences and skills. Professor Gordon has not only encouraged me to grow as a productive chemist but he has also emphasized the importance of becoming an independent thinker. His hard work and passionate attitude towards his research has been very inspirational to me. I have been amazingly fortunate and grateful to have Professor Mark Gordon as my research advisor.

I thank my program of study committee members for their guidance over the years. I appreciate their constructive comments throughout my graduate adventures at Iowa State University. I would like to thank **Professor Theresa Windus** for all the support she has given me since the beginning of my graduate studies. I really appreciate her willingness to answer questions, clarify the subject matter and helped me to understand many quantum mechanical concepts during her class. I am very grateful to **Professor Thomas Holme**, for his insightful comments and many motivating discussions. I thank **Professor Emily Smith** for adding an experimental perspective towards my research and her encouragement through out the years. I also thank **Professor Monica Lamm** for sharing her knowledge on macro systems, which has help me to visualize the applicability of my work in the real world.

I am thankful to **Professor Klaus Reudenberg** for sharing his lectures. I am especially grateful to **Dr. Mike Schmidt**, for his guidance, understanding, patience, and answering of my many questions.

I would like to thank **Dr. Sarom Leang**, **Dr. Luke Roskop**, and **Dr. Spencer Pruitt** who have been faithful friends over the last few years. They made sure that I would be graduating on time. My work has greatly benefited from their suggestions, encouragement, and humor.

In addition, I am very privileged and thankful to have collaborated with **Dr. Soohaeng Willow**, **Dr. Bosiljka Njegic**, **Dr. Noriyuki Minezawa**, and **Professor Michael Collins**. I also gratefully acknowledge **Professor Lyudmila Slipchenko**, and **Dr. Federico Zahariev**, along with the rest of my fellow Gordon Group members for their support.

I also thank to the administrative staff, **Michelle Duncalf**, **Renee Harris**, and **Lynette Edsall**, for their continued assistance in navigating through the paper work.

I owe my deepest gratitude to my masters research advisor, **Professor Titus Albu**, for the tremendous support and continued encouragement. I also like to thank **Professor Scott Northrup**, **Professor Daniel Swartling**, **Professor David Crouse**,

Professor Jisook Kim, Professor Jeffrey Boles, and Professor Edward Lisic at Tennessee Tech University for the role they have played during my academic journey. I thank my undergraduate advisors, Professor Nalin De Silva and Professor Rohini De Silva at University of Colombo for encouraging me towards the path of graduate school.

I also thank Professor Krishna Kumar, Katie Kumar, Professor James Cornette, and Carolyn Cornette for their encouraging guidance. I gratefully thank to friends, Marilee Hall and Kumari Rannulu, relative, Somasiri De Silva, my sister, Dilusha De Silva, and my high school teacher, Mahanama Hiniduma who are very inspirational to my life in many ways.

I thank my parents, Dhanasiri De Silva and Sumithra Perera, my mother-in-law Srimathi Liyanage, and grandmother, Charlotte Premalatha for their blessings.

Finally, I thank my wife, Chamila. Despite her own graduate studies, her support, encouragement, and unwavering love is undeniably the driving force behind my pursuit of graduate studies. I praise my daughter, Amelia and son Jaden, for inspiring and amazing me every day.

CHAPTER 1. GENERAL INTRODUCTION

General Overview

Over the span of last few decades, electronic structure methods have emerged as a viable and powerful approach to quantum mechanics. The recognition of electronic structure methods in the field of chemistry was highlighted by Nobel Prize awardees Walter Kohn and the late Sir John A. Pople in 1998 for the development of computational methods in quantum chemistry. Since then, the quantum chemistry field is continually growing with tremendous advances in theory and algorithmic methods, as well as the exponential increase in available computing power. Quantum chemistry offers the real promise of being able to complement experimental work as a means to uncover and explore new chemistry.

Dissertation Organization

This dissertation is comprised of seven chapters: Chapter 1 provides the theoretical background of *ab initio* methods and density functional theory, which are relevant to the computational methodologies presented in the following chapters. Chapter 2 examines the anharmonicity associated with weakly bound metal cation dihydrogen complexes using the vibrational self-consistent field (VSCF) method and characterizes the interaction between a hydrogen molecule and a metal cation. Chapter 3 illustrates a

study of molecular hydrogen clustering around the lithium cation and their accompanied vibrational anharmonicity employing VSCF. Chapter 4 provides a qualitative interpretation of solvent-induced shifts of amides and simulated electronic absorption spectra using the combined time-dependent density functional theory/effective fragment potential method (TDDFT/EFP). Chapter 5 elucidates an excited-state solvent assisted quadruple hydrogen atom transfer reaction of a coumarin derivative using micro solvated quantum mechanical (QM) water and macro solvated EFP water. Chapter 6 presents a dispersion correction to the QM−EFP1 interaction energy. Finally, a general conclusion of this dissertation work and prospective future direction are presented in Chapter 7.

Theoretical Background

The following quantum chemistry notations were used throughout this chapter. Many electron operators are denoted by a hat over upper case Latin letters. For example, the Hamltonion is $\hat{H}$. One-electron operators are denoted by a hat over lower case Latin letters. For example, the Fock operator for electron-one is $\hat{f}(1)$. The exact many electron wave function is denoted by Φ. The approximate many electron wave function is denoted by Ψ. Molecular spin orbitals (with latin indices $i, j, k, \ldots$) are denoted by χ. Molecular spatial orbitals (with latin indices $i, j, k, \ldots$) are denoted by ψ. Atomic spatial orbitals (with greek indices $\mu, \nu, \lambda, \ldots$) are denoted by ϕ. Occupied molecular spatial orbitals are

specifically labeled by $a,b,c,\ldots$. Virtual molecular spatial orbitals specifically labeled by $r,s,t,\ldots$. Exact energies are denoted by E_{exact}. Approximate energies are denoted by E.

Ab initio methods

Ab initio methods refer to a set of quantum mechanical approaches derived from the first principles of quantum mechanics. Generally, the term *ab initio* description is applied to methods that make certain approximations in order to solve the time-dependent (TD) Schrödinger equation[1-6]

$$i\hbar\frac{\partial}{\partial t}\Phi_{TD}\left(\mathbf{r},\mathbf{R},t\right)=\hat{H}\Phi_{TD}\left(\mathbf{r},\mathbf{R},t\right) \tag{1}$$

where Φ_{TD} is the wavefunction, which depends on the electronic coordinates, $\mathbf{r}$, nuclear coordinates, $\mathbf{R}$, and time, t. $\hat{H}$ is the nonrelativistic Hamiltonian operator. $\hbar$ is Planck's constant, h, divided by 2π; i is the square root of -1.

The first approximation to Φ_{TD} made by many *ab inito* methods is to assume that the spatial part ($\mathbf{r}$ and $\mathbf{R}$) and the time part (t) of Φ_{TD} are separable

$$\Phi_{TD}\left(\mathbf{r},\mathbf{R};t\right)\approx\Phi\left(\mathbf{r},\mathbf{R}\right)f\left(t\right) \tag{2}$$

where Φ is the time-independent wavefunction and f is the time-dependent function. Therefore, the time-independent Schrödinger equation can be written as

$$\hat{H}\Phi\left(\mathbf{r},\mathbf{R}\right)=E\Phi\left(\mathbf{r},\mathbf{R}\right) \tag{3}$$

where E is the total energy of the system. Unlike the time-dependent Schrödinger equation, the time-independent Schrödinger equation can be expressed as an eigenvalue problem.

For a molecule with N electrons and M nuclei the Hamiltonian operator can be written in atomic units as

$$\hat{H} = -\sum_{i=1}^{N} \frac{1}{2}\nabla_i^2 - \sum_{A=1}^{M} \frac{1}{2M_A}\nabla_A^2$$
$$+ \sum_{i=1}^{N}\sum_{j>i}^{N} \frac{1}{r_{ij}} + \sum_{A=1}^{M}\sum_{B>A}^{M} \frac{Z_A Z_B}{R_{AB}} \tag{4}$$
$$- \sum_{i=1}^{N}\sum_{A=1}^{M} \frac{Z_A}{r_{iA}}$$

where the electrons and the nuclei are described by the position vector $\mathbf{r}_i$ and $\mathbf{R}_A$, respectively. The distance between ith electron and the jth electron is $r_{ij} = |\mathbf{r}_{ij}| = |\mathbf{r}_i - \mathbf{r}_j|$; the distance between Ath nucleus and the Bth nucleus is $R_{AB} = |\mathbf{R}_{AB}| = |\mathbf{R}_A - \mathbf{R}_B|$, and the distance between ith electron and the Ath nucleus is $r_{iA} = |\mathbf{r}_{iA}| = |\mathbf{r}_i - \mathbf{R}_A|$. The M_A is the ratio of the mass of nucleus A to the mass of an electron, and Z_A is the atomic number of nucleus A. The Laplacian operators ∇_i^2 and ∇_A^2 involve differentiation with respect to the coordinates of the ith electron and the Ath nucleus. The first term in Eq. (4) is the operator for the kinetic energy for the electrons $\left(\hat{T}_e\right)$; the second term is the operator for the nuclear kinetic energy$\left(\hat{T}_n\right)$; the third term represents the repulsion between electrons $\left(\hat{V}_{ee}\right)$; the fourth term represents the repulsion between nuclei $\left(\hat{V}_{nn}\right)$: the fifth term

represents the attraction between electrons and nuclei $\left(\hat{V}_{en}\right)$. The Schrödinger equation may be written compactly as

$$\hat{H} = \hat{T}_e(\mathbf{r}) + \hat{T}_n(\mathbf{R}) + \hat{V}_{ee}(\mathbf{r}) + \hat{V}_{nn}(\mathbf{R}) + \hat{V}_{en}(\mathbf{r},\mathbf{R}) \tag{5}$$

Unfortunately, $\hat{V}_{en}(\mathbf{r},\mathbf{R})$ is problematic, because the electronic and nuclear coordinates are not separable, so the wave function cannot be written as a product of nuclear and electronic terms.

The second approximation made by many *ab inito* methods is the separation of nuclear and electronic motion (Born-Oppenheimer approximation).[7] This is possible because the nuclear masses are much greater than those of electrons, and therefore, nuclei move much more slowly compared to the electrons. As a consequence, the electrons in a molecule rapidly adjust their distribution to changing nuclear positions. This makes it a reasonable approximation to assume that the electron distribution depends only on the instantaneous *positions* of the nuclei and not on their *velocities*. The Born-Oppenheimer approximation eliminates the nuclear kinetic energy term $\left(\hat{T}_n\right)$ in Eq. (5), and it allows the repulsion between nuclei $\left(\hat{V}_{nn}\right)$ to be calculated once and held constant while the electronic part of the Schrödinger equation is solved. The Hamiltonian of Eq. (5) is then reduced to an electronic Hamiltonian $\left(\hat{H}_{elec}\right)$:

$$\hat{H}_{elec} = \hat{T}_e(\mathbf{r}) + \hat{V}_{ee}(\mathbf{r}) + \hat{V}_{en}(\mathbf{r},\mathbf{R}) \tag{6}$$

Therefore the electronic Schrödinger equation can be written as

$$\hat{H}_{elec}\Phi_{elec} = E_{elec}\Phi_{elec} \qquad (7)$$

The solution to the above Schrödinger equation is the electronic wavefunction

$$\Phi_{elec} = \Phi_{elec}\left(\{\mathbf{r}_i\};\{\mathbf{R}_A\}\right) \qquad (8)$$

which describes the motion of electrons. Φ_{elec} *explicitly* depends on the electronic coordinates but depends *parametrically* on the nuclear coordinates, as does the electronic energy.

$$E_{elec} = E_{elec}\left(\{\mathbf{R}_A\}\right) \qquad (9)$$

Therefore, the total electronic energy (potential energy expression) must contain the electronic energy and the nuclear repulsion energy for a particular nuclear configuration.

$$E_{tot} = E_{elec} + \sum_{A=1}^{M}\sum_{B>A}^{M}\frac{Z_A Z_B}{R_{AB}} \qquad (10)$$

Eq. (10) gives rise to the concept of a potential energy surface (PES), a function that describes how the total electronic energy of a system varies with the nuclear degrees of freedom.

For a system with more than one electron, further approximations are required to treat the $\hat{V}_{ee}$ term in Eq. (6), because the electron coordinates are not separable. The most basic approximation is to substitute the *explicit* electron-electron interaction with an averaged interaction and solve self-consistently. Each electron is subjected not to every other individual electron, but to the mean field of the rest of the electrons. This

approximation is known as the self-consistent field (SCF) Hartree-Fock (HF) method.[8-11]

Starting from Eq. (6), the one-electron Fock operator $\hat{f}(1)$ for electron 1 is given by

$$\hat{f}(1) = \hat{h}(1) + v^{HF}(1) \tag{11}$$

The first term in Eq. (11) is the core-Hamiltonion operator. $\hat{h}(1)$ is given by

$$\hat{h}(1) = -\frac{1}{2}\nabla_1^2 - \sum_{A=1}^{M} \frac{Z_A}{r_{1A}} \tag{12}$$

which describes the kinetic energy and the potential energy of an electron in the field of the nuclei. The second term in Eq. (11) is the effective one-electron potential operator called the Hartree-Fock potential $v^{HF}(1)$, which results from the presence of the other electrons.

$$v^{HF}(1) = \sum_{i=1}^{N} \left[\hat{J}_i(1) - \hat{K}_i(1) \right] \tag{13}$$

In Eq. (13) $\hat{J}$ is the Coulomb operator and $\hat{K}$ is the exchange operator.

An electronic wavefunction for *N* particles must be a function of 4*N* coordinates: for each electron, we have x, y, and z Cartesian coordinates plus the spin coordinate (ω), which can have values α and β. The Cartesian coordinates for electron *i* are usually denoted by a collective index $\mathbf{r}_i$, and the set of Cartesian plus spin coordinates is often denoted $\mathbf{x}_i$. The wavefunction $\chi_a(\mathbf{x})$ of an electron is a spin-orbital, which takes the form

$$\chi_a(\mathbf{x}) = \begin{cases} \psi(\mathbf{r})\alpha(\omega) \\ \quad \text{or} \\ \psi(\mathbf{r})\beta(\omega) \end{cases} \tag{14}$$

where $\psi(\mathbf{r})$ is the spatial component and the spin component is either α or β (spin up or spin down).

What is an appropriate form for an *N*-electron wavefunction? The simplest solution would be a product of one-electron functions referred to as a Hartree product Ψ^{HP}. $\Psi^{HP}(\mathbf{x}_1, \mathbf{x}_2, \ldots, \mathbf{x}_N) = \chi_1(\mathbf{x}_1)\chi_2(\mathbf{x}_2)\cdots\chi_N(\mathbf{x}_N)$ (15)

Unfortunately, the Hartree product is not a suitable wavefunction because it ignores the antisymmetry principle. Since electrons are fermions, the electronic wavefunction must be antisymmetric with respect to the interchange of the coordinates of any pair of electrons. This is not the case for the Hartree product.

The required antisymmetric condition to the multi electronic wavefunction can be achieved by using Slater determinant:

$$\Psi(\mathbf{x}_1, \mathbf{x}_2, \ldots, \mathbf{x}_N) = (N!)^{-1/2} \begin{vmatrix} \chi_i(\mathbf{x}_1) & \chi_j(\mathbf{x}_1) & \cdots & \chi_k(\mathbf{x}_1) \\ \chi_i(\mathbf{x}_2) & \chi_j(\mathbf{x}_2) & \cdots & \chi_k(\mathbf{x}_2) \\ \vdots & \vdots & & \vdots \\ \chi_i(\mathbf{x}_N) & \chi_j(\mathbf{x}_N) & \cdots & \chi_k(\mathbf{x}_N) \end{vmatrix} \tag{16}$$

It is convenient to introduce a shorthand notation using the diagonal elements of the Slater determinant as follows:

$$\Psi\left(\mathbf{x}_1,\mathbf{x}_2,\ldots,\mathbf{x}_N\right)=\left|\chi_i\chi_j\cdots\chi_k\right\rangle \tag{17}$$

In quantum chemical computations, each unknown spatial molecular orbital $\left(\psi\right)$ is expanded using a set of known set of basis functions (atomic spatial orbitals). The ith molecular spatial orbital ψ_i can be represented by a summation over basis functions (atomic spatial orbitals) $\left\{\phi_1,\ldots,\phi_N\right\}$, called a linear combination of atomic orbitals (LCAO):

$$\psi_i=\sum_{\mu=1}^{N}C_{\mu i}\phi_\mu \tag{18}$$

where $C_{\mu i}$ are the LCAO coefficients. Basis sets of the atomic orbitals are usually comprised of Gaussian functions. A complete set of basis functions in linear combination could be used to construct any other well-behaved function. In practice, one does not have a complete set of one-particle basis functions $\left\{\chi_i(\mathbf{x})\right\}$; typically one assumes that the incomplete one-electron basis set is large enough to give useful results.

The one-electron operators given in Eq. (13), $\hat{J}$ and $\hat{K}$ act on spin orbitals via the following equations:

$$\hat{J}_b(1)\chi_a(1)=\left[\int d\mathbf{x}_2\chi_b^*(2)r_{12}^{-1}\chi_b(2)\right]\chi_a(1) \tag{19}$$

$$\hat{K}_b(1)\chi_a(1)=\left[\int d\mathbf{x}_2\chi_b^*(2)r_{12}^{-1}\chi_a(2)\right]\chi_b(1) \tag{20}$$

The Hartree-Fock equations define the energy of the spin orbitals χ_a as ε_a;

$$\hat{f}\left|\chi_a\right\rangle=\varepsilon_a\left|\chi_a\right\rangle \tag{21}$$

The Hartree-Fock equations correspond to an optimal set of molecular orbitals that minimize the energy of a molecular system, by making use of the variational principle. This means that the calculated energy of any Hartree-Fock wavefunction, E_{HF}, is guaranteed to be an upper bound to the exact non-relativistic energy E_{exact}.

$$E_{exact} \leq E_{HF} \tag{22}$$

The Hartree-Fock method formally scales on the order of $O(N^4)$ where N measures the size of the system (e.g., number of basis functions). The main downside of the Hartree-Fock method is that it does not account for the instantaneous electron-electron correlation (*explicit* electron-electron interaction) because each electron is in the average field of all the other $(N-1)$ electrons. Due to the neglect of *explicit* electron correlation, the Hartree-Fock method gives an upper limit to the exact energy and the difference between the exact and the Hartree-Fock energy is called the electron correlation energy. In order to recover the electron correlation several post- Hartree-Fock methods have emerged. Some of these methods such as configuration interaction singles (CIS), coupled-cluster methods (CC) and perturbation theory (PT), are summarized below.

The conceptually simplest method for accounting for correlation effects is configuration interaction (CI).[12] The scope of CI is to improve the Hartree-Fock solution by increasing the space of all possible many-electron wavefunction from a single Slater determinant (in Hartree-Fock theory) to a complete set of Slater determinants, in which

all electrons are distributed among all available orbitals. It is convenient to define these other determinants with respect to the determinant $|\Psi_0\rangle$ that is formed from the N lowest energy Hartree-Fock spin orbitals $|\Psi_0\rangle$. The N-electron determinants $|\Psi_i\rangle$ can be written as substitutions or "excitations" from the Hartree-Fock "reference" determinant to obtain the exact many electron wavefunction $|\Phi_0\rangle$:

$$|\Phi_0\rangle = c_0|\Psi_0\rangle + \sum_{\substack{a \\ r}} c_a^r|\Psi_a^r\rangle + \sum_{\substack{a<b \\ r<s}} c_{ab}^{rs}|\Psi_{ab}^{rs}\rangle$$
$$+ \sum_{\substack{a<b<c \\ r<s<t}} c_{abc}^{rst}|\Psi_{abc}^{rst}\rangle + \sum_{\substack{a<b<c<d \\ r<s<t<u}} c_{abcd}^{rstu}|\Psi_{abcd}^{rstu}\rangle + \cdots \qquad (23)$$

where $|\Psi_a^r\rangle$ means the Slater determinant formed by replacing spin-orbital a in $|\Psi_0\rangle$ with spin orbital r, etc. Every N-electron determinant can be described by the set of N spin orbitals from which it is formed, and this set of orbital occupancies is often referred to as a "configuration." The advantage of the CI method is its generality; the formalism applies to excited states and to systems far from their equilibrium geometries. By contrast, conventional single-reference perturbation theory and coupled-cluster approaches generally assume that the reference configuration is dominant, and they may fail when it is not. If one performs a calculation using a given set of one-particle functions $\{\chi_i(\mathbf{x})\}$ and all possible N-electron functions (determinants) $\{|\Psi_i\rangle\}$ the procedure is called "full CI". If one desires only wavefunctions of a given spin and/or spatial symmetry, as is usually the case, only those N-electron functions of that spin and

symmetry are included, since the Hamiltonian matrix is block-diagonal according to space and spin symmetries.

Unfortunately, a full CI is computationally intractable for any but the smallest systems, even with an incomplete one-electron basis set, due to the presence of a large number of N-electron basis functions. Therefore, the CI space in Eq. (23) must be truncated in such a way that the approximate CI wavefunction and energy are as close as possible to the exact values. Singly excited configuration interaction (CIS) is the truncated CI expansion in Eq. (23) after the first summation. The CIS method formally scales on the order of $O(N^5)$. A wavefunction that corresponds to a truncated CI expansion is neither size consistent nor size extensive. A method is said to be size extensive if the energy calculated scales linearly with the number of particles (electrons) N. A method is called size consistent if it gives an energy $E_A + E_B$ for two well separated subsystems A and B in a supermolecule calculation. While the definition of size extensivity applies at any geometry, the concept of size consistency applies only in the limiting case of infinite separation.

The perturbation theory of Møller and Plesset,[13] a subset of many-body perturbation theory (MBPT), is an alternative approach to the CI that considers dynamic correlation effects with better computational scaling. The conventional approach to nth-order MBPT treats the exact non-relativistic Hamiltonian $\hat{H}$ as a perturbed Hartree-Fock

Hamiltonian $\hat{H}_0$, with the energy and wavefunction expanded in *n* orders of the perturbation *V* associated with a parameter λ that can have the value of 0 or 1.

$$\hat{H} = \hat{H}_0 + \lambda V \tag{24}$$

$$\left|\Phi_i\right\rangle = \left|\Psi_i^{(0)}\right\rangle + \lambda \left|\Psi_i^{(1)}\right\rangle + \lambda^2\left|\Psi_i^{(2)}\right\rangle + \cdots \tag{25}$$

$$E_{exact} = E_i^{(0)} + \lambda\, E_i^{(1)} + \lambda^2 E_i^{(2)} + \cdots \tag{26}$$

The $E_i^{(n)}$ is the *n*th-order energy. The motivation of nth-order perturbation theory is to systematically incorporate the higher order corrections to better approximate the exact energy and wavefunction. In particular, the formalism of 2nd-order Møller-Plesset (MP2) theory has found great importance as a reliable, size consistent, and size extensive method. The second-order MP2 energy correction for the ground state (*i* = 0) is

$$E_i^{(2)} = \sum_{n>0} \frac{\left|\left\langle\Psi_0^{(0)}\left|V\right|\Psi_n^{(0)}\right\rangle\right|^2}{E_0^{(0)} - E_n^{(0)}} \tag{27}$$

A disadvantage of the MP2 method is that it is not variational. In addition, the higher order energy corrections (MP3, MP4...) can lead to unpredictable behavior since the MP*n* series is sometimes not convergent. The reliability of perturbation theory depends on how well the Hartree-Fock wavefunction approximates the exact non-relativistic wavefunction. In other words, the perturbation must be small for perturbation theory to provide reliable results. The MP2 method formally scales on the order of $O(N^5)$.

The coupled cluster (CC)[14] method is more computationally expensive but also a more accurate many body approach than MP2. By an exponential *ansatz* for the coupling

of correlated electron pairs, highly excited determinants are incorporated into the wavefunction.

$$|\Phi\rangle = e^{\hat{T}}|\Psi_0\rangle \tag{28}$$

where $|\Psi_0\rangle$ is usually the ground state Slater determinant of the Hartree-Fock molecular orbitals.

The operator $e^{\hat{T}}$ is defined by the Taylor series expansion

$$e^{\hat{T}} = 1 + \hat{T} + \frac{\hat{T}^2}{2!} + \frac{\hat{T}^3}{3!} + \cdots = \sum_{k=0}^{\infty} \frac{\hat{T}^k}{k!} \tag{29}$$

and the cluster operator $\hat{T}$

$$\hat{T} = \hat{T}_1 + \hat{T}_2 + \hat{T}_3 + \cdots + \hat{T}_N \tag{30}$$

where N is the number of electrons in the molecule and the single excitation operator $\left(\hat{T}_1\right)$ and the double excitation operator $\left(\hat{T}_2\right)$ are defined below.

$$\hat{T}_1\Psi_0 = \sum_{r=N+1}^{\infty} \sum_{a=1}^{N} t_a^r \Psi_a^r \tag{31}$$

$$\hat{T}_2\Psi_0 = \sum_{s=r+1}^{\infty} \sum_{r=N+1}^{\infty} \sum_{b=a+1}^{N} \sum_{a=1}^{N-1} t_{ab}^{rs} \Psi_{ab}^{rs} \tag{32}$$

where Ψ_a^r is a single Slater determinant with the occupied spin orbital χ_a replaced by the virtual spin orbital χ_r and t_a^r coefficient. Ψ_{ab}^{rs} is a Slater determinant with the occupied spin orbital χ_a and χ_b replaced by the virtual spin orbitals χ_r and χ_s and t_{ab}^{rs} coefficient. It is necessary to solve for the coefficients t_a^r and t_{ab}^{rs} during the process of finding $|\Phi\rangle$. This is done by solving the following set of equations.

$$\left\langle \Phi_0 \middle| e^{-\left(\hat{T}_1 + \hat{T}_2 + \cdots\right)} \hat{H} e^{\left(\hat{T}_1 + \hat{T}_2 + \cdots\right)} \middle| \Phi_0 \right\rangle = E \tag{33}$$

$$\left\langle \Phi_a^r \middle| e^{-\left(\hat{T}_1 + \hat{T}_2 + \cdots\right)} \hat{H} e^{\left(\hat{T}_1 + \hat{T}_2 + \cdots\right)} \middle| \Phi_0 \right\rangle = 0 \tag{34}$$

$$\left\langle \Phi_{ab}^{rs} \middle| e^{-\left(\hat{T}_1 + \hat{T}_2 + \cdots\right)} \hat{H} e^{\left(\hat{T}_1 + \hat{T}_2 + \cdots\right)} \middle| \Phi_0 \right\rangle = 0 \tag{35}$$

and so on, where Φ_0 is the ground state wavefunction, Φ_a^r is the wavefunction of single excitations, Φ_{ab}^{rs} is the wavefunction of double excitations, etc. The cluster operator (and the number of equations) is truncated at the desired number of excitations. The "gold standard" of computational chemistry is coupled cluster with singles, doubles, and perturbatively calculated triple excitations (CCSD(T)) for its excellent compromise between accuracy and the relatively low computational cost for molecules near equilibrium geometries. The computational cost increases sharply with the highest level of excitation in the CC method. For example CCSD, CCSD(T), and CCSDT methods formally scales in the order of $O\left(N^6\right)$, $O\left(N^7\right)$, and $O\left(N^8\right)$, respectively.

Density Functional Theory

A popular alternative to *ab initio* wavefunction methods is first principles density functional theory (DFT)[15-17] for electronic structure studies. Unlike the methods discussed above (Hartree-Fock, MP*n*, CC, and CI), DFT does not attempt to solve the Schrödinger equation. Instead it is based on the concept that the energy of a chemical

system is a functional form of the electron density $[\rho(x,y,z)]$, which is in turn a function of the coordinates of the nuclei. Regardless of the number of electrons, the electronic density $[\rho(x,y,z)]$ is dependent upon three spatial coordinates; this would eliminate the many body problem associated with solving the Schrödinger equation. In general, DFT has a computational scaling similar to Hartree-Fock theory but it depends on the functional used. Therefore, DFT is an efficient alternative to *ab initio* wavefunction methods.

In DFT method the use of the one-electron Kohn-Sham operator $(\hat{h}_{KS})$, defined in Eq. (36), allows the electrons to be treated as independent particles moving in an external potential of the other electrons, which resembles to the Hartree-Fock method.

$$\hat{h}_{KS} = -\frac{1}{2}\nabla_1^2 - \sum_{A=1}^{M} \frac{Z_A}{|r-r_{1A}|} + \int \frac{\rho(r')}{|r-r'|}dr' + V_{XC}(r) \tag{36}$$

The correlation effects are included via an exchange-correlation functional, $V_{XC}(r)$. The major problem with DFT is that the exact functionals for $V_{XC}(r)$ are not known except for the free electron gas. However, approximations such as the local-density approximation (LDA), the generalized gradient approximation (GGA), and the meta-generalized gradient approximation (meta-GGA) exist which permit the calculation of some properties accurately. Functionals that make use of an admixture of Hartree-Fock exchange are referred to as global hybrid exchange functionals. The functionals that have no Hartree-Fock exchange contribution are known as pure density functionals.

Time-dependent density functional theory (TDDFT)[18,19] is a useful tool for extracting electronic excited state properties. Compared to accurate *ab initio* excited state wavefunction methods, the relatively low computational cost of TDDFT has made it very attractive method for computing excited state properties. The computational scaling factor of TDDFT depends on the DFT functional used. Note that CIS is less expensive than TDDFT. The problem of finding excitation energies within TDDFT can be reduced to the solution of an eigenvalue problem, which in a two-level approximation (i.e., including only single excitations) is given by

$$
\begin{bmatrix} \mathbf{A} & \mathbf{B} \\ \mathbf{B} & \mathbf{A} \end{bmatrix} \begin{bmatrix} \mathbf{X} \\ \mathbf{Y} \end{bmatrix} = \omega \begin{bmatrix} 1 & 0 \\ 0 & -1 \end{bmatrix} \begin{bmatrix} \mathbf{X} \\ \mathbf{Y} \end{bmatrix}
\tag{37}
$$

where $\mathbf{A}$ and $\mathbf{B}$ are the Hessians of the electronic energy. ω is the response matrix which represents the excitation energies, and $\mathbf{X}$ ($\mathbf{Y}$) is a vector that denotes excitation (de-excitation) coefficients.

The dominant contributions to the $\mathbf{A}$ matrix are the transition energies between the virtual and occupied Kohn-Sham orbitals. The matrix $\mathbf{B}$ represents a coupling between different transitions. The elements of the $\mathbf{A}$ and $\mathbf{B}$ matrix elements are given by

$$
A_{ar,bs} = \delta_{ab}\delta_{rs}\left(\varepsilon_r - \varepsilon_a\right) + 2\left(ar|bs\right) + \left(ar|f_{XC}|bs\right)
\tag{38}
$$

$$
B_{ar,bs} = 2\left(ar|bs\right) + \left(ar|f_{XC}|bs\right)
\tag{39}
$$

The leading term on the diagonal of matrix **A** is the orbital energy difference between the occupied orbital *a* and the virtual orbital *r*. The remaining terms in **A** (and **B**) correspond to two-electron integrals between *a,b* occupied orbitals and *r,s* virtual orbitals.

The most challenging part of the DFT approach is determining the appropriate exchange and correlation functionals. Many exchange and correlation functionals contain parameters, that are fitted to describe specific types of chemical systems or processes. However, the DFT approach can be computationally more tractable than the correlated *ab initio* approaches.

References

(1)   Schrödinger, E. *Naturwissenschaften* **1926**, *14*, 664.

(2)   Schrödinger, E. *Annalen Der Physik* **1926**, *79*, 361.

(3)   Schrödinger, E. *Annalen Der Physik* **1926**, *79*, 489.

(4)   Schrödinger, E. *Annalen Der Physik* **1926**, *79*, 734.

(5)   Schrödinger, E. *Annalen Der Physik* **1926**, *80*, 437.

(6)   Schrödinger, E. *Annalen Der Physik* **1926**, *81*, 109.

(7)   Born, M.; Oppenheimer, R. *Annalen Der Physik* **1927**, *84*, 0457.

(8)   Hartree, D. R. *Proc. Cambridge Phil. Soc.* **1928**, *24*, 89.

(9)   Hartree, D. R. *Proc. Cambridge Phil. Soc.* **1928**, *24*, 111.

(10)   Hartree, D. R. *Proc. Cambridge Phil. Soc.* **1928**, *24*, 426.

(11)   Fock, V. *Physik* **1930**, *61*, 126.

(12)   Foresman, J. B.; Head-Gordon, M.; Pople, J. A.; Frisch, J. *J. Phys. Chem.* **1992**, *96*, 135.

(13)   Moller, C.; Plesset, M. S. *Phys. Rev. Lett.* **1934**, *46*, 618.

(14)   Shavitt, I.; Bartlett, R. J. *Many-Body Methods in Chemistry and Physics: MBPT and Coupled-Cluster Theory,*; Cambridge University Press: New York, 2009.

(15)   Parr, R. G. *Annu. Rev. Phys.* **1995**, *46*, 701.

(16)   Hohenberg, P.; Kohn, W. *Phys. Rev. B.* **1964**, *136*, 864.

(17)   Kohn, W.; Sham, L. J. *Phys. Rev. A* **1965**, *140*, 1133.

(18)   Runge, E.; Gross, E. K. U. *Phys. Rev. Lett.* **1984**, *52*, 997.

(19)   Petersilka, M.; Gossmann, U. J.; Gross, E. K. U. *Phys. Rev. Lett.* **1996**, *76*, 1212.

CHAPTER 2. ANHARMONICITY OF WEAKLY BOUND
$M^+−H_2$ COMPLEXES

Nuwan De Silva, Bosiljka Njegic, and Mark S. Gordon

Abstract

The anharmonicity of weakly bound complexes is studied using the vibrational self-consistent field (VSCF) approach for a series of metal cation dihydrogen ($M^+−H_2$) complexes. The H–H stretching frequency shifts of $M^+–H_2$ ($M^+ = Li^+$, Na^+, B^+, and Al^+) complexes are calculated with the coupled-cluster method including all single and double excitations with perturbative triples (CCSD(T)) level of theory with the cc-pVTZ basis set. The calculated H–H stretching frequency of $Li^+–H_2$, $B^+–H_2$, $Na^+–H_2$, and $Al^+–H_2$ is red shifted by 121, 202, 74 and 62 cm^{-1}, respectively, relative to that of unbound H_2. The calculated red shifts and their trends are in good agreement with the available experimental and previously calculated data. Insight into the observed trends is provided by symmetry adapted perturbation theory (SAPT).

I. Introduction

Hydrogen is a promising candidate to meet the global energy demand and to foster a cleaner and sustainable new energy economy.[1] In addition, oxidation of hydrogen in a fuel cell yields water as a byproduct; hence, there is no emission of green house gases or ozone precursors. With the recent advances in fuel cell technology, the extensive production of hydrogen using renewable energy sources appears to be a promising direction for solving the current energy crisis.

Although hydrogen is the most abundant element in the universe, constituting about 93% of all atoms, pure hydrogen is not available in significant quantities in nature. Because hydrogen is not available as a pre-existing energy source like fossil fuels, it first must be produced and then stored as a carrier, much like a battery. Production of hydrogen can involve a variety of sources, including natural gas and coal. However, precautions must be taken to avoid the emissions of greenhouse gases and ozone precursors during the hydrogen extraction process.[2]

Another challenge is presented in the large storage capacity necessary for hydrogen, which requires about four times the volume required by gasoline. Therefore, design of suitable, high capacity storage material is of great importance for hydrogen to be an efficient fuel.[3] There are presently three general ways known for storing hydrogen: compressed hydrogen gas tanks, liquid hydrogen tanks, and materials-based hydrogen

storage. The energy density of gaseous hydrogen can be improved by storing hydrogen in compressed hydrogen gas tanks and liquid hydrogen tanks. However, the compressed hydrogen gas tanks and liquid hydrogen tanks have significant disadvantages. Compression is hindered by low hydrogen density and high-pressure operations, resulting in high costs for compression and tanks, and causes safety issues associated with high-pressure storage.[4] Liquefaction of hydrogen requires an amount of energy equal to almost half of that available from hydrogen combustion, and continuous boil-off occurring in the tanks limits the applications.[3]

Recent research has been focused on lighter storage material with favorable uptake and release kinetics to overcome the issues associated with compression and liquefaction tanks. Hydrogen can be bound to materials, such as fullerenes[5,6] and carbon nanotubes,[7,8] stored as a solid compound via physisorption. However, materials that utilize physisorption have a low gravimetric uptake compared to that of chemisorption. Molecular hydrogen bound into a solid storage material via chemisorption such as metal hydrides,[9] complex hydrides,[10] metal cation-doped zeolites,[11] and metal-organic frameworks (MOF),[12] is a promising technique to overcome the storage problem.

Metal cation-dihydrogen (M^+-H_2) complexes are simple charged polyatomic molecules and therefore constitute a useful benchmark system for assessing computational strategies aimed at describing ion-neutral complexes that are relevant for the hydrogen storage problem. In general, M^+-H_2 complexes are weakly bound, with

binding energies typically less than 5 kcal/mol. Therefore, the weak interaction in M^+-H_2 complexes alone cannot achieve a significant adsorption capacity at reasonable temperatures. However, there are strategies to improve adsorption by making charged metal sites available within the material such as alkali-doped carbon nanotubes.[13,14] Analysis of binding between molecular hydrogen and a metal cation is useful to understand the various aspects of hydrogen storage. Such insight might be applied in the future to the design of novel materials with favorable absorption/desorption kinetics.

Interactions between metal cations and dihydrogen adducts have been explored experimentally and theoretically. Recently Bieske, *et al*. reported rotationally resolved infrared spectra of simple metal cation-dihydrogen complexes in the gas phase, including Li^+-H_2,[15] B^+-H_2,[16] Na^+-H_2,[17] and Al^+-H_2.[18] A correlation between the red shift in the H_2 stretching frequencies upon complexation ($\Delta\nu_{HH}$) and the M^+-H_2 interaction energies was explored. A second paper by Bieske *et al*. reconsidered the relationship between the red shift and the metal-H_2 binding.[19] The observed red shifts in the H−H frequencies upon metal complexation was interpreted in terms of a charge transfer from the H−H bonding orbital into the *sp* hybrid orbital of the metal cation, especially for the more polarizable B^+ and Al^+ cations. The correlation between the binding energy and $\Delta\nu_{HH}$ of dihydrogen adducts with alkaline cations (Li^+, Na^+, K^+, Rb^+) was also investigated by Vitillo *et al*.,[11] using Hartree-Fock (HF) and second order perturbation theory (MP2), as well as density functional theory (DFT) with the B3LYP functional. A linear correlation between binding energy and $\Delta\nu_{HH}$ was reported.

The advent of a wide variety of high-resolution infrared spectroscopic methods facilitates more accurate probing of a broader frequency range. To to accurately interpret the origin of the spectral features, computational guidance is essential. The computationally least demanding approach and the most common method for determining vibrational frequencies is the harmonic approximation, a normal mode analysis based on the matrix of second derivatives of the energy (Hessian). However, in general, molecular vibrations are not purely harmonic and the intrinsic anharmonicity (diagonal potential) of a particular mode often increases as the frequency of the vibration decreases. Furthermore, the anharmonicity of a particular mode may increase due to coupling with other modes (coupling potential), coupling that is ignored in the harmonic approximation. The traditional approach to estimate anharmonic frequencies is to use scaling factors for the harmonic frequencies.[20] Scaling the harmonic frequencies has often worked well. However, using a single scale factor for a great diversity of vibrational modes, ranging from the quasi-rigid vibrational motions that take place in strongly bonded molecules to the far more extended and floppy motions that occur in clusters bound by weak van der Waals interactions is not adequate. Therefore, improvements beyond the harmonic approximation can be important. A useful approach for predicting accurate vibrational spectra is the vibrational self-consistent field (VSCF) method, which starts from the harmonic approximation and systematically approaches the correct anharmonic frequencies. The VSCF[21-24] method has emerged in recent years as a powerful tool for accurate predictions of vibrational spectra. The VSCF method can be

augmented by second order perturbation theory (PT2-VSCF),[25] in order to correct for correlation effects among the modes.

The aim of the present paper is to examine the anharmonicity associated with the Li^+-H_2, Na^+-H_2, B^+-H_2, and Al^+-H_2, complexes and characterize the interaction between a hydrogen molecule and a metal cation. The results are compared with the experimental vibrational data, including the bond lengths, the frequency of the H−H stretching mode, and the binding energy. An important motivation for this work is to examine, and attempt to understand, the red shifts in the H–H stretching mode (ν_1) in the M^+-H_2 complexes. The organization of the paper is as follows. Section II describes the computational details. In Sec. III, the geometry, anharmonic frequencies and interaction energies of the M^+-H_2 complexes are discussed. Concluding remarks are summarized in Section IV.

II. Computational Details

All calculations were performed using the GAMESS[26,27] electronic structure code, and the molecules were visualized with MacMolPlt.[28] Electronic structure calculations were performed on M^+-H_2 ($M^+ = Li^+$, Na^+, B^+, and Al^+) complexes using coupled-cluster theory including all single and double excitations with perturbative triples (CCSD(T))[29,30] and the cc-pVTZ[31] basis set. The geometry optimizations were carried out in C_2v

symmetry. The CCSD(T) geometry optimizations were performed using numerical gradients. All stationary points are true minima (all positive force constants).

To obtain the anharmonic frequencies, PT2-VSCF calculations were carried out on the potential energy surface (PES) that was generated on a 16x16 point grid, by making displacements along normal mode vectors expressed as a sum of simple internal coordinate contributions.[32] Cartesian normal mode displacement vectors are often not suitable for treating nonlinear, low frequency vibrational motions, such as, bending and torsion.[32] Because selection of internal coordinates is not unique even in a system as small as three atoms, two internal coordinate selections, 3-bond (two M−H bonds and the H−H bond) and 2-bond-1-angle (two M−H bonds and H−M−H angle), were considered. In order to obtain the optimum set of coordinates, the normal mode vibrational frequencies were partitioned into each internal coordinate according to the method described by Boatz and Gordon.[33]

A series of calculations were carried out in which the spacing of the PES grid points along each vibrational mode was systematically increased until the diagonal frequencies converged, as described in a paper by Njegic and Gordon.[34] While convergence of diagonal ν_1 and ν_3 frequencies was achieved as expected, the diagonal potential for the antisymmetric stretch (ν_2) frequency requires special treatment. At large displacements along the ν_2 mode, the three atoms of $M^+–H_2$ adopt close to a colinear configuration (due to the H–H internal rotation in the molecular plane). This near

linearity causes a failure of the internal to Cartesian coordinate transformation due to a very small determinant of the Wilson B matrix[35] in the iterative procedure. When the internal-to-Cartesian coordinate transformation fails, the displacement vector that was used to generate the point that is closest to the failed point is used to step to the next point on the PES. Since such displacement vectors are expressed in the form of Cartesian rather than internal coordinates, artificial stretching may be introduced in the similar manner as if Cartesian coordinates VSCF were used to generate PES. If the number of failed points is small, the consequent errors may make only negligible contributions to the calculated VSCF frequencies. Unfortunately, for M^+–H_2, there is a large number of failed points generated along both diagonal and coupling potentials involving the ν_2 mode, whereas the number of failed points for the ν_1 and ν_3 frequencies is zero. To address this problem, a different approach was used for the ν_2 mode, in which the energies of the failed points were extrapolated by a forth order polynomial fit.

To obtain bond dissociation energies that can be related to experiment, D_0, zero point energy (ZPE) corrections have been obtained using the anharmonic frequencies. To analyze the relationship between the M^+−H_2 binding energies and the red shifts in the H−H vibrational frequencies, symmetry adapted perturbation theory (SAPT)[36] calculations were performed for each complex, also using the cc-pVTZ basis set. An additional interpretive tool is provided by the electrostatic potential (ESP)-derived MP2/cc-pVTZ atomic charges.[37,38]

III. Results and Discussion

Molecular hydrogen adopts a C_2v structure with each of the four isovalent metal cations, M^+ (Li^+: [He]; B^+: [He]$2s^2$; Na^+: [Ne]; Al^+: [Ne]$3s^2$).[11] Table 1 lists selected CCSD(T) geometric parameters of M^+–H_2 complexes, obtained with the cc-pVTZ basis set. The distance between M^+ and the midpoint along the H–H bond (R) increases with the size of the metal cation. The R values are obtained experimentally via vibrationally averaged separations (R_0), whereas calculated values are equilibrium separations (R_e). As one would expect, R_0 is generally larger than R_e. The H−H bond length changes (Δr_{HH}) are taken relative to isolated H_2 whose calculated bond distance is 0.743 Å. The Li^+−H_2 and B^+−H_2 complexes have a larger Δr_{HH} (about 0.010 Å) than the Na^+−H_2 and Al^+−H_2 complexes (about 0.005 Å). The larger Δr_{HH} may be due to greater electron delocalization of the H–H bond toward the Li^+ and B^+ centers than for Na^+ and Al^+, leading to greater H–H bond weakening. These relationships are discussed in more detail below.

The three M^+–H_2 vibrational modes may be characterized by normal mode vectors as: H–H symmetric stretch (ν_1 = ~4000 cm^{-1}), M^+–H_2 antisymmetric stretch (ν_2 = ~700 cm^{-1}) and M^+–H_2 symmetric stretch (ν_3 = ~400 cm^{-1}). Choosing a coordinate system to use for the PES displacements plays a vital role in VSCF calculations. Choosing the most separable coordinate system even for triatomic molecules is not trivial. The ideal coordinate system has minimal mode-mode coupling. In some previous rovibrational

energy level calculations, the Hamiltonian was written in Jacobi coordinates (r, R, θ) for Li$^+$–H$_2$,[39] Na$^+$–H$_2$,[17] and Al$^+$–H$_2$[18] complexes, where **r** is the H–H intra-molecular vector, **R** is the vector between M$^+$ and the midpoint along H–H bond, and θ is the angle between **r** and **R**. In this paper, the following three choices of coordinates for M$^+$–H$_2$ complexes are considered: (1) Cartesian coordinates; (2) two M–H bonds and the subsumed angle (2-bond-1-angle); (3) three bonds (3-bond). Previous work has demonstrated the utility of internal coordinates for performing VSCF calculations.[32,34] Boatz and Gordon[33] demonstrated how to decompose normal modes and the corresponding force constants in terms of internal coordinates. This method can be used to help determine the most separable set of internal coordinates. For example, Table 2 presents the contribution of each internal coordinate to each normal coordinate force constant for the Li$^+$–H$_2$ complex at the CCSD(T)/cc-pVTZ level of theory. In all three normal modes, the Li–H bond distances contribute for both choices of internal coordinates, whereas the H–H distance appears to be a more appropriate choice than the H–Li–H angle.

The difference between the two sets of internal coordinates arises from the treatment of the H–H bond distance. The 3-bond set of internals ensures an explicit treatment of the H–H bond length during molecular vibrations. The contribution of the H–Li–H angle to the ν$_2$ mode is zero (Table 2). In Figures 1a and 1b, the H–H distance is plotted as a function of the displacements (at small amplitude displacements) made along the ν$_2$ and ν$_3$ modes, respectively, when Cartesian, 2-bond-1-angle and 3-bond coordinates are used to generate the diagonal PES. While both Cartesian and 2-bond-1-

angle coordinates lead to changes in the H−H distance as displacements are made along mode ν_2, the H−H distance is preserved if 3-bond coordinates are used. The performance of the three coordinate sets is also reflected in the very different values of the ν_2 diagonal frequency at amplitude ~1100, ~1100, ~800 cm^{-1} for the Cartesian, 2-bond-1-angle and 3-bond coordinates, respectively. Importantly, any errors that are made in the diagonal potential (for example, by using inappropriate coordinates) will be propagated into the coupling potential, and this will be reflected in errors in the predicted anharmonic frequencies. Both Cartesian and 3-bond coordinates preserve the H−H distance as displacements are made along mode ν_3, while the 2-bond-1-angle coordinate choice leads to changes in the H−H distance (Figure 1b).

Figure 2 shows vectors associated with the three types of vibrational motion exhibited by the M–H$_2^+$ molecules. While the ν_1 and ν_3 modes can be described as linear displacements, the ν_2 mode vectors show strikingly different types of motion, depending on whether they are expressed in terms of 2-bond-1-angle (Figure 2a) or 3-bond (Figure 2b). While the ν_2 antisymmetric stretch can be described as linear displacements along the bonds when the 2-bond-1-angle internal coordinates are used, one sees the in-plane internal rotation noted earlier when the 3-bond internal coordinates are used. The 3-bond coordinate system ensures maximum separation of all three modes and thus is used in all subsequent calculations of molecular vibrations.

The calculated CCSD(T)/cc-pVTZ harmonic and anharmonic (VSCF-PT2) vibrational frequencies along with other available published calculations and experimental data are tabulated in Table 3. There is an excellent agreement (within 20 cm^{-1}) of the PT2-VSCF frequencies with the available experimental data. The anharmonic corrections to the harmonic frequencies are rather different for the three vibrational modes. The ratio of the VSCF-PT2/harmonic frequencies ranges from 0.74 to 0.94 for the various frequencies listed in Table 3. This illustrates the fact that using one scaling factor[40] to scale all harmonic frequencies would not capture the actual anharmonicity that is present in the complexes. The VSCF-PT2 frequencies are in good agreement with the published rovibrational calculations.

Table 4 shows the CCSD(T)/cc-pVTZ calculated H–H frequency shifts of the M^{+}–H$_2$ complexes. Harmonic red shifts are calculated with respect to the harmonic frequencies of isolated H$_2$. The PT2-VSCF red shifts are calculated with respect to the diagonal frequencies of isolated H$_2$. The experimental H–H stretching frequency of molecular H$_2$ is 4161.17 cm^{-1}.[41] The VSCF-PT2 frequencies capture the *trends* in the experimental red shifts both qualitatively and quantitatively.

The binding energies (D_e) of the M^{+}–H$_2$ complexes are calculated as D_e = [total Energy (M^{+} and H$_2$ fragments)] – [total Energy (M^{+}–H$_2$ complex)]. The ZPE-corrected binding enthalpy (D_0) is the sum of D_e and ΔZPE. The CCSD(T)/cc-pVTZ M^{+}–H$_2$ binding energies are given in Table 5. Theory and experiment are in good agreement,

with errors in the calculated values in the range of 0.3 to 0.6 kcal/mol, well below chemical accuracy (~1 kcal/mol). The trend in binding energies is also captured, with the binding energies in the order Li > B > Na > Al. H_2 binds weakly to these cations, with the CCSD(T) D_0 ranging from 0.93 to 4.48 kcal/mol.

The values of D_0 and R follow the expected inverse relationship, as the D_0 values increase nearly linearly as the R values of the M^+–H_2 complexes decrease, as shown in Figure 3. The M^+–H_2 symmetric stretching frequencies, ν_3, are linearly correlated with D_0 as shown in Figure 4. This is to be expected, as the ν_3 mode is the one that leads to the dissociation of the M^+–H_2 complex into H_2 molecule and a metal cation.

Based on the binding energies, one might predict the red shift associated with the H–H stretching frequency to be in the order Li^+–H_2 > B^+–H_2 > Na^+–H_2 > Al^+–H_2, since this is the order in which the M^+–H bond energy decreases. That is, one might expect a concomitant decrease in the H–H bond energy and frequency based on common bond distance-bond energy relationships. However, as shown in Table 4 and in Figure 5, the observed red shifts are in the order B^+–H_2 > Li^+–H_2 > Na^+–H_2 > Al^+–H_2. The main disagreement between the red shifts and the binding energies occurs for Li^+ versus B^+. In addition, the red shifts induced by Na^+ versus Al^+ are much closer to each other than would be predicted based on the corresponding binding energies.

In an attempt to understand the relationship between the observed metal-H_2 binding energies and the red shifts in the H–H frequencies that are observed upon complexation, the symmetry adapted perturbation theory (SAPT) method that was developed by Jeziorski, Szalewicz and co-workers[36] is employed as an appealing interpretive tool. The SAPT method is based on many body perturbation theories and is therefore expected to provide relative energies that are as accurate as CCSD(T).

The SAPT total interaction energies and the corresponding components for the four complexes of interest here are summarized in Table 6. For convenience, the CCSD(T) binding energies (excluding zero point vibrational corrections) and H–H red shifts are included in this table as well. First, note that the total SAPT interaction energies are in very good agreement with the CCSD(T) binding energies. This lends credence to employing the SAPT energy decomposition. Now, note that each of the attractive terms in Table 6, those that contribute to bonding interactions (Coulomb, induction, dispersion, and charge transfer), demonstrate the same trend as do the red shifts in the H–H frequencies, *not* the trend followed by the M–H binding energies. That is, those interactions that one would conceptually associate with binding demonstrate the expected relationship with the weakening of the H–H bond. The fact that the charge transfer essentially follows the same trend (except for the very small values of Na and Al) supports the conjecture by Bieske and co-workers regarding the role of charge transfer. However, charge transfer is certainly not the whole, or even the most important part of the story, since the largest contribution to binding of each metal to H_2 comes from the

induction interaction. The sum of the four attractive contributions, labeled "total attraction" in Table 6, follows the same trend as the H–H frequency red shifts.

On the other hand, the repulsive terms, dominated by the exchange repulsion, are much larger for B than for the other metals. These repulsive terms more than counter balance the attractive terms that favor B over Li for binding to H_2. So, as is usually the case, the net binding is a balance between attractive and repulsive contributions, and in this case, the balance results in stronger net binding of H_2 to Li than to B.

The total electron density maps and the ESP atomic charges for each of the M^+–H_2 complexes are shown in Figure 6. There are two interesting trends apparent in this figure. First, the electron density shifts upon complexation, as embodied in the ESP charges, from H_2 to M^+, is in the order B > Li > Na ~ Al. This is the same order that is observed for the H–H frequency red shifts and is consistent with the foregoing discussion. Similarly, one can see from the total density maps that the delocalization of charge follows the same trend. This trend in electron density reflects the importance of both induction and charge transfer, as noted in the previous paragraphs.

IV. Conclusions

The theoretical study of anharmonic molecular vibrations and binding energies of Li^+–H_2, Na^+–H_2, B^+–H_2 and Al^+–H_2 complexes using the VSCF method corrected for

second order perturbation theory have been presented. The CCSD(T) red shifts and the predicted M^+–H_2 binding energies are in excellent agreement with the experimental values. The unusual relationship between the experimentally observed binding energies and red shifts in the H–H vibrational frequencies is also well reproduced by theory. The fact that the trends in the red shifts do not reflect the binding energy trends is interpreted, using the SAPT method, in terms of a balance between opposing attractive and repulsive interactions.

The anharmonic corrections to the harmonic frequencies are rather different for the three vibrational modes in these M^+–H_2 complexes. For example, the ratio of the VSCF-PT2/harmonic frequencies is 0.94 for the H-H stretch, while this ratio ranges from 0.74 to 0.86 for the symmetric stretch versus 0.87 to 0.94 for the antisymmetric stretch. This means that one universal scaling factor to scale the harmonic frequencies would not capture the actual anharmonicity that is present in the complexes. So, while calculating VSCF frequencies is more computationally challenging than employing a simple scale factor, the VSCF approach is more accurate.

Acknowledgements

References

(1)   Service, R. F. *Science* **2004**, *305*, 958.

(2)   Schultz, M. G.; Diehl, T.; Brasseur, G. P.; Zittel, W. *Science* **2003**, *302*, 624.

(3)   Schlapbach, L.; Zuttel, A. *Nature* **2001**, *414*, 353.

(4)   Zhou, L. *Renewable Sustainable Energy Rev.* **2005**, *9*, 395.

(5)   Kim, Y. H.; Zhao, Y. F.; Williamson, A.; Heben, M. J.; Zhang, S. B. *Phys. Rev. Lett.* **2006**, *96*, 016102.

(6)   Liu, Y.; Brown, C. M.; Blackburn, J. L.; Neumann, D. A.; Gennett, T.; Simpson, L.; Parilla, P.; Dillon, A. C.; Heben, M. *J. Alloys Compd.* **2007**, *446*, 368.

(7)   Fakioglu, E.; Yurum, Y.; Veziroglu, T. N. *Int. J. Hydrogen Energy* **2004**, *29*, 1371.

(8)   Tang, C. C.; Bando, Y.; Ding, X. X.; Qi, S. R.; Golberg, D. *J. Am. Chem. Soc.* **2002**, *124*, 14550.

(9)   Grochala, W.; Edwards, P. P. *Chem. Rev.* **2004**, *104*, 1283.

(10)   Orimo, S. I.; Nakamori, Y.; Eliseo, J. R.; Zuttel, A.; Jensen, C. M. *Chem. Rev.* **2007**, *107*, 4111.

(11)   Vitillo, J. G.; Damin, A.; Zecchina, A.; Ricchiardi, G. *J. Chem. Phys.* **2005**, *122*, 114311.

(12)   Mulder, F. M.; Dingemans, T. J.; Schimmel, H. G.; Ramirez-Cuesta, A. J.; Kearley, G. J. *Chem. Phys.* **2008**, *351*, 72.

(13)   Chen, P.; Wu, X.; Lin, J.; Tan, K. L. *Science* **1999**, *285*, 91.

(14)   Yang, R. T. *Carbon* **2000**, *38*, 623.

(15)   Emmeluth, C.; Poad, B. L. J.; Thompson, C. D.; Weddle, G. H.; Bieske, E. J. *J. Chem. Phys.* **2007**, *126*, 204309.

(16)   Dryza, V.; Poad, B. L. J.; Bieske, E. J. *J. Am. Chem. Soc.* **2008**, *130*, 12986.

(17)   Poad, B. L. J.; Wearne, P. J.; Bieske, E. J.; Buchachenko, A. A.; Bennett, D. I. G.; Klos, J.; Alexander, M. H. *J. Chem. Phys.* **2008**, *129*, 184306.

(18)   Emmeluth, C.; Poad, B. L. J.; Thompson, C. D.; Weddle, G.; Bieske, E. J.; Buchachenko, A. A.; Grinev, T. A.; Klos, J. *J. Chem. Phys.* **2007**, *127*, 164310.

(19)   Dryza, V.; Poad, B. L. J.; Bieske, E. J. *J. Phys. Chem. A* **2009**, *113*, 6044.

(20)   Pople, J. A.; Scott, A. P.; Wong, M. W.; Radom, L. *Isr. J. Chem.* **1993**, *33*, 345.

(21)   Chaban, G. M.; Jung, J. O.; Gerber, R. B. *J. Chem. Phys.* **1999**, *111*, 1823.

(22)   Yagi, K.; Taketsugu, T.; Hirao, K.; Gordon, M. S. *J. Chem. Phys.* **2000**, *113*, 1005.

(23)   Yagi, K.; Hirao, K.; Taketsugu, T.; Schmidt, M. W.; Gordon, M. S. *J. Chem. Phys.* **2004**, *121*, 1383.

(24)   Matsunaga, N.; Chaban, G. M.; Gerber, R. B. *J. Chem. Phys.* **2002**, *117*, 3541.

(25)   Jung, J. O.; Gerber, R. B. *J. Chem. Phys.* **1996**, *105*, 10332.

(26)   Gordon, M. S.; Schmidt, M. W. *Theory and Applications of Computational Chemistry: The First Forty Years*; Elsevier: Amsterdam, The Netherlands, 2005.

(27)   Schmidt, M. W.; Baldridge, K. K.; Boatz, J. A.; Elbert, S. T.; Gordon, M. S.; Jensen, J. H.; Koseki, S.; Matsunaga, N.; Nguyen, K. A.; Su, S. J.; Windus, T. L.; Dupuis, M.; Montgomery, J. A. *J. Comput. Chem.* **1993**, *14*, 1347.

(28)   Bode, B. M.; Gordon, M. S. *J. Mol. Graph. Modell.* **1998**, *16*, 133.

(29)   Piecuch, P.; Kucharski, S. A.; Kowalski, K.; Musial, M. *Comput. Phys. Commun.* **2002**, *149*, 71.

(30)   Raghavachari, K.; Trucks, G. W.; Pople, J. A.; Head-Gordon, M. *Chem. Phys. Lett.* **1989**, *157*, 479.

(31)   Dunning, T. H. *J. Chem. Phys.* **1989**, *90*, 1007.

(32)   Njegic, B.; Gordon, M. S. *J. Chem. Phys.* **2006**, *125*, 224102.

(33)   Boatz, J. A.; Gordon, M. S. *J. Phys. Chem.* **1989**, *93*, 1819.

(34)   Njegic, B.; Gordon, M. S. *J. Chem. Phys.* **2008**, *129*, 164107.

(35)   Wilson Jr., E. B.; Decius, J. C.; Cross, P. C. *Molecular Vibrations: The Theory of Infrared and Raman Vibrational Spectra*; Dover Publications, Inc.: New York, 1955.

(36) Jeziorski, B.; Moszynski, R.; Szalewicz, K. *Chem. Rev.* **1994**, *94*, 1887.

(37) Singh, U. C.; Kollman, P. A. *J. Comput. Chem.* **1984**, *5*, 129.

(38) Bayly, C. I.; Cieplak, P.; Cornell, W. D.; Kollman, P. A. *J. Phys. Chem.* **1993**, *97*, 10269.

(39) Sanz, C.; Bodo, E.; Gianturco, F. A. *Chem. Phys.* **2005**, *314*, 135.

(40) Scott, A. P.; Radom, L. *J. Phys. Chem.* **1996**, *100*, 16502.

(41) Bragg, S. L.; Brault, J. W.; Smith, W. H. *Astrophys. J.* **1982**, *263*, 999.

(42) Kraemer, W. P.; Spirko, V. *Chem. Phys.* **2006**, *330*, 190.

(43) Kemper, P. R.; Bushnell, J. E.; Weis, P.; Bowers, M. T. *J. Am. Chem. Soc.* **1998**, *120*, 7577.

(44) Bushnell, J. E.; Kemper, P. R.; Bowers, M. T. *J. Phys. Chem.* **1994**, *98*, 2044.

(45) Kemper, P. R.; Bushnell, J.; Bowers, M. T.; Gellene, G. I. *J. Phys. Chem. A* **1998**, *102*, 8590.

Table 1. Selected CCSD(T) M^+–H_2 geometric parameters, with the cc-pVTZ basis set.

M^+–H_2	R_e(Å)[a]	R_0(Å)[b]	r_{HH}(Å)	Δr_{HH}(Å)[c]
Li^+–H_2	2.018	2.056[d]	0.751	0.008
B^+–H_2	2.242	2.262[e]	0.756	0.013
Na^+–H_2	2.469	2.493[f]	0.748	0.005
Al^+–H_2	2.987	3.035[g]	0.747	0.004

[a,b] The distance between M^+ and the midpoint along H–H bond. Experimental values are R_0; calculated values are R_e.

[c] H−H bond length (r_{HH}) changes (Δr_{HH}) are taken relative to isolated H_2. The isolated H−H bond distances is 0.743 Å at CCSD(T) with the cc-pVTZ basis.

[d] Reference[15]

[e] Reference[16]

[f] Reference[17]

[g] Reference[18]

Table 2. The CCSD(T)/cc-pVTZ contribution of internal coordinates to the normal coordinate force constant for Li^+–H_2.
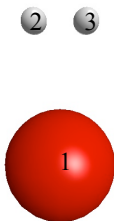
Coordinate System	Coordinate	H–H symmetric stretching (ν_1)	Li^+–H_2 antisymmetric stretching (ν_2)	Li^+–H_2 symmetric stretching (ν_3)
2-bond-1-angle	1-2 bond distance	-0.128	-0.708	0.786
	1-3 bond distance	-0.128	0.708	0.786
	2-1-3 bond angle	-0.357	0.000	-0.075
3-bond	1-2 bond distance	-0.128	-0.708	0.786
	1-3 bond distance	-0.128	0.708	0.786
	2-3 bond distance	-1.409	0.000	0.002

Table 3. Comparison of calculated CCSD(T)/cc-pVTZ frequencies (cm^{-1}) with the available experimental data.

M$^+$–H$_2$	Harmonic	PT2-VSCF	Other Calculations	Experimental
Li$^+$–H$_2$			Rovibrational[a]	
ν_1	4291	4045	N/A	4053[d]
ν_2	695	652	646	N/A
ν_3	478	400	426	N/A
B$^+$–H$_2$				
ν_1	4212	3964	N/A	3941[e]
ν_2	515	480	N/A	N/A
ν_3	356	306	N/A	NA
Na$^+$–H$_2$			Rovibrational[b]	
ν_1	4337	4092	4098	4094[b]
ν_2	533	492	485	N/A
ν_3	307	242	246	N/A
Al$^+$–H$_2$			Rovibration[c]	
ν_1	4348	4104	4099	4095[c]
ν_2	364	318	283	N/A
ν_3	181	134	153	N/A
H$_2$				
ν_1	4409	4166	N/A	4161[f]

[a] Reference[39]

[b] Reference[17]

[c] Reference[18]

[d] Reference[15]

[e] Reference[16]

[f] Reference[41]

Table 4. Calculated CCSD(T)/cc-pVTZ H–H stretching (v_1) frequency red shifts (cm^{-1}) of M^+–H_2 complexes. Harmonic red shifts are calculated with respect to the harmonic frequency of isolated H_2. PT2-VSCF red shifts are calculated with respect to the diagonal frequency of isolated H_2.

M^+H_2	Harmonic	PT2-VSCF	Experimental
B^+–H_2	197	202	221[a]
Li^+–H_2	119	121	108[b]
Na^+–H_2	72	74	67[c]
Al^+–H_2	62	62	66[d]

[a] Reference[16]

[b] Reference[15]

[c] Reference[17]

[d] Reference[18]

Table 5. CCSD(T) ZPE-corrected binding energy (D_0) in kcal/mol for the M^+–H_2 complexes with cc-pVTZ basis set.

	Li^+–H_2	B^+–H_2	Na^+–H_2	Al^+–H_2
D_e	5.81	4.02	3.04	1.49
ΔZPE	1.33	0.83	0.94	0.56
D_0	4.48	3.19	2.09	0.93
Experimental D_0	4.79^a	3.8 ± 0.2^b	2.45 ± 0.2^c	1.35 ± 0.15^d

[a] From rovibrational calculations[42]

[b] Reference[43]

[c] Reference[44]

[d] Reference[45]

Table 6. SAPT/cc-pVTZ interaction energy components (kcal/mol) for M^+–H_2.

	Li^+–H_2	B^+–H_2	Na^+–H_2	Al^+–H_2
SAPT				
Electrostatic/Coulomb	1.71	3.95	1.66	1.30
Polarization/Induction	8.04	8.62	4.58	2.12
Dispersion	0.14	2.62	0.12	1.07
Charge Transfer	1.26	4.72	-0.16	0.67
Exchange	-2.69	-10.90	-1.41	-2.77
Exchange-Induction	-2.51	-3.95	-1.69	-0.64
Exchange-Dispersion	-0.02	-0.25	-0.01	-0.09
Total Attraction[a]	11.15	19.91	6.20	5.16
Total Repulsion[b]	-5.22	-15.10	-3.11	-3.50
E_{int} (SAPT)	5.93	4.81	3.09	1.65
CCSD(T)/cc-pVTZ				
D_e	5.81	4.02	3.04	1.49
H–H Red Shift (VSCF) in cm^{-1}	121	202	74	62

[a]Sum of Electrostatic + Polarization + Dispersion + Charge Transfer

[b]Sum of Exchange + Exchange-Induction + Exchange-Dispersion
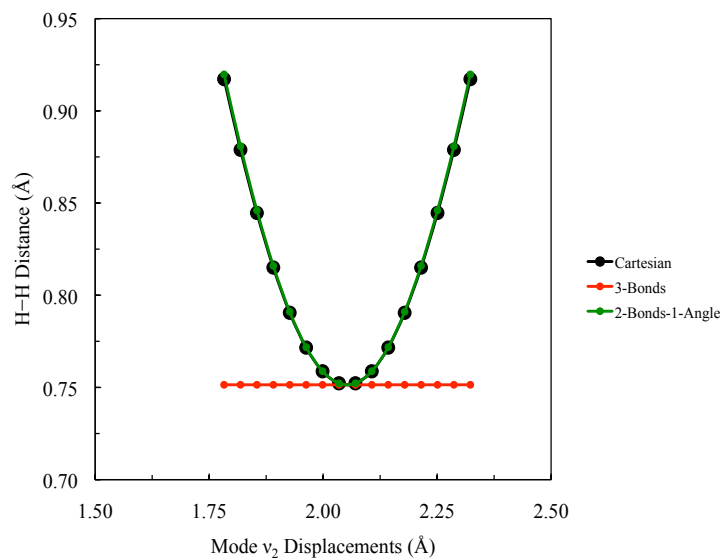
(a)
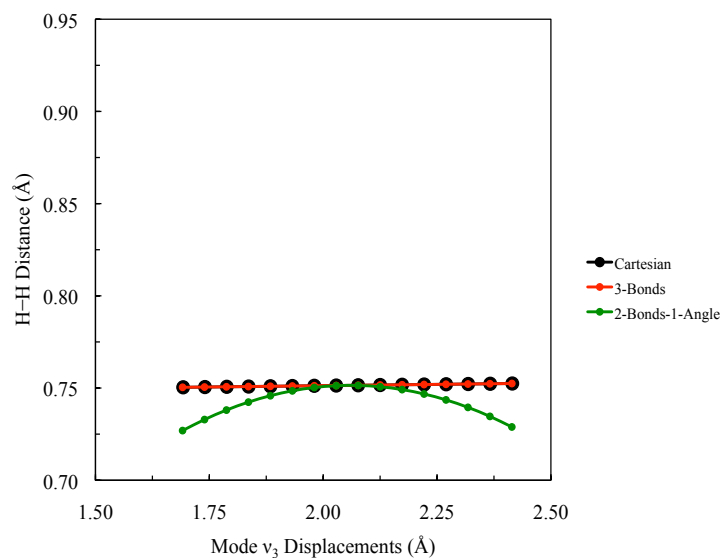
(b)

Figure 1. (a) The H–H distance plotted as a function of displacement made along mode ν_2 (Li$^+$–H$_2$ antisymmetric stretching); (b) The H–H distance plotted as a function of displacement made along mode ν_3 (Li$^+$–H$_2$ symmetric stretching). The displacements are made in Cartesian (black), 3-bond internal (red) and 2-bond-1-angle internal (green) basis for Li$^+$–H$_2$ at the CCSD(T) level of theory with the cc-pVTZ basis set (at small amplitude displacements).
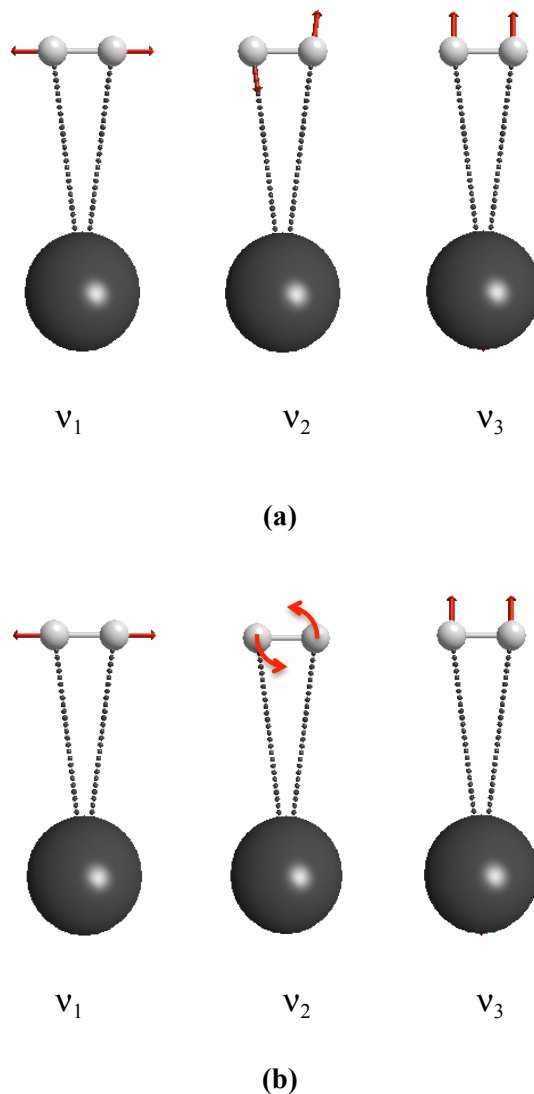
Figure 2. (a) The vibrational motion in normal mode vectors and diagonal VSCF in 2-bond-1-angle internal coordinates for the M^+–H_2 complexes; (b) The vibrational motions depicted by the diagonal VSCF generated using 3-bond internal coordinates.
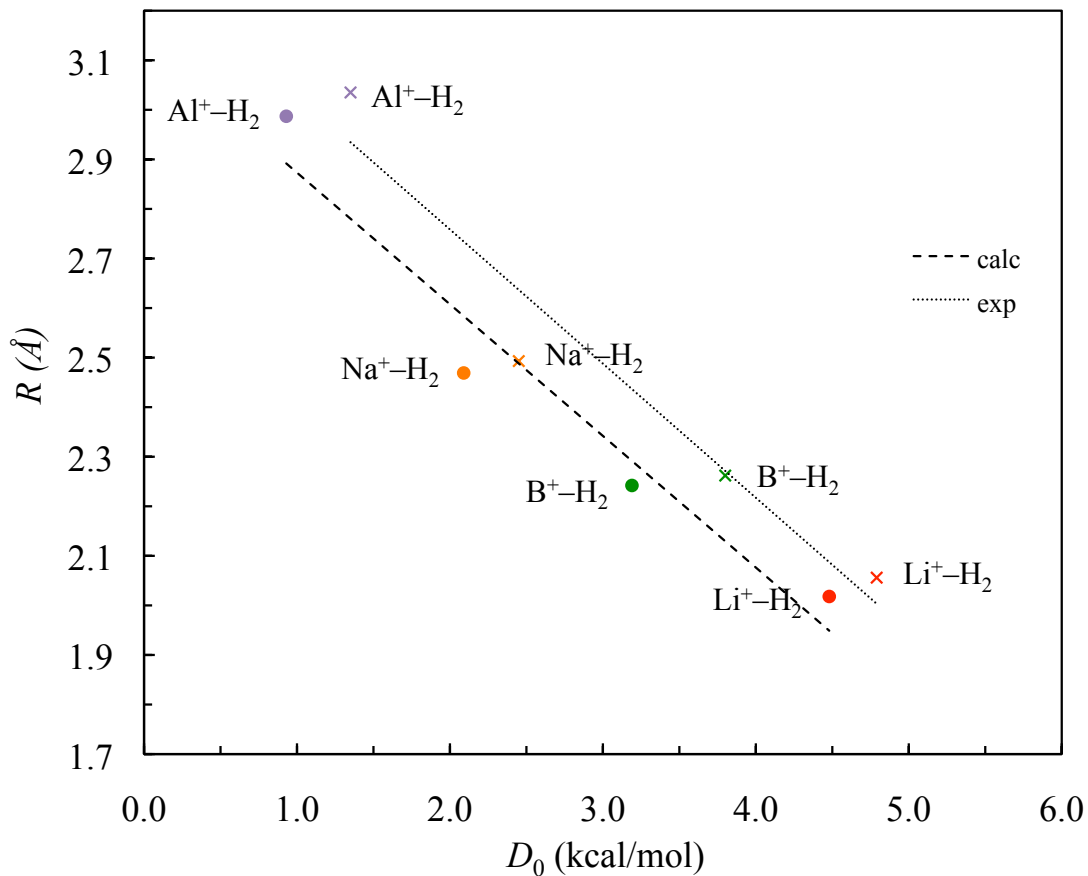
Figure 3. Graph of distance between M^+ and the midpoint along H–H bond (R) vs. the ZPE-corrected binding energy (D_0) for Li^+–H_2 (red), B^+–H_2 (green) Na^+–H_2 (yellow), and Al^+–H_2 (purple). The calculated values at CCSD(T) level of theory with cc-pVTZ basis set, are displayed in circles and the experimental values are displayed in crosses. The binding energies (D_e) of the M^+–H_2 complexes are calculated as follows. The D_e = [Total Energy (M^+ and H_2 fragments)] – [Total Energy (M^+–H_2 molecule)].
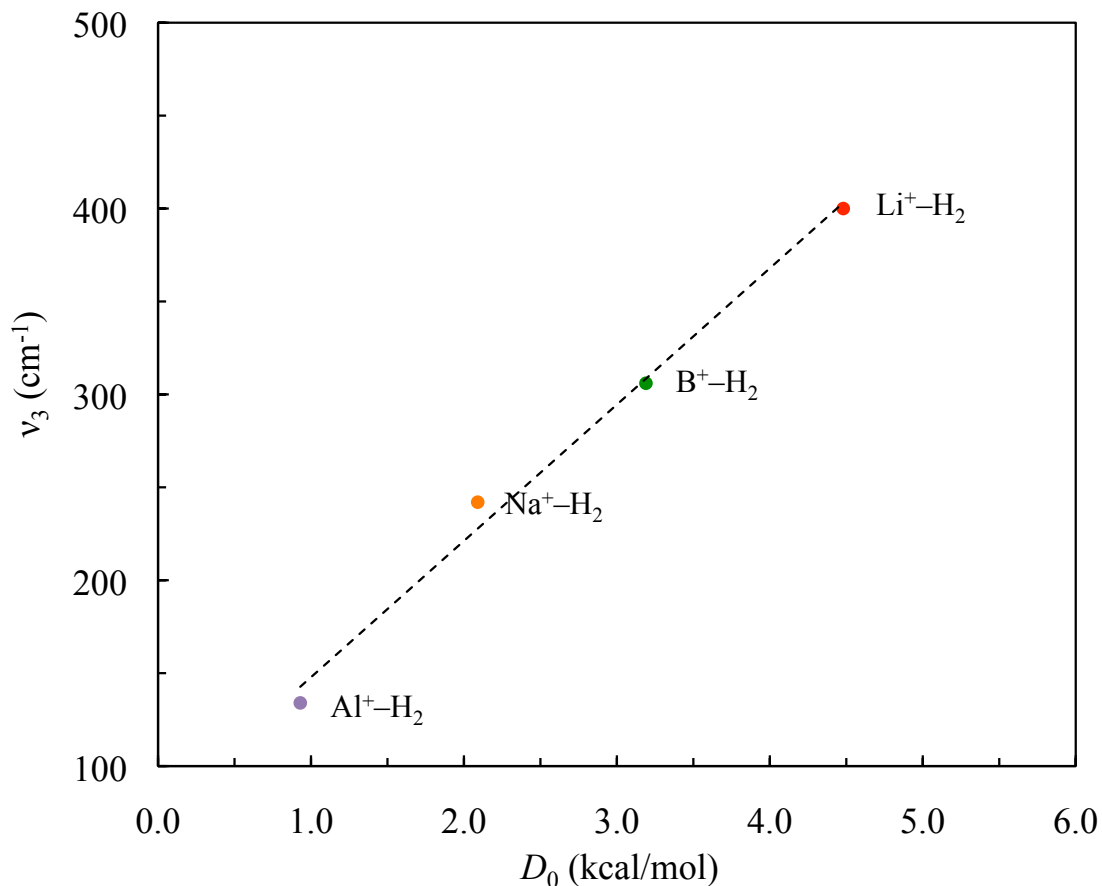
Figure 4. The graph of M^+–H_2 symmetric stretching frequency (v_3) vs. the ZPE-corrected binding energy (D_0) for Li^+–H_2 (red), B^+–H_2 (green) Na^+–H_2 (yellow), and Al^+–H_2 (purple) complexes computed at CCSD(T) level of theory with cc-pVTZ basis set. The binding energies (D_e) of the M^+–H_2 complexes are calculated as follows. The D_e = [Total Energy (M^+ and H_2 fragments)] − [Total Energy (M^+–H_2 molecule)]. The zero-point energy corrections (ΔZPE) are calculated using PT2-VSCF frequencies. The ZPE-corrected binding energy (D_0) is given as the sum of D_e and ΔZPE.
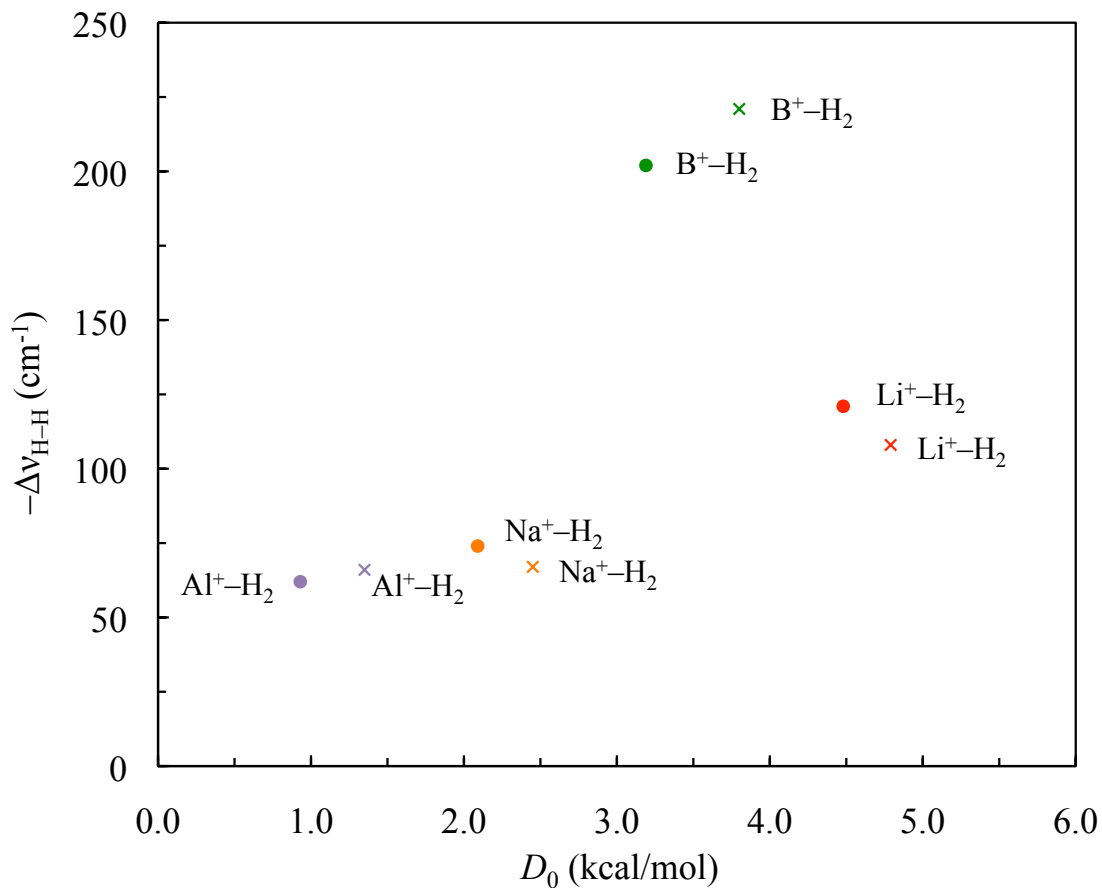
Figure 5. Graph of CCSD(T)/cc-pVTZ H–H stretching frequency red shifts ($-\Delta v_{H-H}$) vs. the ZPE-corrected binding energy (D_0) for Li^+–H_2 (red), B^+–H_2 (green) Na^+–H_2 (yellow), and Al^+–H_2 (purple) complexes computed at basis set. The binding energies (D_e) of the M^+–H_2 complexes are calculated as follows. The calculated values are displayed in circles and the experimental values are displayed in crosses.
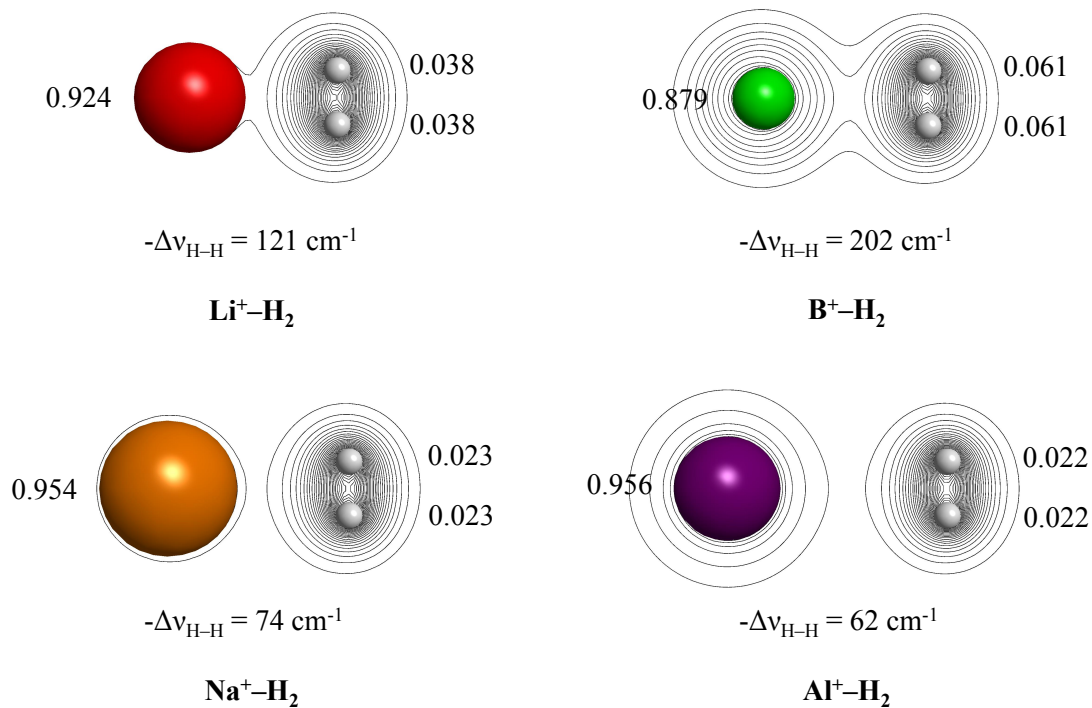
Figure 6. The total electron density maps and the electrostatic potential (ESP)-derived MP2/cc-pVTZ atomic charges for each of the studied complexes.

CHAPTER 3. ANHARMONICITY OF WEAKLY BOUND
Li$^+$−(H$_2$)$_n$ (n = 1−3) COMPLEXES

A paper published in *The Journal of Physical Chemistry A*

Nuwan De Silva, Bosiljka Njegic, and Mark S. Gordon

Abstract

The anharmonicity of Li$^+$–(H$_2$)$_n$ (n = 1, 2, and 3) complexes is studied using the vibrational self-consistent field (VSCF) approach. The H–H stretching frequency shifts of Li$^+$–(H$_2$)$_n$ complexes are calculated with the coupled-cluster method including all single and double excitations with perturbative triples (CCSD(T)) level of theory with the cc-pVTZ basis set. The calculated IR active H–H stretching frequency in Li$^+$–H$_2$, Li$^+$–(H$_2$)$_2$ and Li$^+$–(H$_2$)$_3$ is red shifted by 121, 109 and 96-99 cm^{-1}, respectively, relative to that of isolated H$_2$. The calculated red shifts and their trends are in good agreement with the available experimental data.

I. Introduction

In recent years, hydrogen has been considered to be a promising fuel source that could meet the future demand for a clean and renewable form of energy.[1,2] However, the lack of suitable materials for the storage of molecular hydrogen is a challenge that needs

to be resolved. Absorbing molecular hydrogen into solid storage materials such as metal hydrides,[3] complex hydrides,[4] metal organic frameworks (MOF),[5] and metal cation-doped zeolites[6] is a promising technique to overcome the storage problem.

There is great interest in developing a viable hydrogen storage material for hydrogen powered vehicles which contain a gravimetric density of about 6 wt % hydrogen.[2] Since the Li atom is lightweight, various Li-doped materials have been proposed. For instance, Denq *et al.* suggested a new Li-doped pillared single-wall carbon nanotube.[7] Furthermore, lithium cation-dihydrogen ($Li^+–(H_2)_n$) complexes are simple charged polyatomic molecules that are important for the hydrogen storage problem. The charge-quadrupole interaction between the charge on the Li^+ and the quadrupole moment of the H_2 ($^1\Sigma_g^+$) can be useful to understand the various aspects of the design or development of novel materials for hydrogen storage.[3-6]

The properties of $Li^+–(H_2)_n$ complexes have been studied experimentally and theoretically. Experimentally, Bieske, *et al.* have reported rotationally resolved infrared spectra of $Li^+–(H_2)_n$ ($n=1–3$) complexes in the H–H stretch region.[8] They found that the $Li^+–(H_2)_n$ ($n=1–3$) complexes exhibit a H–H stretch band with a center that is red-shifted by 108, 106, and 100 cm^{-1}, for $n = 1$, 2, 3, respectively, relative to the stretching fundamental frequency of the bare H_2 molecule.

Theoretically, Rao *et al.* have carried out a study using Hartree−Fock (HF) and fourth-order perturbation theory (MP4) with the 6-311G** basis set to explore the amount and nature of hydrogen uptake by both the neutral and cationic forms of Li.[9] Rao *et al.* have found that the Li^+ ion can hold at least six H_2 molecules in the first solvation (storage) shell. Davy *et al.* have studied the geometry, vibrational frequencies and complexation energies of Li^+–$(H_2)_n$ clusters up to four H_2 molecules using the coupled cluster method, including all single and double excitations (CCSD) with the 6-311G(d,p) basis set.[10] Davy *et al.* have reported the zero point energy (ZPE) corrected bond dissociation energy (D_0) of complexation is in the range 2.74−4.32 kcal mol^{-1} per H_2 molecule. The Li^+ cation was shown to be able to bind up to six H_2 molecules with a mean bond dissociation energy (D_e) of 4.77 kcal mol^{-1} at the MP2/6-311G(d,p) level of theory.[11]

A previous study[12] by the authors analyzed the anomalous trends in the vibrational spectra of a series of M^+–H_2 (M^+ = Li^+, Na^+, B^+, and Al^+) complexes using the vibrational self-consistent field (VSCF) method,[13-16] augmented by second order perturbation theory (PT2-VSCF).[17] In the present work, the PT2-VSCF approach is employed to study molecular hydrogen clustering around the Li^+ cation. The aim of the current work is to compare the structures of the Li^+-hydrogen clusters and the associated vibrational spectra. The results are compared with the experimental vibrational data, including the bond lengths, the frequency of the H−H stretching mode, and the binding energies. The organization of the paper is as follows. Section II describes the

computational details. In section III, the geometries and complexation energies and the anharmonic frequencies of the Li^+–$(H_2)_n$ complexes are discussed. Concluding remarks are summarized in section IV.

II. Computational Details

All calculations were performed using the GAMESS[18,19] electronic structure code, and molecules were visualized with MacMolPlt.[20] Electronic structure calculations were performed on Li^+–H_2, Li^+–$(H_2)_2$ and Li^+–$(H_2)_3$ using the coupled-cluster method including all single and double excitations with perturbative contributions from connected triple excitations (CCSD(T))[21,22] with the cc-pVTZ [23] basis set.

The geometry optimizations were carried out in C_{2v}, D_{2d} and D_3 symmetries, respectively, for the Li^+–H_2, Li^+–$(H_2)_2$ and Li^+–$(H_2)_3$. The CCSD(T) geometry optimizations were performed using numerical gradients. The optimized structures were tightly converged with the largest component of the numerical gradient less than 0.00001 Hartree/Bohr. The Hessian (matrix of energy second derivatives) was calculated and diagonalized at the optimized geometries. Hessians were calculated fully numerically with a 0.010 Bohr displacement step size for the Li^+–H_2 and Li^+–$(H_2)_3$ molecules and a 0.001 Bohr displacement step size for the Li^+–$(H_2)_2$ molecule at the CCSD(T)/cc-pVTZ level of theory. All stationary points were characterized as true minima by confirming that the corresponding Hessian is positive definite.

To obtain the anharmonic frequencies, PT2-VSCF calculations were carried out on the potential energy surface (PES) that was generated on a 16×16 points grid, by making displacements along normal mode vectors expressed as a sum of simple internal coordinate contributions.[24] For Li^+–H_2 three bonds were used to describe the normal modes.[12] For Li^+–$(H_2)_2$ six bonds, an angle, and two dihedral angles were used. The Li^+–$(H_2)_3$ complex was described by the nine bonds, two angles, and four dihedral angles. A series of calculations were carried out in which the spacing of the PES grid points along each vibrational mode was systematically increased until the diagonal frequencies converged, as described by Njegic and Gordon.[25] As described previously,[12] special care was used for all of the Li^+–H antisymmetric stretching modes of the Li^+–$(H_2)_n$ complexes.

The IR and Raman intensities were evaluated using the nuclear derivatives of the dipole moment and the static polarizability, respectively, at the HF/cc-pVTZ level using the CCSD(T)/cc-pVTZ optimized geometries. To obtain bond dissociation energies that can be related to experiment, D_0, ZPE corrections have been obtained using the anharmonic frequencies (PT2-VSCF) at the CCSD(T)/cc-pVTZ level of theory.

III. Results and Discussion

As shown in Figure 1, the Li^+–H_2, Li^+–$(H_2)_2$ and Li^+–$(H_2)_3$ complexes adopt C_{2v}, D_{2d} and D_3 structures, respectively, at the CCSD(T)/cc-pVTZ level of theory. Li^+–H_2 has a T-shaped structure (C_{2v}). In Li^+–$(H_2)_2$, the H_2 subunits are in a T-shaped arrangement opposite to Li^+ and perpendicular to each other (D_{2d}), with their centers of mass located on a straight line that passes through the Li center. In Li^+–$(H_2)_3$, the three H_2 sub units are tilted relative to each other (D_3), and their centers of mass are the vertices of an equilateral triangle. In the three Li^+–$(H_2)_n$ complexes the centers of mass of the H_2 subunits are distributed over a sphere around the Li^+ in such a way that the repulsion among H_2 subunits is minimized.

Table 1 summarizes selected CCSD(T)/ cc-pVTZ optimized geometric parameters. The distance between Li^+ and the H–H bond midpoint (R) increases with the size of the Li^+–$(H_2)_n$ cluster. The R values are obtained experimentally via vibrationally averaged separations (R_0), whereas calculated values are equilibrium separations (R_e). As one would expect, R_0 is larger than R_e. The H–H bond length changes (Δr_{HH}) are quoted relative to isolated H_2, whose calculated bond distance is 0.743 Å. The H–H and Δr_{HH} distances decrease as the size of the Li^+–$(H_2)_n$ cluster increases. Successive addition of the second and third H_2 molecules leads to a slight progressive weakening of the $Li^{+\cdots}H_2$ bonds, as seen by the 0.0041 and 0.0053 Å increases in the intermolecular bond lengths.

The calculated CCSD(T)/cc-pVTZ harmonic, anharmonic (VSCF-PT2) vibrational frequencies, IR and Raman intensities along with other available published calculations and experimental data are tabulated in Tables 2 (for $n = 1,2$) and 3 (for $n = 3$) for the $Li^+-(H_2)_n$ complexes. All three vibrational modes of Li^+-H_2 are assigned as stretching modes. The $Li^+-(H_2)_2$ complex has six stretching, two bending, and a torsional mode. The $Li^+-(H_2)_3$ complex has nine stretching, three bending, and three torsional modes. In general, $3n$ symmetric stretching modes can be identified in the $Li^+-(H_2)_n$ complexes, where n is the number of H_2 molecules in the complex.

The vibrational normal mode vectors of the Li^+-H_2, $Li^+-(H_2)_2$, and $Li^+-(H_2)_3$, are shown in Figures 2, 3, and 4, respectively. The three normal mode vectors of Li^+-H_2 are H–H symmetric stretching (v_1), Li^+-H antisymmetric stretching (v_2), and Li^+-H symmetric stretching (v_3). In general, there are n H–H stretching modes and $2n$ Li^+-H stretching modes in each $Li^+-(H_2)_n$ complex. The rest of the vibrational modes (for $n = 2$, 3) are bending or torsional modes.

Vibrational molecular motions in $Li^+-(H_2)_n$ clusters can be assigned, based on the normal mode vectors, to one of the following three main vibrational regions: H–H stretch ($\sim$4000 cm^{-1}), Li^+-H_2 stretch ($\sim$500 cm^{-1}), and bending and torsion (below $\sim$100 cm^{-1}). There is excellent agreement (within 20 cm^{-1}) of the PT2-VSCF frequencies with the available experimental data. Upon the addition of the second and third H_2 molecules, the slight increase in the intermolecular bond length is consistent with the trend in the

calculated H–H stretching (A_1) PT2-VSCF frequencies [$n = 1$: 4045 cm^{-1}; $n = 2$: 4058 cm^{-1}; $n = 3$: 4081 cm^{-1}]. In each Li$^+$–(H$_2$)$_n$ complex, the highest H–H harmonic stretching frequency undergoes an anharmonic shift (relative to the harmonic frequencies) of about 200 cm^{-1}, which is the largest anharmonicity associated with any particular mode.

The highest vibrational frequency mode of Li$^+$–(H$_2$)$_2$ and Li$^+$–(H$_2$)$_3$ is Raman active but IR inactive. The Raman scattering of the highest vibrational frequency increases as n increases. The H–H stretching modes for the Li$^+$–(H$_2$)$_n$ complexes with A_1, B_2, and E symmetry are both IR and Raman active. The IR active H–H stretching mode gives the most intense IR peak in each of the Li$^+$–(H$_2$)$_n$ complexes.

Table 4 shows the CCSD(T)/cc-pVTZ calculated IR active H–H frequency shifts of the Li$^+$–(H$_2$)$_n$ complexes. Harmonic red shifts are calculated with respect to harmonic frequencies of the isolated H$_2$ (4409 cm^{-1}). The PT2-VSCF red shifts are calculated with respect to the diagonal frequencies of isolated H$_2$ (4166 cm^{-1}). The experimental H–H stretching frequency of molecular H$_2$ is 4161.17 cm^{-1}.[26] The VSCF-PT2 frequencies capture the trends in the experimental red shifts both qualitatively and quantitatively. Relative to the isolated H$_2$ molecule, the calculated PT2-VSCF red shifts for Li$^+$–H$_2$, Li$^+$–(H$_2$)$_2$, and Li$^+$–(H$_2$)$_3$ are 121 cm^{-1}, 109 cm^{-1} and 96-99 cm^{-1}, respectively, at the CCSD(T)/cc-pVTZ level of theory.

The binding energies per H_2 (D_e) of the $Li^+–(H_2)_n$ complexes are calculated as D_e = ([total energy (Li^+ and H_2 fragments)] – [total energy ($Li^+–(H_2)_n$ complex)])/n. The zero point energy corrections per H_2 (ΔZPE) are calculated using the PT2-VSCF frequencies. The ZPE-corrected binding enthalpy per H_2 (D_0) is the sum of D_e and ΔZPE. The CCSD(T)/cc-pVTZ $Li^+–(H_2)_n$ binding energies are given in Table 5. The calculated D_0 and other calculated data in the literature are in good agreement. According to Table 5, for all of the complexes studied, D_0 decreases, as expected, with an increasing number of H_2 units. This trend is consistent with the increase in the R_e of the complex with an increasing number of H_2 units. The vibrational information also reveals how the extent of the H–H intramolecular interactions is related to that of the corresponding $Li^+–H_2$ bond. A stronger $Li^+–H_2$ bond implies that electron density is transferred from the H_2 to the Li^+, which results in a weakening of the H–H bond, and, therefore, a softer H–H stretching mode. According to the calculated interaction energies, one would predict that the red shift associated with the H–H stretching frequency varies in the order $Li^+–(H_2)_3 < Li^+–(H_2)_2 < Li^+–H_2$ due to the delocalization of the H–H electron density toward the metal cation, with a consequent weakening of the H–H bond, compared to the free H_2 molecule. Addition of H_2 units to the system reduces the delocalization contribution per H_2 toward the Li^+. For instance, the highest H–H stretching frequency of a given complex is lower than the free H–H stretching frequency, but as the number of H_2 subunits increases, that frequency approaches that of the free molecule.

IV. Conclusions

The PT2-VSCF approach is employed at the CCSD(T) level of theory to compute the vibrational spectrum of $Li^+–(H_2)_n$ complexes, for $n = 1, 2, 3$. The H_2 subunits are predicted to be weakly bound (~5 kcal/mol) to the lithium cation. The strength of the metal-H_2 complex interaction mainly depends on the number of H_2 subunits attached to the metal cation, where the interaction decreases with increasing n. The calculated H–H frequency red shifts are in good agreement with the available experimental data. The downward shifts of the H–H frequency are correlated with the complexation energy per H_2. The H–H stretching frequency varies according to the delocalization of the H–H electron density toward the metal cation and the consequent weakening of the H–H bond, compared to the frequency of the isolated H_2 molecule. The amount of delocalization of the electron density per H_2 subunit towards the metal cation decreases with n, resulting in a less red-shifted H–H stretching frequency.

In the $Li^+–(H_2)_n$ complexes ($n = 1,2,3$), the modest 5 kcal/mol interaction energy might be suitable for a hydrogen storage system with favorable H_2 loading and unloading kinetics. In order to load or unload the H_2 to/from the Li^+, one needs to pay attention to the $Li^+–H$ stretching modes. Among the $Li^+–H$ stretching modes, the most IR active modes (v_3 of $Li^+–H_2$, v_5 of $Li^+–(H_2)_2$, and degenerate v_7 and v_8 of $Li^+–(H_2)_3$), are responsible for dissociation of an H_2 from the Li^+ Therefore, one might increase the

temperature or provide the correct amount of energy to the most IR active Li^+–H stretching modes in order to release H_2 and vice versa.

Acknowledgements

References

(1)   Coontz, R.; Hanson, B. *Science* **2004**, *305*, 957-957.

(2)   Schlapbach, L.; Zuttel, A. *Nature* **2001**, *414*, 353-358.

(3)   Grochala, W.; Edwards, P. P. *Chem. Rev.* **2004**, *104*, 1283-1315.

(4)   Orimo, S. I.; Nakamori, Y.; Eliseo, J. R.; Zuttel, A.; Jensen, C. M. *Chem. Rev.* **2007**, *107*, 4111-4132.

(5)   Mulder, F. M.; Dingemans, T. J.; Schimmel, H. G.; Ramirez-Cuesta, A. J.; Kearley, G. J. *Chem. Phys.* **2008**, *351*, 72-76.

(6)   Vitillo, J. G.; Damin, A.; Zecchina, A.; Ricchiardi, G. *J. Chem. Phys.* **2005**, *122*, 114311-114310.

(7)   Deng, W. Q.; Xu, X.; Goddard, W. A. *Phys. Rev. Lett.* **2004**, *92*, 166103-166106.

(8)   Emmeluth, C.; Poad, B. L. J.; Thompson, C. D.; Weddle, G. H.; Bieske, E. J. *J. Chem. Phys.* **2007**, *126*, 204309-204309.

(9)   Rao, B. K.; Jena, P. *Europhys. Lett.* **1992**, *20*, 307-312.

(10)   Davy, R.; Skoumbourdis, E.; Kompanchenko, T. *Mol. Phys.* **1999**, *97*, 1263-1271.

(11)   Barbatti, M.; Jalbert, G.; Nascimento, M. A. C. *J. Chem. Phys.* **2001**, *114*, 2213-2218.

(12)   De Silva, N.; Njegic, B.; Gordon, M. S. *J. Phys. Chem. A* **2011**, *115*, 3272-3278.

(13)   Chaban, G. M.; Jung, J. O.; Gerber, R. B. *J. Chem. Phys.* **1999**, *111*, 1823-1829.

(14)   Yagi, K.; Taketsugu, T.; Hirao, K.; Gordon, M. S. *J. Chem. Phys.* **2000**, *113*, 1005-1017.

(15)   Yagi, K.; Hirao, K.; Taketsugu, T.; Schmidt, M. W.; Gordon, M. S. *J. Chem. Phys.* **2004**, *121*, 1383-1389.

(16)   Matsunaga, N.; Chaban, G. M.; Gerber, R. B. *J. Chem. Phys.* **2002**, *117*, 3541-3547.

(17)   Jung, J. O.; Gerber, R. B. *J. Chem. Phys.* **1996**, *105*, 10332-10348.

(18)   Gordon, M. S.; Schmidt, M. W. *Theory and Applications of Computational Chemistry: The First Forty Years*; Elsevier: Amsterdam, The Netherlands, 2005.

(19)   Schmidt, M. W.; Baldridge, K. K.; Boatz, J. A.; Elbert, S. T.; Gordon, M. S.; Jensen, J. H.; Koseki, S.; Matsunaga, N.; Nguyen, K. A.; Su, S. J.; Windus, T. L.; Dupuis, M.; Montgomery, J. A. *J. Comput. Chem.* **1993**, *14*, 1347-1363.

(20)   Bode, B. M.; Gordon, M. S. *J. Mol. Graphics Modell.* **1998**, *16*, 133-138.

(21)   Piecuch, P.; Kucharski, S. A.; Kowalski, K.; Musial, M. *Comput. Phys. Commun.* **2002**, *149*, 71-96.

(22)   Raghavachari, K.; Trucks, G. W.; Pople, J. A.; Head-Gordon, M. *Chem. Phys. Lett.* **1989**, *157*, 479-483.

(23)   Dunning, T. H. *J. Chem. Phys.* **1989**, *90*, 1007-1023.

(24)   Njegic, B.; Gordon, M. S. *J. Chem. Phys.* **2006**, *125*, 224102-224112.

(25)   Njegic, B.; Gordon, M. S. *J. Chem. Phys.* **2008**, *129*, 164107-164113.

(26)   Bragg, S. L.; Brault, J. W.; Smith, W. H. *Astrophysical Journal* **1982**, *263*, 999-1004.

(27)   Sanz, C.; Bodo, E.; Gianturco, F. A. *Chem. Phys.* **2005**, *314*, 135-142.

(28)   Kraemer, W. P.; Spirko, V. *Chem. Phys.* **2006**, *330*, 190-203.

Table 1. Selected CCSD(T) geometric parameters of Li^+–$(H_2)_n$ complexes, with the cc-pVTZ basis set

Molecule	$R_e(Å)^{a,b}$	$R_0(Å)^{a,b}$	$r_{HH}(Å)$	$\Delta r_{HH}(Å)^c$
Li^+–H_2	2.0181^d	2.056^e	0.7514^d	0.0087^d
Li^+–$(H_2)_2$	2.0222		0.7511	0.0084
Li^+–$(H_2)_3$	2.0275		0.7506	0.0079

[a] The distance between Li^+ and the midpoint along H−H bond.

[b] Experimental values are R_0; calculated values are R_e.

[c] H−H bond length (r_{HH}) changes (Δr_{HH}) are taken relative to isolated H_2. The isolated H−H bond distances is 0.7427 Å at CCSD(T) with the cc-pVTZ basis.

[d] Reference [12].

[e] Reference[8].

Table 2. CCSD(T)/ cc-pVTZ vibrational frequencies (cm^{-1}) of $Li^+–H_2$ and $Li^+–(H_2)_2$

Molecule	Symmetry			IR intensity (Debye^2/amu-Å^2)	Raman intensity (Å^4/amu)	Harmonic frequency	PT2-VSCF frequency	Experimental frequency
$Li^+–H_2$								
ν_1	A_1	H–H	sym str	11.3	170.3	4291	4045[a]	4053[b]
ν_2	B_1	Li^+–H	antisym str	0.1	15.9	695	652[a]	646[c]
ν_3	A_1	Li^+–H	sym str	2.7	10.0	478	400[a]	426[c]
$Li^+–(H_2)_2$								
ν_1	A_1	H–H	sym str	0.0	264.9	4295	4058	
ν_2	B_2	H–H	antisym str	13.6	40.7	4293	4057	4055[b]
ν_3	E	Li^+–H	antisym str	0.1	12.4	690	643	
ν_4	E	Li^+–H	antisym str	0.1	12.4	690	642	
ν_5	B_2	Li^+–H	antsym str	3.3	0.2	521	461	
ν_6	A_1	Li^+–H	sym str	0.0	8.6	420	365	
ν_7	B_1	torsion		0.0	28.5	66	24	
ν_8	E	H_2–Li^+–H_2 bend		2.1	0.6	40	21	
ν_9	E	H_2–Li^+–H_2 bend		2.1	0.6	40	22	

[a] Reference[12]. [b] Reference[8]. [c] Reference[27].

Table 3. CCSD(T)/ cc-pVTZ vibrational frequencies (cm^{-1}) of Li$^+$–(H$_2$)$_3$

Molecule	Symmetry			IR intensity (Debye^2/amu-Å^2)	Raman intensity (Å^4/amu)	Harmonic frequency	PT2-VSCF frequency	Experimental frequency
Li$^+$–(H$_2$)$_3$								
ν_1	A_1	H–H	sym str	0.0	368.8	4302	4081	
ν_2	E	H–H	antisym str	7.2	30.1	4300	4067	4060[a]
ν_3	E	H–H	antisym str	7.2	30.1	4300	4070	4060[a]
ν_4	E	Li$^+$–H	antisym str	0.1	16.3	686	630	
ν_5	E	Li$^+$–H	antisym str	0.1	16.3	686	627	
ν_6	A_2	Li$^+$–H	antisym str	0.2	0.0	680	615	
ν_7	E	Li$^+$–H	antisym str	2.0	2.2	482	444	
ν_8	E	Li$^+$–H	antisym str	2.0	2.2	482	440	
ν_9	A_1	Li$^+$–H	sym str	0.0	23.8	406	337	
ν_{10}	A_1	torsion		0.0	6.6	70	69	
ν_{11}	E	H$_2$–Li$^+$–H$_2$ bend		0.0	5.9	69	65	
ν_{12}	E	H$_2$–Li$^+$–H$_2$ bend		0.0	5.9	69	68	
ν_{13}	A_2	H$_2$–Li$^+$–H$_2$ bend		1.8	0.0	46	55	
ν_{14}	E	torsion		0.6	0.4	24	13	
ν_{15}	E	torsion		0.6	0.4	24	20	

[a] Reference[8].

Table 4. Calculated CCSD(T)/cc-pVTZ H–H symmetric stretching frequency red shifts (cm^{-1}) of Li$^+$–(H$_2$)$_n$ complexes[a]

Molecule	harmonic	PT2-VSCF	experimental[b]
Li$^+$–H$_2$	119	121	108
Li$^+$–(H$_2$)$_2$	116	109	106
Li$^+$–(H$_2$)$_3$	109	96-99	100

[a] Harmonic red shifts are calculated with respect to the harmonic frequency of isolated H$_2$ (4409 cm^{-1}). PT2-VSCF red shifts are calculated with respect to the diagonal frequency of isolated H$_2$ (4166 cm^{-1}).

Table 5. CCSD(T)/cc-pVTZ ZPE-corrected binding energy (D_0) per H_2 in kcal/mol for the $Li^+-(H_2)_n$ complexes.

	Li^+-H_2	$Li^+-(H_2)_2$	$Li^+-(H_2)_3$
D_e	5.81	5.70	5.57
ΔZPE	1.33	1.45	1.55
D_0	4.48[a]	4.26	4.02
Other calculations D_0	4.79[b] 4.32[c]	4.02[c]	3.74[c]

[a] Reference[12].

[b] From rovibrational calculations.[28]

[c] From CCSD/6-311G(d,p) calculations; ZPE correction with harmonic frequencies.[10]
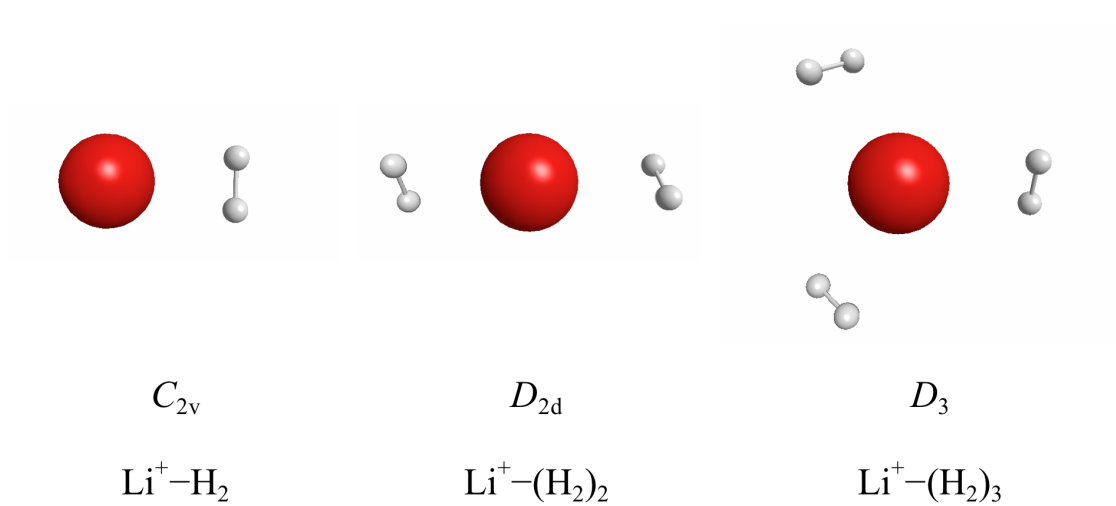
Figure 1. Optimized geometries of $Li^+-(H_2)_n$ complexes computed at CCSD(T) level of theory with cc-pVTZ basis set.
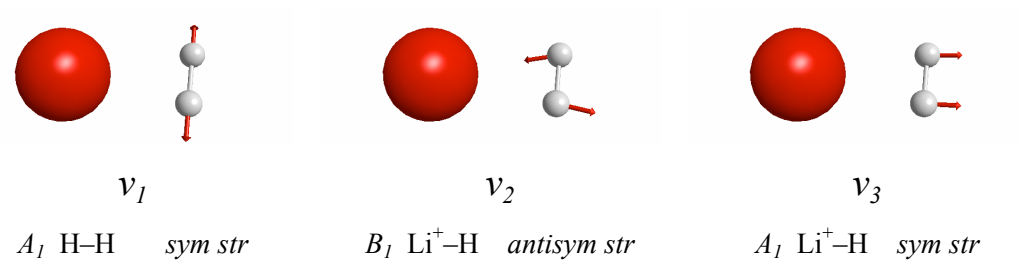
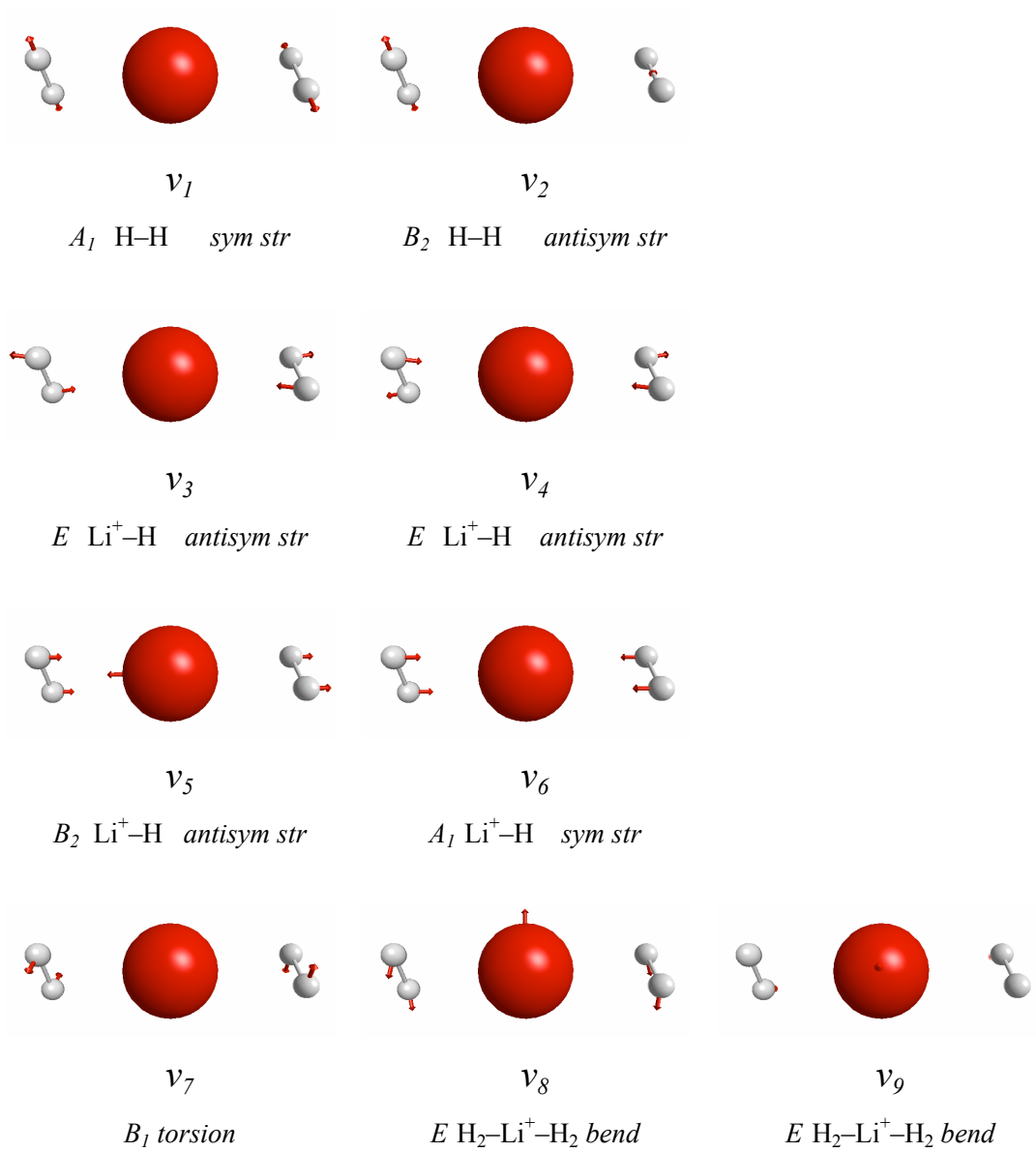**Figure 2**. Vibrational normal mode vectors of Li^+-H_2

v_1

A_1 H–H   *sym str*

v_2

B_2 H–H   *antisym str*

v_3

E Li$^+$–H   *antisym str*

v_4

E Li$^+$–H   *antisym str*

v_5

B_2 Li$^+$–H   *antisym str*

v_6

A_1 Li$^+$–H   *sym str*

v_7

B_1 *torsion*

v_8

E H$_2$–Li$^+$–H$_2$ *bend*

v_9

E H$_2$–Li$^+$–H$_2$ *bend*

Figure 3. Vibrational normal mode vectors of Li$^+$–(H$_2$)$_2$
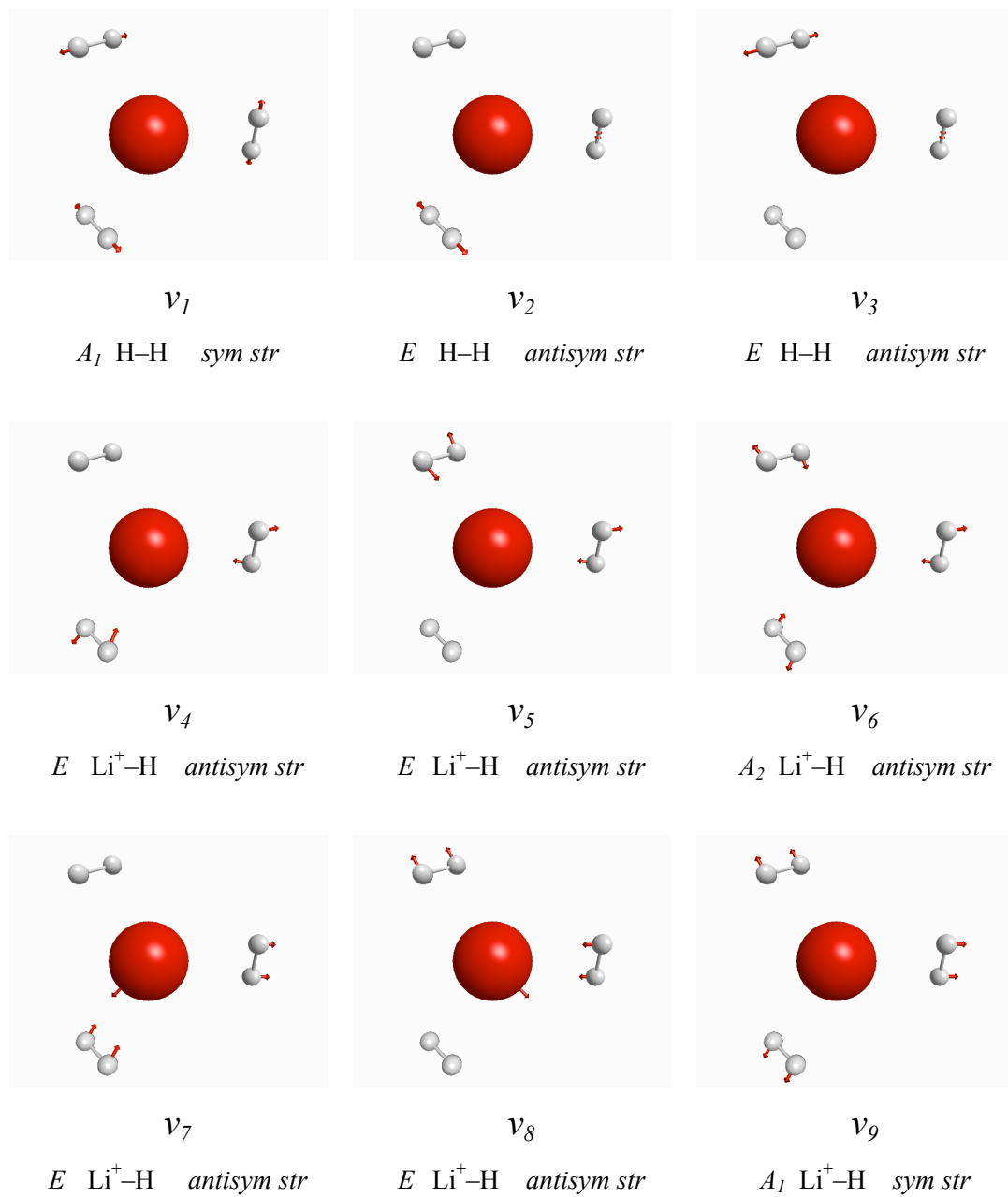
Figure 4. Vibrational normal mode vectors of $Li^+-(H_2)_3$

v_{10}

A_1 torsion

v_{11}

E H$_2$–Li$^+$–H$_2$ bend

v_{12}

E H$_2$–Li$^+$–H$_2$ bend

v_{13}

A_2 H$_2$–Li$^+$–H$_2$ bend
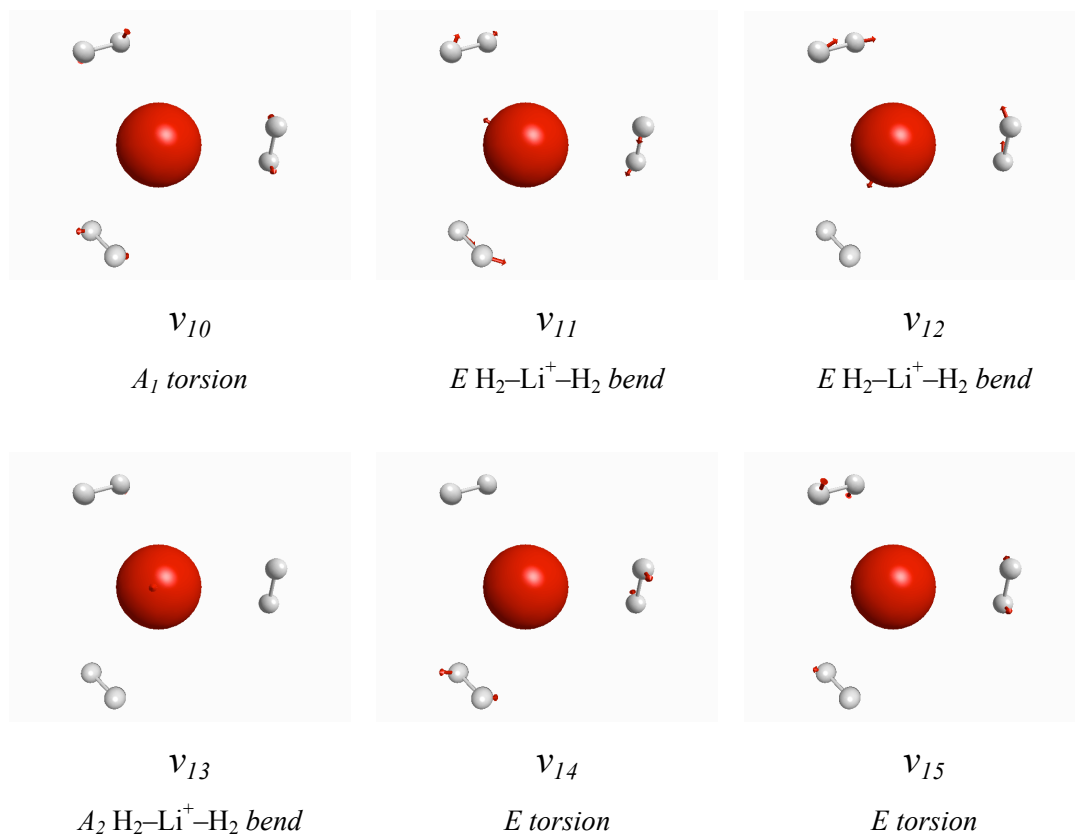
v_{14}

E torsion

v_{15}

E torsion

Figure 4. (continued)

CHAPTER 4. SOLVENT INDUCED SHIFTS IN THE UV SPECTRUM OF AMIDES

A paper published in *The Journal of Physical Chemistry A*

Nuwan De Silva, Soohaeng Y. Willow, and Mark S. Gordon

Abstract

Solvent effects on the electronic spectra of formamide and *trans*-N-methylacetamide are studied using four different levels of theory: singly excited configuration interaction (CIS), equations of motion coupled-cluster theory with singles and doubles (EOM-CCSD), completely renormalized coupled-cluster theory with singles and doubles with perturbative triple excitations (CR-EOM-CCSD(T)), and time dependent density functional theory (TDDFT), employing small clusters of water molecules. The simulated electronic spectrum is obtained via the molecular dynamics simulations with 100 waters modeled with the effective fragment potential method and exhibits a blue-shift and red-shift, respectively, for the $n{\rightarrow}\pi^*$ and $\pi_{\mathrm{nb}}{\rightarrow}\pi^*$ vertical excitation energies, in good agreement with the experimental electronic spectra of amides.

I. Introduction

The study of solvent effects on the electronic absorption spectra of amides provides an excellent benchmark for implementing an accurate solvent representation of proteins. Therefore, the electronic transition energies of formamide (HCONH2) and trans-N-methylacetamide (NMA) have been of considerable interest, both experimentally[1-6] and theoretically.[7-12] The previous studies were motivated by the role of amides as a model for the underlying repeating unit in protein backbones. $HCONH_2$ is an important prototype molecule, being the simplest unsubstituted unit to contain the peptide linkage in proteins. Meanwhile, NMA can serve as the simplest substituted unit in the peptide linkage. $HCONH_2$ and NMA provide an important prototype for the calculation and interpretation of electronic excitation energies of proteins. Interactions between these prototype molecules and surrounding water molecules can give insight into the complex intermolecular interactions that occur when proteins are solvated.

Experimentally, the gas phase electronic spectra of amides are well understood. In general, amides exhibit five main absorption bands in the gas phase:[2] (1) an intense band, the V_1 band, due to the $\pi_{nb} \rightarrow \pi^*$ transition; (2) a less intense band, the W band (due to the $n \rightarrow \pi^*$ transition); (3), (4) two sharp bands, R_1 and R_2 (due to Rydberg transitions); and (5) a Q band (due to Rydberg transitions with a superposition of two Rydberg states).[6,13,14]

The absorption spectra of amides in the condensed phase exhibits interesting solvatochromic effects depending on the type of amide and the solvent. In the electronic absorption spectrum of $HCONH_2$ in aqueous solution the $n{\rightarrow}\pi^*$ and $\pi_{nb}{\rightarrow}\pi^*$ transitions were found to be blue- and red-shifted by 0.27 and 0.50 eV, respectively, relative to the gas phase $HCONH_2$.[4,5] Nielsen and Schellman[4] measured the absorption curves for a series of amides including NMA in cyclohexane and water. The position of the $\pi_{nb}{\rightarrow}\pi^*$ band in NMA was measured, and a very small red-shift was observed when changing the solvent from cyclohexane to water (0.07 eV). Considering the $\pi_{nb}{\rightarrow}\pi^*$ excitation energy of NMA in gas phase (6.81 eV) measured by Kaya $et.\ al.$[3] and NMA in aqueous solution (6.67 eV) measured by Nielsen $et.\ al.$[4], a 0.14 eV red-shift was observed in the aqueous phase. The experimental gas phase data for the $n{\rightarrow}\pi^*$ transition of NMA is not available. However, when NMA is placed in cyclohexane the $n{\rightarrow}\pi^*$ band appeared to be 5.46 eV,[15] and in aqueous solution, the $n{\rightarrow}\pi^*$ band shifted to 5.85 eV[4] with a 0.39 eV blue-shift. The electronic spectrum shifts in different directions and with different magnitudes, depending on the nature of the solvent and solute-solvent interactions.[16-18]

Two approaches are commonly used to model solvent effects, the continuum (implicit) approach[19,20] and the discrete (explicit) approach.[21,22] The continuum model requires some choice for the geometry of the molecular cavity, which is intended to reflect the size of the solvated molecule. Popular continuum methods include the polarizable continuum method (PCM),[20,23] the conductor-like screening model (COSMO)[24,25] the solvation model x (SMx),[26-28] where x denotes a specific

parametrization of a particular solvent model, the solvation with volume polarization (SVP)[29], and the self-consistent reaction field (SCRF) model.[30] A review article for the continuum solvation models can be found in references.[31,32] In the discrete approach, the individual solvent molecules are explicitly present, modeled either by some level of electronic structure theory or by a model potential. The individual solvent-solute interactions are explicitly accounted for.

Both the continuum and discrete approaches have advantages and disadvantages. The continuum approach is relatively fast and is designed to mimic bulk properties of the solution. However, the continuum approach does not describe the specific interactions (e.g., hydrogen bonds) between the solute and solvent molecules. In addition, the continuum approach can be very sensitive to the cavity parameters. The discrete approach treats solute-solvent interactions explicitly. However, the discrete approach generally requires extensive configurational sampling. Therefore, the discrete approach can be computationally demanding, especially if fully *ab initio* potentials are used.

Commonly used discrete methods include the effective fragment potential (EFP) method, the simple point charge/extended (SPC/E) method,[33] and the three-, four-, and five-point transferable intermolecular potentials (TIP3P, TIP4P, and TIP5P),[34,35] all-atom optimized potentials for liquid simulations (OPLS)-AA,[36] dissipative particle dynamics (DPD),[37] smooth particle hydrodynamics (SPH),[38] and the particle-based simulation technique[39] often called stochastic rotation dynamics (SRD).[40] The approach taken in the

present work for representing the solvent explicitly is the effective fragment potential method for water (EFP1).[41-43] The EFP1 method, which includes self-consistent polarization effects, has been shown to accurately treat the interactions between solute and solvent molecules.[44-55] The EFP1 method, a quantum mechanics (QM)-based method that includes self-consistent induction, was introduced to study aqueous solvent effects. Most of the above discrete methods can be considered to be variants of quantum mechanics/molecular mechanics (QM/MM) simulations in which the electronic structure of the solute is treated as QM and the solvent molecules are treated as MM.[56]

The physical properties of amide:solvent complexes, such as minima, hydrogen bond interactions, and the effect of hydration on the harmonic vibrational frequencies and internal rotation barrier, have been the subject of a large number of studies; e.g., $HCONH_2$:solvent[57-67] and NMA:solvent.[66,68-74] The computational modeling of solvent effects on the electronic spectra of amides[10,57-77] has primarily examined the effects of up to three explicit water molecules. The singly excited configuration interaction (CIS) method with a minimal STO-3G basis set was used to calculate the n-π^* excited state of $HCONH_2$ in the presence of one and two water molecules.[75] These authors concluded that the formation of a hydrogen bond with the carbonyl oxygen of $HCONH_2$ could destabilize the n-π^* state and change the magnitude of the blue-shifted $n\rightarrow\pi^*$ transition energy. The geometries of the ground state and the first excited singlet and triplet states of $HCONH_2$ *in vacuo* and in the presence of three EFP1 water molecules were explored by Krauss and Webb[76] using the multiconfigurational self-consistent-field (MCSCF)

method with the DH(d,p) basis set. The vertical transition of $HCONH_2$ *in vacuo* and in the presence of three EFP water molecules was reported to be 5.66 eV and 6.14 eV, respectively. It was also shown that the EFP1 water calculations accurately reproduced the fully *ab initio* excited state geometry and the interaction energy between $HCONH_2$ and water.

The complete active space self-consistent field (CASSCF) and multiconfigurational second-order perturbation theory (CASPT2) methods have been used to study the n-π* and π_{nb}-π* states of $HCONH_2$ with one water molecule, using a double-ζ plus polarization basis set.[10] Relative to isolated $HCONH_2$, the n-π* state was predicted to be blue-shifted by 0.18 eV upon the addition of a water molecule, while the π_{nb}-π* state was predicted to be red-shifted by 0.15 eV. The CASSCF and CASPT2 methods, with an ANO basis set, have also been used to calculate the ground state and excited state energies of $HCONH_2$ in the presence of one, two, and three water molecules.[67] The $HCONH_2$ with one, two, and three water molecules undergoes a blue-shift of 0.36, 0.48, and 0.50 eV, respectively, in the $n{\rightarrow}\pi$* transition, whereas the $\pi_{nb}{\rightarrow}\pi$* transition undergoes a red-shift of 0.15, 0.15, and 0.25 eV, respectively, relative to isolated $HCONH_2$.

Besley and Hirst[66] have reported a theoretical investigation of the solvent effects on the valence electronic spectra of NMA and $HCONH_2$ using the CASSCF and CASPT2 methods for the solute and a self-consistent reaction field model for the solvent. The

experimental $n{\rightarrow}\pi^*$ and $\pi_{nb}{\rightarrow}\pi^*$ excitation energies were reproduced to within 0.15 eV accuracy. A red-shift was predicted for the $\pi_{nb}{\rightarrow}\pi^*$ excitation energy. However, in contrast to the experimental data, no significant blue-shift was found for the $n{\rightarrow}\pi^*$ excitation energy. Recently, a polarizable embedding (PE) QM/MM method was developed by Olsen *et al.*[78] They have computed gas-to-aqueous solvent induced shifts of the lowest $n{\rightarrow}\pi^*$ vertical excitation energy in acetone and acrolein and the lowest $\pi{\rightarrow}\pi^*$ vertical excitation energy in acrolein, pyridine, uracil, coumarin 151, and coumarin 153. They have used a QM/MM (PE-DFT) approach in which the solute is treated using DFT (CAM-B3LYP functional) and the solvent molecules are represented by a PE potential. The aug-cc-pVDZ basis set was used in the calculations of excitation energies of all the moilecules except a smaller 6-31++G* basis was used in the calculations on coumarin 153. The PE model was applied by Sneskov *et al.* to the $n{\rightarrow}\pi^*$ and $\pi_{nb}{\rightarrow}\pi^*$ excitation energies of $HCONH_2$ and NMA in vacuum and water solution using the CCSDR(3 with the aug-cc-pVDZ basis set.[79] Even though Sneskov *et al.* predicted acceptable solvent-induced blue-shift $n{\rightarrow}\pi^*$ transitions in both $HCONH_2$ and NMA, they failed to predict the solvent-induced red-shift $\pi_{nb}{\rightarrow}\pi^*$ transitions in NMA within 0.15 eV accuracy. (The $\pi_{nb}{\rightarrow}\pi^*$ transition of NMA was predicted to give a large blue-shift (+ 0.67 eV) instead of a small red-shift.).

The temperature effects on the electronic spectra of amides ($HCONH_2$, N-methylformamide, acetamide, and NMA) have been studied using a combination of molecular dynamics (MD) simulations and TDDFT in the gas phase by Besley *et. al.*[77]

The valence n-π^* and π_{nb}-π^* states were both predicted to have temperature-induced red-shifts, 0.1−0.35 eV at 300 K, relative to 0 K. These authors have also calculated the electronic spectrum of $HCONH_2$ in the presence of 16 water molecules around each gas phase MD configuration. Overall, a blue-shift was predicted for the n-π^* state and red-shift was predicted for the π_{nb} -π^* state of $HCONH_2(H_2O)_{16}$, with respect to $HCONH_2$. The mean values for the n-π^* and π_{nb}-π^* excitation energies of $HCONH_2(H_2O)_{16}$ are blue and red -shifted by +0.52 eV and −0.33 eV, respectively, compared to the gas phase at 300 K. The authors also noted that structural changes in the amides contribute to the π_{nb}-π^* red-shift.

In the present study, solvent effects on the electronic absorption spectra of amides are considered for the $n{\rightarrow}\pi^*$ and $\pi_{nb}{\rightarrow}\pi^*$ vertical excitations. The $n{\rightarrow}\pi^*$ state originates primarily from a carbonyl oxygen lone pair n into the anti-bonding C=O π^* orbital. Experimentally the $n{\rightarrow}\pi^*$ excitation of amides exhibits a blue shift in an aqueous environment.[4,5] The $\pi_{nb}{\rightarrow}\pi^*$ excitation from a non-bonding π orbital into an anti-bonding π^* orbital is particularly interesting, since the $\pi_{nb}{\rightarrow}\pi^*$ transition has an intense band and exhibits a red-shift in an aqueous environment.[4,5] Since amides can act as models for the underlying repeating unit in a protein, understanding solvent effects on amides helps to design and develop an accurate solvent representation of proteins. In this article, a *qualitative* interpretation of solvent-induced shifts of amides is obtained via examination of the change in the solute HOMO and LUMO electronic energies of solute:water complexes at four different levels of theory: CIS, EOM-CCSD, CR-EOM-CCSD(T), and

TDDFT. QM/MM molecular dynamics simulations are employed to provide the simulated electronic spectrum and *quantitative* values of solvent-induced blue-shift and red-shift, respectively, for $n{\rightarrow}\pi^*$ and $\pi_{nb}{\rightarrow}\pi^*$ vertical excitations using an explicit solvent model. An important aspect of this article is to demonstrate that the sophisticated EFP method can capture the observed solvent shifts. This is important since EFP has been shown previously to predict ground state properties at a level that is equivalent to MP2.[49, 50, 80, 81]

II. Computational Details

For QM-EFP applications, an EFP1 water is described by one-electron potentials, representing electrostatic (Coulomb), induction (polarization), and exchange repulsion + charge transfer, that are added to the QM Hamiltonian. The Coulomb interaction is modeled with multipoles (through octopoles) located at atoms and bond midpoints. The polarization effects are described by dipole polarizability tensors located at the centroids of localized orbitals: bonds and lone-pairs. The repulsive terms (exchange repulsion + charge transfer) are represented by exponential functions placed at the atom centers and the center of mass, with the exponents fitted to the water dimer potential energy surface. There are two QM-EFP1 variants; Hartree-Fock (HF)-based (EFP1/HF)[41,42] and density functional theory (DFT)-based (EFP1/DFT).[43] The B3LYP[82,83] functional was used for the DFT version. Recently, Yoo *et al.*[44] interfaced time dependent density functional theory (TDDFT) with the EFP1/DFT model to describe the excited states of molecules

solvated by water. This combined TDDFT/EFP1/DFT method was used to calculate the solvent-induced shifts of molecular electronic excitations of acetone. The calculated solvent effect on the $n \rightarrow \pi^*$ vertical excitation energy is in good agreement with the experimental blue-shift.

All calculations in the present work are performed with the GAMESS[84,85] electronic structure code. First, the solute with one, two, and three water molecules located at the ground state global minima are fully optimized with second order perturbation theory (MP2)[86] and the 6-311++G(2d,2p) basis set, in C_1 symmetry.

Using the optimized geometries, vertical excitation energy calculations are carried out with CIS,[87] equations of motion coupled-cluster with singles and doubles (EOM-CCSD),[88] completely renormalized coupled cluster theory with single and double and perturbative triple excitations (CR-EOMCCSD(T)),[89] and TDDFT[90,91] with the PBE0 functional and using the cc-pVDZ[92,93] basis set. Only vertical singlet-to-singlet transitions are considered here.

The hybrid QM/EFP scheme is employed to calculate the solvent induced shifts of the amides.[44] The solute is treated quantum mechanically using DFT and the PBE0 functional with the cc-pVDZ basis set. The solvent is treated using EFP1/DFT 100 solvent water molecules. Therefore, MD simulations with 100 waters explicitly modeled with the EFP method in GAMESS can be described as a QM/MM (PBE0/EFP1) variant.

The MD simulations were carried out for both the gas phase and the aqueous phase (100 EFP1 water molecules) at 300 K, with a time step of 1 fs. The simulation was carried out for 60 ps with 50 ps equilibration, and configurations were extracted every 10 steps after equilibration was achieved. Therefore, a total of 1000 configurations were used to compute the TDDFT(PBE0)/cc-pVDZ vertical excitation energies.

The simplest *ab initio* electronic structure implementation for calculating vertical excitation energies is CIS. TDDFT has become a popular method for calculating electronic excitation spectra because it is able to produce accurate vertical absorption energies for some types of molecular systems, at a relatively modest computational cost.[94-97] Of the methods used in this work, CR-EOM-CCSD(T) is expected to provide the most accurate excitation energies and also to be the most computationally expensive.

III. Results and Discussion

The MP2/6-311++G(2d,2p) optimized structures of the $HCONH_2$:n(H_2O) and NMA:n(H_2O) complexes (n=0~3) are shown in Figures 1 and 2, respectively. In general, the water molecules are more likely to form hydrogen bonds to the carbonyl oxygen than to the amide group.

The calculated vertical $n \rightarrow \pi^*$ (ω_1) and $\pi_{nb} \rightarrow \pi^*$ (ω_2) excitation energies of the amides and amide:water complexes are shown in Tables I and II, respectively. The blue

(or red) -shifted energy values are given in parentheses. In general, $n \rightarrow \pi^*$ excitations are blue-shifted and $\pi_{nb} \rightarrow \pi^*$ excitations are red-shifted at all levels of theory. One exception is the TDDFT $\pi_{nb} \rightarrow \pi^*$ transition in $HCONH_2$:$2H_2Oa$. However, the predicted solvent-induced shifts for these species are small at all levels of theory. EOM-CCSD and CR-EOMCCSD(T) give essentially the same vertical excitation energies.

The MD simulated spectra of $HCONH_2$ and NMA are shown in Figures 3a and 3b, respectively. The $\omega_1(n \rightarrow \pi^*)$ spectra are shown in solid bars and $\omega_2(\pi_{nb} \rightarrow \pi^*)$ spectra are shown in open bars. In each spectrum, the green color represents the amide with 100 EFP1 waters and the orange color represents the amide without EFP1 waters. The average excitation energy of the $\omega_1(n \rightarrow \pi^*)$ transition is blue-shifted and the average $\omega_2(\pi_{nb} \rightarrow \pi^*)$ transition is red-shifted in both $HCONH_2$:100EFP1 and NMA:100EFP1, relative to the $HCONH_2$ and NMA without EFP1 waters present.

Each geometric configuration (snapshot) in an MD trajectory shows different electronic properties. Hence, the $\omega_1(n \rightarrow \pi^*)$ and $\omega_2(\pi_{nb} \rightarrow \pi^*)$ vertical excitation energies are different for one geometric configuration to another. Therefore, it is important to average the excitation energies. The computed average vertical excitation energy values and shifts are given in Table III. The computed shifts are in reasonable agreement with the experimental data.[4, 5]

The physical origin of the solvatochromic shifts of $\omega_1(n \to \pi^*)$ and $\omega_2(\pi_{nb} \to \pi^*)$ can be correlated with molecular orbital characteristics if the CIS wavefunction is in reasonable agreement with the more reliable levels of theory (e.g., the EOM-CC methods), and if the CI wavefunction is dominated by just one orbital excitation, such as $n \to \pi^*$ and $\pi_{nb} \to \pi^*$. It may be seen in Tables 1 and 2 that although the absolute CIS excitation energies are too high relative to the more accurate methods, they are consistently so. Consequently, the CIS method is in consistently good agreement with the shifts that are predicted by the EOM-CC methods. In addition, the CIS expansion coefficient for the $n \to \pi^*$ and $\pi_{nb} \to \pi^*$ excitations are greater than $|0.9|$ in most of the complexes and always greater than $|0.8|$, so, a *qualitative* orbital-based argument is reasonable here.

The π_{nb}, n, and π^* Hartee-Fock orbitals of $HCONH_2$ and NMA molcules are shown in Fig. 4(a) and 4(b), respectively. Schematic representations of the molecular orbitals and vertical excitation of amides are provided in Fig. 5. According to Figures 4(a), 4(b) and 5, the electron densities of both the lone pair orbital n and the anti-bonding π^* orbital are distributed mainly on the carbonyl group of the amide. Most of the electron density in the n orbital is located on the oxygen, while in the π^* orbital most of the electron density is located on the carbonyl carbon. The nonbonding orbital π_{nb} has a nodal plane on the carbonyl carbon atom. Therefore, the electronic density of the π_{nb} orbital is primarily on the nitrogen atom and on the oxygen atom.

As illustrated in Figure 6, the schematic energy level diagrams[44] are designed for the solvent effects on the vertical excitations using two possible interactions (Interaction type I and Interaction type II), of water with amides. Figure 7 shows the configuration (snapshot) of $HCONH_2$ in EFP1 water during a MD simulation. This shows how the EFP1 water molecules spherically surround the solute molecule. One can determine the optimum number of EFP1 waters that are required for solvation by successively adding EFP1 water molecules and calculating the properties. The solutes $HCONH_2$ and NMA (not shown) are relatively small, so 100 EFP1 water molecules are sufficient for complete solvation. The structural pattern of water molecules surrounding the solutes shown in Figure 7 is close to that of the solute:$n(H_2O)$ in gas phase shown in Figures 1 and 2.

Interaction type I: In Fig. 6 (a), one of the hydrogen atoms in a water molecule involves a hydrogen bond interaction with the amide carbonyl oxygen. In this interaction type, the water oxygen atom donates the hydrogen to the carbonyl oxygen acting as the hydrogen acceptor. Both the occupied (n and π_{nb}) and virtual (π^*) amide orbitals are stabilized due to the favorable electronic interaction between the partially positive water hydrogen atom and the electronic density on the carbonyl group. However, one can deduce that the amide n orbital would be more stabilized than the π^* orbital since the n orbital has more electron density localized on the carbonyl oxygen than does the π^* orbital. Therefore, the n-π^* energy gap increases in the presence of the water, relative to the isolated amide molecule. This interaction results in a blue-shifted $n \rightarrow \pi^*$ vertical

excitation. However, the amide occupied π_{nb} orbital will be slightly less stabilized than that of the π^* orbital because the π_{nb} electron density is distributed between the nitrogen and oxygen atoms. Therefore, the π_{nb}-π^* energy gap slightly decreases n the presence of a water molecule, relative to the isolated amide molecule, giving rise to a red shift upon solvation.

Interaction type II: In Fig. 6 (b), a water oxygen atom forms a hydrogen bond interaction with an amide (N-H) hydrogen atom. In this interaction type, the water oxygen atom is the hydrogen atom acceptor and the N-H amide group is the hydrogen donor. Since the electron densities on the occupied orbitals (n and π_{nb}) and the virtual π^* orbital cause a destabilizing electronic interaction between the partially negative water oxygen atom and the partially negative amide nitrogen atom, each of the π_{nb}, n, and the π^* orbital energies increase in the presence of a water molecule, relative to an isolated amide. One can deduce that the π_{nb} orbital will be destabilized more than the π^* due to the larger electron density of the π_{nb} localized on the amide nitrogen atom than that of π^* orbital. Therefore, the π_{nb}-π^* energy gap decreases with a water present, relative to the isolated amide molecule. This gives rise to a red-shifted $\pi_{nb} \rightarrow \pi^*$ vertical excitation.

In summary, the blue (or red)-shift vertical excitations are mainly due to the different electron density distributions between the n (or π_{nb}) and the π^* orbitals of amides interact with different solvent configurations via hydrogen bonding.

IV. Conclusions

Four different levels of theory CIS, EOM-CCSD, CR-EOMCCSD(T), and TDDFT (PBE0 functional) with cc-pVDZ basis set are used to study the explicit solvent effect on the electronic spectra for the of $HCONH_2{:}n(H_2O)$ and $NMA{:}n(H_2O)$ complexes (n = 1-3). These computational results provide the *qualitative* interpretation of the solvent effects on the electronic absorption spectra of amides. In addition, the simulated electronic spectra are calculated through the QM/EFP1 MD simulation combined with TDDFT/EFP1. The calculated water solvent effect on the $n{\rightarrow}\pi^*$ and $\pi_{nb}{\rightarrow}\pi^*$ vertical excitations exhibits *quantitative* blue- and red- shifts in the amides, which are consistent with the experimental observation.

The schematic energy level diagrams (Fig. 6) are used to understand the solvent induced blue- and red -shift vertical excitation of the amides. In summary, the physical origin of the solvent effect on $n{\rightarrow}\pi^*$ (blue-shift) and $\pi_{nb}{\rightarrow}\pi^*$ (red-shift) vertical excitations of amides could be understood as how the energies of occupied molecular orbitals are changed relative to that of the π^* due to stabilizing (or destabilizing) electronic interaction of water with the electronic densities of the amides.

Acknowledgements

References

1. Szalay, P.; Fogarasi, G. Theoretical Prediction of the Electronic Excited States and Resonance Raman Intensities in Formamide from Coupled Cluster Calculations. *Chem. Phys. Lett.* **1997,** *270*, 406-412.

2. Hunt, H. D.; Simpson, W. T. Spectra of Simple Amides in the Vacuum Ultraviolet. *J. Am. Chem. Soc.* **1953,** *75*, 4540-4543.

3. Kaya, K.; Nagakura, S. Electronic Absorption Spectra of Hydrogen Bonded Amides. *Theor. Chim. Acta.* **1967,** *7*, 124-132.

4. Nielsen, E. B.; Schellman, J. A. The Absorption Spectra of Simple Amides and Peptides. *J. Phys. Chem.* **1967,** *71*, 2297-2304.

5. Basch, H.; Robin, M. B.; Kuebler, N. A. Electronic Spectra of Isoelectronic Amides, Acids, and Acyl Fluorides. *J. Chem. Phys.* **1968,** *49*, 5007-5018.

6. Gingell, J. M.; Mason, N. J.; Zhao, H.; Walker, I. C.; Siggel, M. R. F. VUV Optical Absorption and Electron Energy Loss Spectroscopy of Formamide. *Chem. Phys.* **1997,** *220*, 191-205.

7. Basch, H.; Robin, M. B.; Kuebler, N. A. Electronic States of the Amide Group. *J. Chem. Phys.* **1967,** *47*, 1201-1210.

8. Nitzsche, L. E.; Davidson, E. R. Ab Initio Calculation of Some Vertical Excitation Energies of N-Methylacetamide. *J. Am. Chem. Soc.* **1978,** *100*, 7201-7204.

9. Li, Y.; Garrell, R. L.; Houk, K. N. Mechanism of Cis-Trans Isomerizations of Amide and Peptide Excited States. *J. Am. Chem. Soc.* **1991,** *113*, 5895-5896.

10. Sobolewski, A. L. Ab Initio Study of Potential Energy Surfaces Relevant for Hydrogen Transfer in Formamide, Its Dimer and Its Complex with Water. *J. Photochem. Photobiol. A* **1995,** *89*, 89-97.

11. Hirst, J. D.; Hirst, D. M.; Brooks, C. L. I. Ab Initio Calculations of the Excited States of Formamide. *J. Phys. Chem.* **1996** *100*, 13487-13491.

12. Hirst, J. D.; Hirst, D. M.; Brooks, C. L. I. Multireference Configuration Interaction Calculations of Electronic States of N-Methylformamide, Acetamide, and N-Methylacetamide. *J. Phys. Chem.* **1997** *101*, 4821-4827.

13. Doltsinis, N. L.; Sprik, M. Electronic Excitation Spectra from Time-Dependent Density Functional Response Theory Using Plane-Wave Methods. *Chem. Phys. Lett.* **2000,** *330*, 563-569.

14. Serrano-Andrés, L.; Fülscher, M. P. Theoretical Study of the Electronic Spectroscopy of Peptides. 1. The Peptidic Bond: Primary, Secondary, and Tertiary Amides. *J. Am. Chem. Soc.* **1996,** *118*, 12190-12199.

15. Glazer, A. N.; Rosenheck, K. Solvent and Conformational Effects on the Ultraviolet Spectra of Polypeptides and Substituted Amides. *J. Biol. Chem.* **1962,** *237*, 3674-3678.

16. Bayliss, N. S.; McRae, E. G. Solvent Effects in Organic Spectra: Dipole Forces and the Franck–Condon Principle. *J. Phys. Chem.* **1954,** *58*, 1002-1006.

17. Bayliss, N. S.; McRae, E. G. Solvent Effects in the Spectra of Acetone, Crotonaldehyde, Nitromethane and Nitrobenzene. *J. Phys. Chem.* **1954,** *58*, 1006-1011.

18. Bayliss, N. S.; Will-Johnson, G. Solvent Effects on the Intensities of the Weak Ultraviolet Spectra of Ketones and Nitroparaffins-I *Spectrochim. Acta. A* **1968,** *24*, 551-561.

19. Onsager, L. Electric Moments of Molecules in Liquids. *J. Am. Chem. Soc.* **1938,** *58*, 1486-1493.

20. Tomasi, J.; Perisco, M. Molecular Interactions in Solution: An Overview of Methods Based on Continuous Distributions of the Solvent. *Chem. Rev.* **1994,** *94*, 2027-2094.

21. Warshel, A. Calculations of Chemical Processes in Solutions. *J. Phys. Chem.* **1979,** *83*, 1640-1652.

22. Levy, R. M.; Kitchen, D. B.; Blair, J. T.; Krogh-Jespersen, K. J. Molecular Dynamics Simulation of Time-Resolved Fluorescence and Nonequilibrium Solvation of Formaldehyde in Water. *J. Phys. Chem.* **1990,** *94*, 4470-4476.

23. Miertus, S.; Scrocco, E.; Tomasi, J. Electrostatic Interaction of a Solute with a Continuum: A Direct Utilization of ab initio Molecular Potentials for the Prevision of Solvent Effects. *Chem. Phys.* **1981,** *55*, 117-129.

24. Klamt, A.; Schuurmann, G. COSMO: A New Approach to Dielectric Screening in Solvents with Explicit Expressions for the Screening Energy and Its Gradient. *J. Chem. Soc., Perkin. Trans. 2* **1993,** 5, 799-805.

25. Klamt, A. Conductor-Like Screening Model for Real Solvents: A New Approach to the Quantitative Calculation of Solvation Phenomena. *J. Phys. Chem.* **1995,** *99*, 2224-2235.

26. Cramer, C. J.; Truhlar, D. G. General Parameterized Scf Model for Free-Energies of Solvation in Aqueous-Solution. *J. Am. Chem. Soc.* **1991,** *113*, 8305-8311.

27. Cramer, C. J.; Truhlar, D. G. Pm3-Sm3: a General Parameterization for Including Aqueous Solvation Effects in the Pm3 Molecular-Orbital Model. *J. Comput. Chem.* **1992,** *13*, 1089-1097.

28. Cramer, C. J.; Truhlar, D. G. An Scf Solvation Model for the Hydrophobic Effect and Absolute Free-Energies of Aqueous Solvation. *Science* **1992,** *256*, 213-217.

29. Zhan, C.-G.; Bentley, J.; Chipman, D. M. Volume Polarization in Reaction Field Theory. *J. Chem. Phys.* **1998,** *108*, 177-192.

30. Kirkwood, J. G. Theory of Solutions of Molecules Containing Widely Separated Charges with Special Application to Zwitterions. *J. Chem. Phys.* **1934,** *2*, 351-361.

31. Tomasi, J.; Mennucci, B.; Cammi, R. Quantum Mechanical Continuum Solvation Models. *Chem. Rev.* **2005,** *105*, 2999-3094.

32. Mennucci, B., Continuum Solvation Models: What Else Can We Learn from Them? *J. Phys. Chem. Lett.* **2010,** *1*, 1666-1674.

33. Berendsen, H. J. C.; Grigera, J. R.; Straatsma, T. P. The Missing Term in Effective Pair Potentials. *J. Phys. Chem.* **1987,** *91*, 6269-6271.

34. Jorgensen, W. L.; Chandrasekhar, J.; Madura, J. D.; Impey, R. W.; Klein, M. L. Comparison of Simple Potential Functions for Simulating Liquid Water. *J. Chem. Phys.* **1983,** *79*, 926-935.

35. Jorgensen, W. L.; Tirado-Rives, J. Potential Energy Functions for Atomic-Level Simulations of Water and Organic and Biomolecular Systems. *Proc. Natl. Acad. Sci.* **2005**, *102*, 6665-6670.

36. Jorgensen, W. L.; Maxwell, D. S.; Tirado-Rives, J. Development and Testing of the OPLS All-Atom Force Field on Conformational Energetics and Properties of Organic Liquids. *J. Am. Chem. Soc.* **1996**, *118*, 11225-11236.

37. Hoogerbrugge, P. J.; Koelman, J. M. V. A. Simulating Microscopic Hydrodynamic Phenomena with Dissipative Particle Dynamics. *Europhys. Lett.* **1992**, *19*, 155-160.

38. Español, P.; Revenga, M. Smoothed Dissipative Particle Dynamics. *Phys. Rev. E* **2003**, *67*, 026705-026716.

39. Malevanets, A.; Kapral, R. Mesoscopic Model for Solvent Dynamics. *J. Chem. Phys.* **1999**, *110*, 8605-8613.

40. Ihle, T.; Kroll, D. M. Stochastic Rotation Dynamics: A Galilean-Invariant Mesoscopic Model for Fluid Flow. *Phys. Rev. E* **2001**, *63*, 020201-020204.

41. Gordon, M. S.; Freitag, A. M.; Bandyopadhyay, P.; Jensen, J. H.; Kairys, V.; Stevens, W. J. The Effective Fragment Potential Method: A QM-Based MM Approach to Modeling Environmental Effects in Chemistry. *J. Phys. Chem. A* **2001**, *105*, 293-307.

42. Day, P. N.; Jensen, J. H.; Gordon, M. S.; Webb, S. P.; Stevens, W. J.; Krauss, M.; Garmer, D.; Basch, H.; Cohen, D. An Effective Fragment Method for Modeling Solvent Effects in Quantum Mechanical Calculations. *J. Chem. Phys.* **1996**, *105*, 1968-1986.

43. Adamovic, I.; Freitag, M. A.; Gordon, M. S. Density Functional Theory Based Effective Fragment Potential Method. *J. Chem. Phys.* **2003**, *118*, 6725-6732.

44. Yoo, S.; Zahariev, F.; Sok, S.; Gordon, M. S. Solvent Effects on Optical Properties of Molecules: A Combined Time-Dependent Density Functional Theory/Effective Fragment Potential Approach. *J. Chem. Phys.* **2008**, *129*, 144112-144119.

45. Arora, P.; Slipchenko, L. V.; Webb, S. P.; DeFusco, A.; Gordon, M. S. Solvent-Induced Frequency Shifts: Configuration Interaction Singles Combined with the Effective Fragment Potential Method. *J. Phys. Chem. A* **2010**, *114*, 6742-6750.

46. Minezawa, N.; De Silva, N.; Zahariev, F.; Gordon, M. S. Implementation of the Analytic Energy Gradient for the Combined Time-Dependent Density Functional

Theory/Effective Fragment Potential Method: Application to Excited-State Molecular Dynamics Simulations. *J. Chem. Phys.* **2011,** *134*, 054111-054122.

47. Webb, S. P.; Gordon, M. S. Solvation of the Menshutkin Reaction: A Rigorous Test of the Effective Fragment Method. *J. Phys. Chem. A* **1999,** *103*, 1265-1273.

48. Merrill, G. N.; Gordon, M. S. Study of Small Water Clusters Using the Effective Fragment Potential Model. *J. Phys. Chem. A* **1998,** *102*, 2650-2657.

49. Day, P. N.; Pachter, R.; Gordon, M. S.; Merrill, G. N. A Study of Water Clusters Using the Effective Fragment Potential and Monte Carlo Simulated Annealing. *J. Chem. Phys.* **2000,** *112*, 2063-2073.

50. Adamovic, I.; Gordon, M. S. Solvent Effects on the S(N)2 Reaction: Application of the Density Functional Theory-Based Effective Fragment Potential Method. *J. Phys. Chem. A* **2005,** *109*, 1629-1636.

51. Bandyopadhyay, P.; Gordon, M. S. A Combined Discrete/Continuum Solvation Model: Application to Glycine. *J. Chem. Phys.* **2000,** *113*, 1104-1109.

52. Bandyopadhyay, P.; Gordon, M. S.; Mennucci, B.; Tomasi, J. An Integrated Effective Fragment-Polarizable Continuum Approach to Solvation: Theory and Application to Glycine. *J. Chem. Phys.* **2002,** *116*, 5023-5032.

53. Kina, D.; Nakayama, A.; Noro, T.; Taketsugu, T.; Gordon, M. S. Ab Initio QM/MM Molecular Dynamics Study on the Excited-State Hydrogen Transfer of 7-Azaindole in Water Solution. *J. Phys. Chem. A* **2008,** *112*, 9675-9683.

54. Sok, S.; Willow, S. Y.; Zahariev, F.; Gordon, M. S. Solvent-Induced Shift of the Lowest Singlet pi -> pi* Charge-Transfer Excited State of p-Nitroaniline in Water: An Application of the TDDFT/EFP1 Method. *J. Phys. Chem. A* **2011,** *115*, 9801-9809.

55. DeFusco, A.; Ivanic, J.; Schmidt, M. W.; Gordon, M. S. Solvent-Induced Shifts in Electronic Spectra of Uracil. *J. Phys. Chem. A* **2011,** *115*, 4574-4582.

56. Senn, H. M.; Thiel, W. QM/MM Methods for Biomolecular Systems. *Angew. Chem., Int. Ed.* **2009,** *48*, 1198-1229.

57. McCreery, J. H.; Christoffersen, R. E.; Hall, G. G. The Development of Quantum Mechanical Solvent Effect Models. Microscopic Electrostatic Contributions. *J. Am. Chem. Soc.* **1976,** *98*, 7198-7202.

58. Duben, A. J.; Miertus, S. The Effect of Solvent on the Internal Rotation of Formamide: An ab Initio Study Using a Polarizable Continuum Model. *Chem. Phys. Lett.* **1982,** *88*, 395-398.

59. Jorgensen, W. L.; Swenson, C. J. Optimized Intermolecular Potential Functions for Amides and Peptides. Hydration of Amides. *J. Am. Chem. Soc.* **1985,** *107*, 1489-1496.

60. Jasien, P. G.; Stevens, W. J. Ab Initio Study of the Hydrogen Bonding Interactions of Formamide with Water and Methanol. *J. Chem. Phys.* **1986,** *84*, 3271-3277.

61. Sim, F.; St-Amant, A.; Papai, I.; Salahub, D. R. Gaussian Density Functional Calculations on Hydrogen-Bonded Systems. *J. Am. Chem. Soc.* **1992,** *114*, 4391-4400.

62. Craw, J. S.; Guest, J. M.; Cooper, M. D.; Burton, N. A.; Hillier, I. H. Effect of Hydration on the Barrier to Internal Rotation in Formamide. Quantum Mechanical Calculations Including Explicit Solvent and Continuum Models. *J. Phys. Chem.* **1996,** *100*, 6304-6309.

63. Contrador, J. C.; Sanchez, M. L.; Aguilar, M. A.; Olivares del Valle, F. J. Solvent Effects on the Potential Energy Surface of the 1:1 Complex of Water and Formamide: Application of the Polarizable Continuum Model to the Study of Nonadditive Effects. *J. Chem. Phys.* **1996,** *104*, 5539-5536.

64. Adamo, C.; Cossi, M.; Barone, V. Catalytic and Bulk Solvent Effects on Proton Transfer. Formamide as a Case Study. *J. Comput. Chem.* **1997,** *18*, 1993-2000.

65. Chen, W.; Gordon, M. S. The Effective Fragment Model for Solvation: Internal Rotation in Formamide. *J. Chem. Phys.* **1996,** *105*, 11081-11090.

66. Besley, N. A.; Hirst, J. D. Ab Initio Study of the Effect of Solvation on the Electronic Spectra of Formamide and N-Methylacetamide. *J. Phys. Chem. A* **1998,** *102*, 10791-10797.

67. Besley, N. A.; Hirst, J. D. Ab Initio Study of the Electronic Spectrum of Formamide with Explicit Solvent. *J. Am. Chem. Soc.* **1999,** *121*, 8559-8566.

68. Jorgensen, W. L.; Gao, J. Cis-Trans Energy Difference for the Peptide Bond in the Gas Phase and in Aqueous Solution. *J. Am. Chem. Soc.* **1988,** *110*, 4212-4216.

69. Mirkin, N.; Krimm, S. Ab Initio Vibrational Analysis of Hydrogen-Bonded *trans*- and *cis*-N-Methylacetamide. *J. Am. Chem. Soc.* **1991,** *113*, 9742-9747.

70. Wong, M. W.; Wiberg, K. B.; Frisch, M. J. Solvent Effects. 3. Tautomeric Equilibria of Formamide and 2-Pyridone in the Gas Phase and Solution: An Ab Initio SCRF Study. *J. Am. Chem. Soc.* **1992,** *114*, 1645-1652.

71. Guo, H.; Karplus, M. Ab Initio Studies of Hydrogen Bonding of N-Methylacetamide: Structure, Cooperativity, and Internal Rotational Barriers. *J. Phys. Chem.* **1992,** *96*, 7273-7287.

72. Guo, H.; Karplus, M. Solvent Influence on the Stability of the Peptide Hydrogen Bond: A Supramolecular Cooperative Effect. *J. Phys. Chem.* **1994,** *98*, 7104-7105.

73. Dixon, D. A.; Dobbs, K. D.; Valentini, J. J. Amide-Water and Amide-Amide Hydrogen Bond Strengths. *J. Phys. Chem.* **1994,** *98*, 13435-13439.

74. Han, W.-G.; Suhai, S. Density Functional Studies on N-Methylacetamide−Water Complexes. *J. Phys. Chem.* **1996,** *100*, 3942-3949.

75. Bene, D. Molecular Orbital Theory of the Hydrogen Bond. XII. Amide Hydrogen Bonding in Formamide–Water and Formamide-Formaldehyde Systems. *J. Chem. Phys.* **1975,** *62*, 1961-1970.

76. Krauss, M.; Webb, S. P. Solvation and the Excited States of Formamide. *J. Chem. Phys.* **1997,** *107*, 5771−5775.

77. Besley, N. A.; Oakley, M. T.; Cowan, A. J.; Hirst, J. D. A Sequential Molecular Mechanics/Quantum Mechanics Study of the Electronic Spectra of Amides. *J. Am. Chem. Soc.* **2004,** *126*, 13502-13511.

78. Olsen, J. M.; Aidas, K. S.; Kongsted, J. Excited States in Solution Through Polarizable Embedding. *J. Chem. Theory Comput.* **2010,** *6*, 3721-3734.

79. Sneskov, K.; Matito, E.; Kongsted, J.; Christiansen, O. Approximate Inclusion of Triple Excitations in Combined Coupled Cluster/Molecular Mechanics: Calculations of Electronic Excitation Energies in Solution for Acrolein, Water, Formamide, and N-Methylacetamide. *J. Chem. Theory Comput.* **2010,** *6*, 839-850.

80. Flick, J. C.; Kosenkov, D.; Hohenstein, E. G.; Sherrill, C. D.; Slipchenko, L. V. Accurate Prediction of Noncovalent Interaction Energies with the Effective Fragment Potential Method: Comparison of Energy Components to Symmetry-Adapted Perturbation Theory for the S22 Test Set. *J. Chem. Theory Comput.* **2012,** *8*, 2835-2843.

81. Gordon, M. S.; Smith, Q. A.; Xu, P.; Slipchenko, L. V. Accurate First Principles Model Potentials for Intermolecular Interactions. *Annu. Rev. Phys. Chem.* **2013,** *64*, 553-578.

82. Becke, A. D. Density-Functional Exchange-Energy Approximation with Correct Asymptotic Behavior. *Phys. Rev. A* **1988,** *38*, 3098-3100.

83. Lee, C.; Yang, W.; Parr, R. G. Development of the Colle-Salvetti Correlation-Energy Formula into a Functional of the Electron Density. *Phys. Rev. B* **1988,** *37*, 785-789.

84. Schmidt, M. W.; Baldridge, K. K.; Boatz, J. A.; Elbert, S. T.; Gordon, M. S.; Jensen, J. H.; Koseki, S.; Matsunaga, N.; Nguyen, K. A.; Su, S. *et al*. General Atomic and Molecular Electronic Structure System. *J. Comput. Chem.* **1993,** *14*, 1347-1363.

85. Gordon, M. S.; Schmidt, M. W. *Advances in Electronic Structure Theory: GAMESS a Decade Later*; Elsevier: Amsterdam, The Netherlands, 2005.

86. Moller, C.; Plesset, M. S. Static Conductance and Scaling Theory of Localization in One Dimension. *Phys. Rev. Lett.* **1934,** *46*, 618-621.

87. Foresman, J. B.; Head-Gordon, M.; Pople, J. A.; Frisch, J. Toward a Systematic Molecular Orbital Theory for Excited States. *J. Phys. Chem.* **1992,** *96*, 135-149.

88. Piecuch, P.; Kucharski, S. Ç. A.; Kowalski, K.; Musiał, M. Efficient Computer Implementation of the Renormalized Coupled-Cluster Methods: The R-CCSD[T], R-CCSD(T), CR-CCSD[T], and CR-CCSD(T) Approaches. *Comput. Phys. Commun.* **2002,** *149*, 71-96.

89. Kowalski, K.; Piecuch, P. New Coupled-Cluster Methods with Singles, Doubles, and Noniterative Triples for High Accuracy Calculations of Excited Electronic States. *J. Chem. Phys.* **2004,** *120*, 1715-1738.

90. Runge, E.; Gross, E. K. U. Density-Functional Theory for Time-Dependent Systems. *Phys. Rev. Lett.* **1984,** *52*, 997-1000.

91. Petersilka, M.; Gossmann, U. J.; Gross, E. K. U. Excitation Energies from Time-Dependent Density-Functional Theory. *Phys. Rev. Lett.* **1996,** *76*, 1212-1215.

92. Dunning Jr., T. H. Gaussian Basis Sets for Use in Correlated Molecular Calculations. I. The Atoms Boron Through Neon and Hydrogen. *J. Chem. Phys.* **1989,** *90*, 1007-1023.

93.   Woon, D. E.; Dunning Jr., T. H. Gaussian Basis Sets for Use in Correlated Molecular Calculations. III. The Atoms Aluminum Through Argon. *J. Chem. Phys.* **1993,** *98*, 1358-1371.

94.   Cossi, M.; Barone, V. Time-Dependent Density Functional Theory for Molecules in Liquid Solutions. *J. Chem. Phys.* **2001,** *115*, 4708-4717.

95.   Improta, R.; Barone, V. Absorption and Fluorescence Spectra of Uracil in the Gas Phase and in Aqueous Solution: A TD-DFT Quantum Mechanical Study. *J. Am. Chem. Soc.* **2004,** *126*, 14320-14321.

96.   Jacquemin, D.; Preat, J.; Charlot, M.; Wathelet, V.; Andre, J. M.; Perpete, E. A. Theoretical Investigation of Substituted Anthraquinone Dyes. *J. Chem. Phys. Lett.* **2004,** *121*, 1736-1743.

97.   Jacquemin, D.; Preat, J. A TD-DFT Study of the Absorption Spectra of Fast Dye Salts. *Chem. Phys. Lett.* **2005,** *410*, 254-259.

Table I. The $\omega_1(n{\to}\pi^*)$ vertical excitation energies (eV) for $HCONH_2$:n(H_2O) and NMA:n(H_2O), n=0~3 with the cc-pVDZ basis set using the MP2/6-311++G(2d,2p) geometry. The vertical excitation energy differences between the amide and amide:water complex are provided in parentheses; a and b refer to different isomers of the complexes (See Figures 1 and 2).

	CIS	EOM-CCSD	CR-	TD-PBE0	Exp
$HCONH_2$	6.48(0.00)	5.78(0.00)	5.41(0.00)	5.65(0.00)	5.58[5]
$HCONH_2$:1H_2Oa	6.84(0.36)	6.04(0.26)	5.65(0.24)	5.89(0.24)	
$HCONH_2$:1H_2Ob	6.57(0.10)	5.84(0.07)	5.47(0.06)	5.71(0.06)	
$HCONH_2$:2H_2Oa	7.12(0.65)	6.26(0.48)	5.85(0.44)	6.06(0.41)	
$HCONH_2$:2H_2Ob	6.97(0.50)	6.13(0.35)	5.73(0.32)	5.96(0.31)	
$HCONH_2$:3H_2Oa	7.25(0.78)	6.35(0.57)	5.94(0.53)	6.13(0.48)	
$HCONH_2$:3H_2Ob	7.22(0.75)	6.33(0.56)	5.92(0.51)	6.12(0.47)	
NMA	6.77(0.00)	5.90(0.00)	5.48(0.00)	5.71(0.00)	[a]5.46[15]
NMA:1H_2Oa	7.08(0.31)	6.14(0.24)	5.70(0.22)	5.94(0.22)	
NMA:1H_2Ob	6.81(0.05)	5.92(0.02)	5.50(0.02)	5.72(0.01)	
NMA:2H_2Oa	7.33(0.56)	6.30(0.40)	5.84(0.36)	6.07(0.36)	
NMA:2H_2Ob	7.14(0.38)	6.18(0.28)	5.73(0.26)	5.96(0.25)	
NMA:3H_2Oa	7.45(0.68)	6.35(0.45)	5.87(0.40)	6.10(0.38)	
NMA:3H_2Ob	7.41(0.64)	6.35(0.46)	5.89(0.41)	6.11(0.40)	

[a]NMA in cyclohexane (The experimental data for NMA are not available for the n-π^* state).

Table II. The $\omega_2(\pi_{nb}\rightarrow\pi^*)$ vertical excitation energies (eV) for $HCONH_2$:n(H_2O) and NMA:n(H_2O), n=0~3 with the cc-pVDZ basis set using the MP2/6-311++G(2d,2p) geometry. The vertical excitation energy differences between the amide and amide:water complex are provided in parentheses; a and b refer to different isomers of the complexes (See Figures 1 and 2).

	CIS	EOM-CCSD	CR-EOMCCSD(T)	TD-PBE0	Exp
$HCONH_2$	9.21(0.00)	8.13(0.00)	7.79(0.00)	8.64(0.00)	7.31[5]
$HCONH_2$:1H_2O	9.08(-0.13)	7.90(-0.23)	7.42(-0.37)	8.61(-0.03)	
$HCONH_2$:1H_2O	9.12(-0.09)	7.96(-0.17)	7.47(-0.32)	8.39(-0.25)	
$HCONH_2$:2H_2O	9.12(-0.08)	7.93(-0.20)	7.46(-0.33)	8.75(0.11)	
$HCONH_2$:2H_2O	9.07(-0.13)	7.88(-0.25)	7.41(-0.38)	8.61(-0.03)	
$HCONH_2$:3H_2O	9.11(-0.09)	7.90(-0.23)	7.44(-0.35)	7.95(-0.69)	
$HCONH_2$:3H_2O	9.07(-0.13)	7.90(-0.23)	7.44(-0.35)	8.10(-0.54)	
NMA	8.94(0.00)	7.68(0.00)	7.17(0.00)	7.57(0.00)	6.81[3]
NMA:1H_2Oa	8.96(0.03)	7.70(0.01)	7.23(0.05)	7.72(0.15)	
NMA:1H_2Ob	8.87(-0.07)	7.64(-0.04)	7.15(-0.02)	7.47(-0.10)	
NMA:2H_2Oa	8.89(-0.04)	7.58(-0.10)	7.08(-0.09)	7.54(-0.03)	
NMA:2H_2Ob	8.88(-0.05)	7.63(-0.05)	7.14(-0.03)	7.56(-0.01)	
NMA:3H_2Oa	8.84(-0.10)	7.50(-0.19)	6.99(-0.18)	7.54(-0.03)	
NMA:3H_2Ob	8.83(-0.11)	7.54(-0.14)	7.05(-0.13)	7.56(-0.01)	

Table III. The average vertical excitation energies of ω_1 and ω_2 are given in eV for HCONH$_2$ and NMA at the TD-PBE0/cc-pVDZ level of theory.

	$\omega_1(n\rightarrow\pi^*)$	$\omega_2(\pi_{nb}\rightarrow\pi^*)$
HCONH$_2$	5.75	8.74
HCONH$_2$:100EFP1	6.08	8.31
QM/EFP1 shift	0.33	$-$ 0.43
Experimental shift	0.27[a]	$-$ 0.50[b]
NMA	5.74	7.52
NMA:100EFP1	6.15	7.51
QM/EFP1 shift	0.42	$-$ 0.01
Experimental shift	0.39[c]	$-$ 0.07[d]

[a]Obtained using the $n\rightarrow\pi^*$ absorption spectra of HCONH$_2$ in gas phase (5.58 eV)[5] and HCONH$_2$ in aqueous solution (5.85 eV).[4]

[b]Obtained using the $\pi_{nb}\rightarrow\pi^*$ absorption spectra of HCONH$_2$ in gas phase (7.31 eV)[5] and HCONH$_2$ in acetonitrile solution (6.81 eV).[5]

[c]Obtained using the $n\rightarrow\pi^*$ absorption spectra of NMA in cyclohexane (5.46 eV)[15] and NMA in aqueous solution (5.85 eV).[4]

[d]Obtained using the $\pi_{nb}\rightarrow\pi^*$ absorption spectra of NMA in cyclohexane (6.74 eV)[4] and NMA in aqueous solution (6.67 eV).[4]

HCONH₂

HCONH₂:1H₂Oa
0.00

HCONH₂:1H₂Ob
4.30
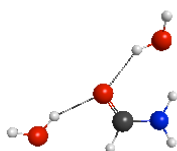
HCONH₂:2H₂Oa
4.46

HCONH₂:2H₂Ob
0.00

HCONH₂:3H₂Oa
0.00
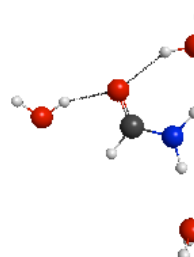
HCONH₂:3H₂Ob
4.94

Figure 1. MP2/6-311++G(2d,2p) optimized structures of HCONH₂:n(H₂O) complexes (n=0~3); a and b refer to different isomers of the complexes. The relative energies of isomers in each HCONH₂:n(H₂O) complexes are given in kcal/mol.
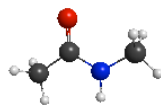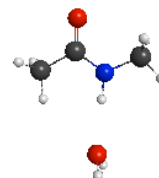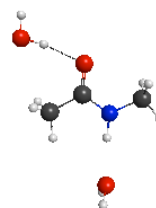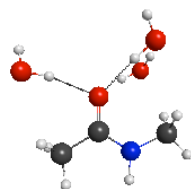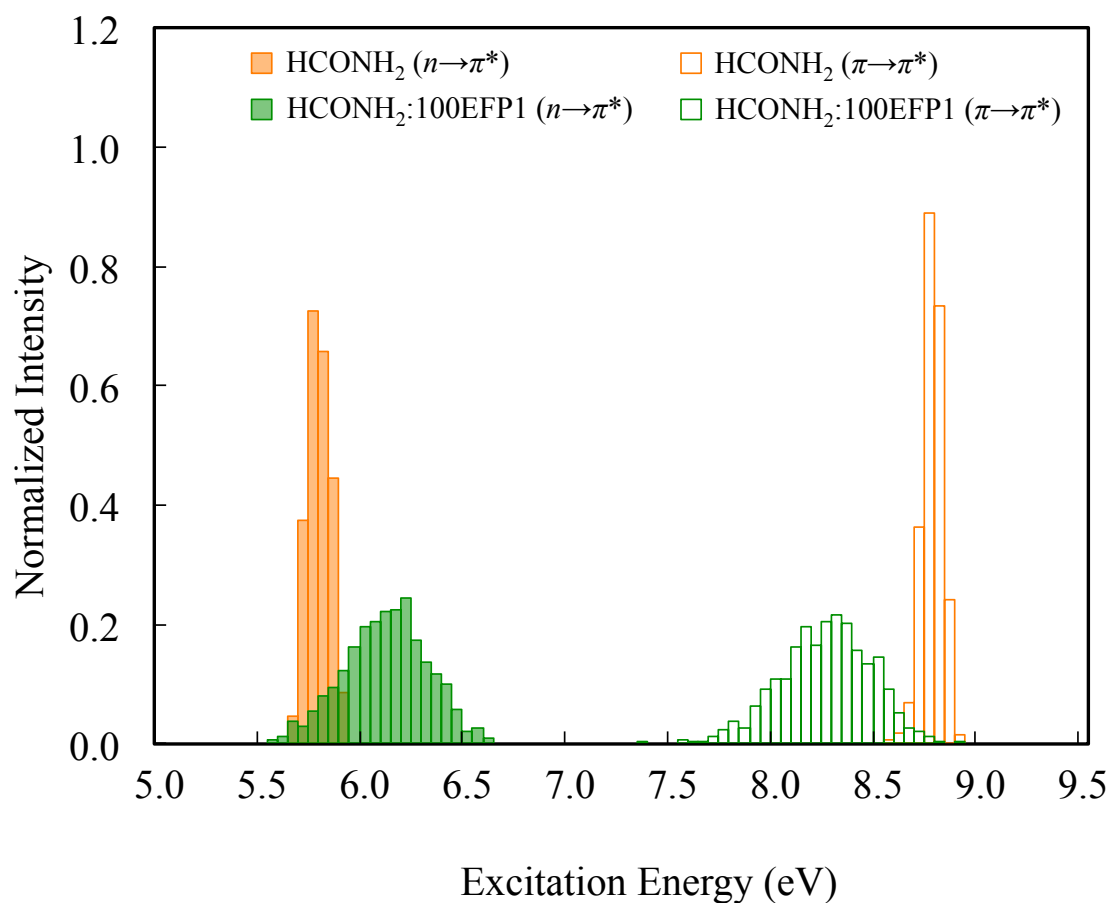
NMA
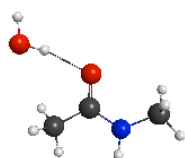
NMA:1H₂Oa
2.58

NMA:1H₂Ob
0.00

NMA:2H₂Oa
0.00

NMA:2H₂Ob
1.26

NMA:3H₂Oa
0.00

NMA:3H₂Ob
0.60

Figure 2. MP2/6-311++G(2d,2p) optimized structures of NMA:n(H₂O) complexes (n=0~3); a and b refer to different isomers of the complexes. The relative energies of isomers in each HCONH₂:n(H₂O) complexes are given in kcal/mol.

(a) HCONH$_2$

Figure 3. The simulated spectrum for the $\omega_1(n \rightarrow \pi^*)$ (shaded bars) and $\omega_2(\pi_{nb} \rightarrow \pi^*)$ (unshaded bars) vertical excitation energies (ω) of (a) HCONH$_2$ and (b) NMA. The green bars represent the amide with 100EFP1 and the orange bars represent the amide without EFP1.
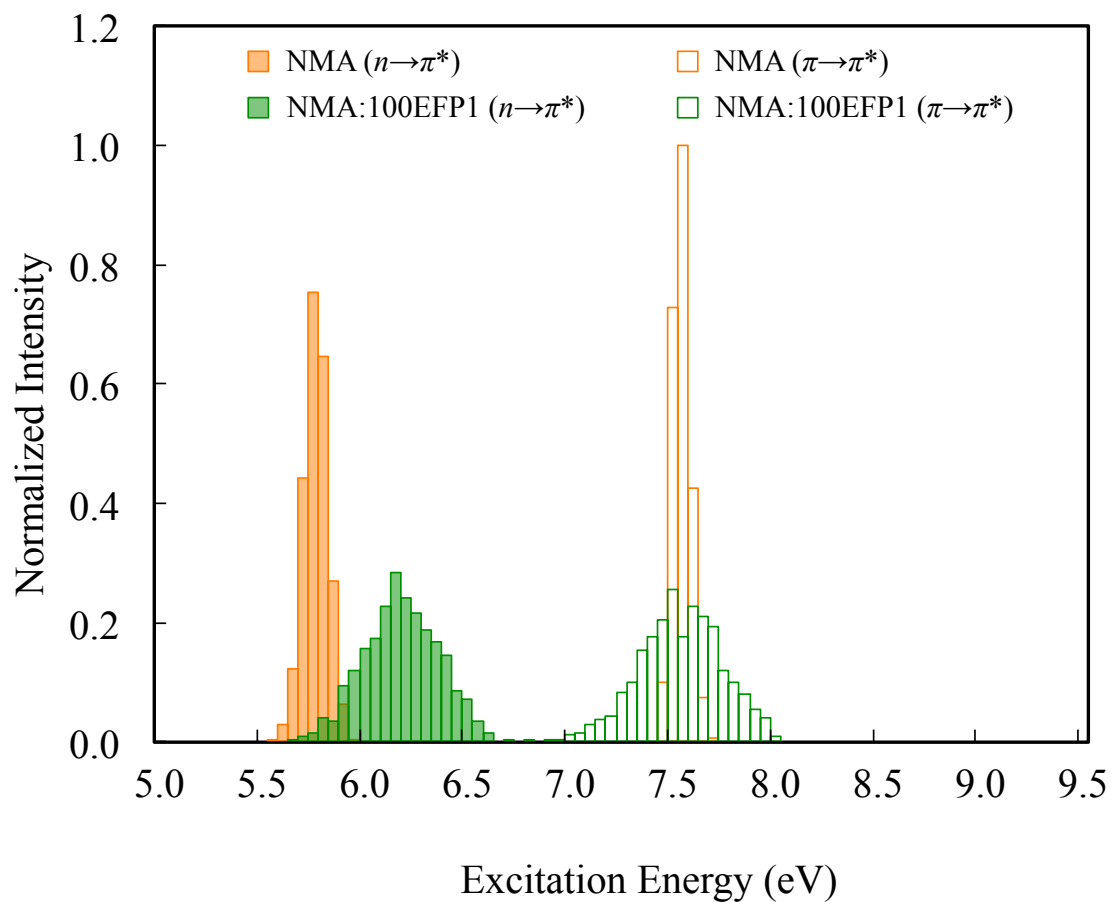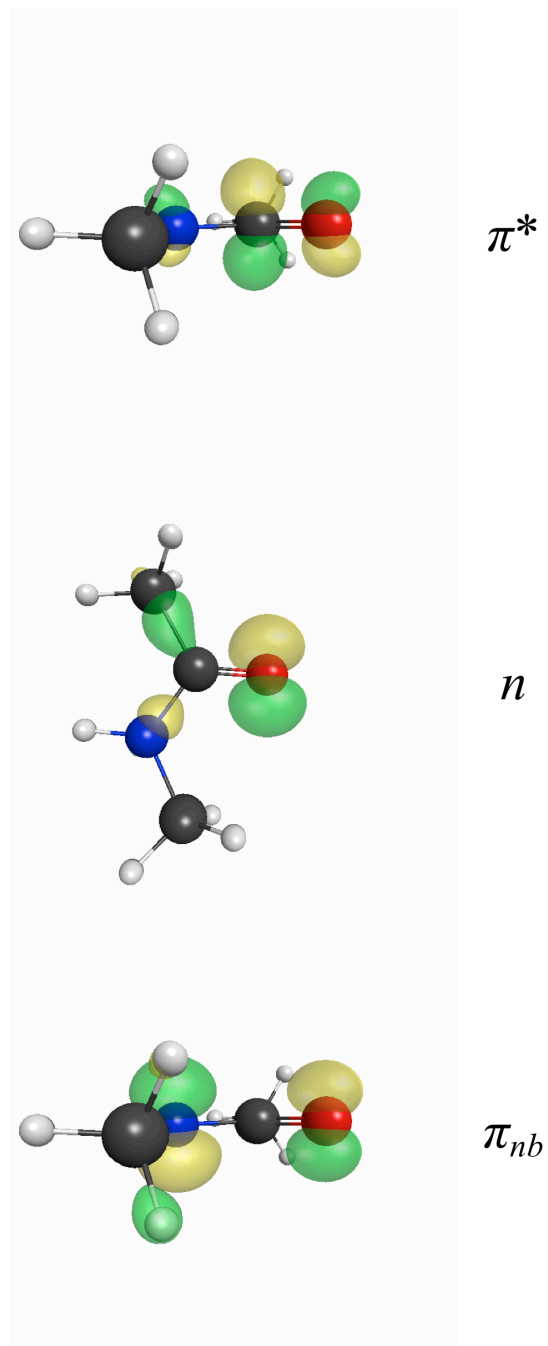
(b) NMA

Figure 3. (continued)

π^*

n

π_{nb}

(a)
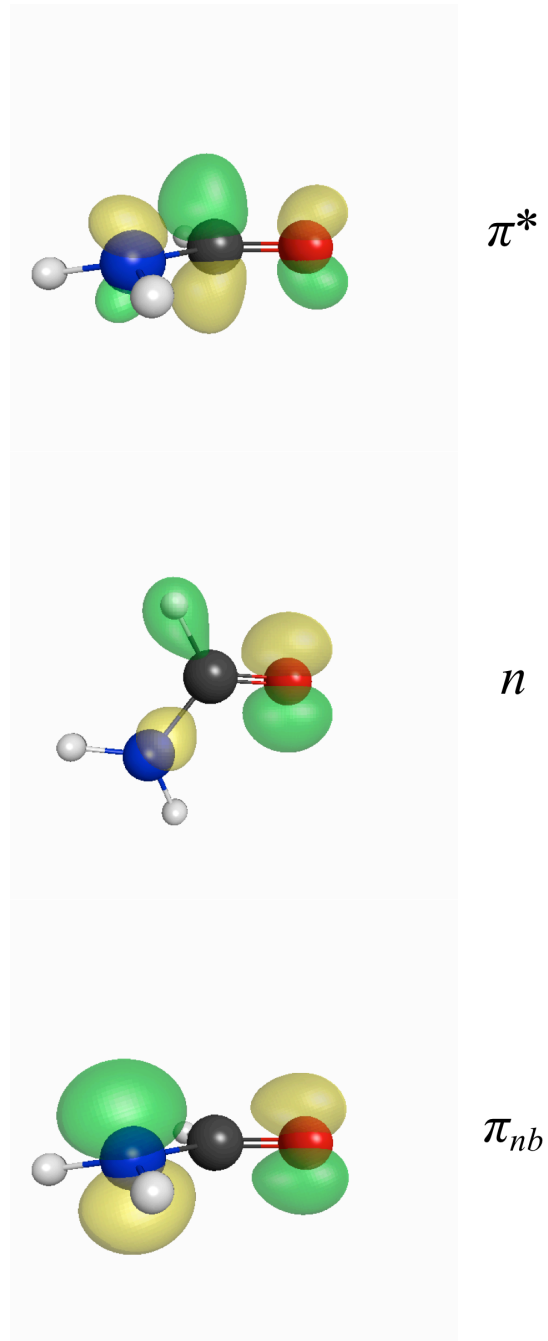
Figure 4. The π_{nb}, n, and π^* Hartree-Fock orbitals of $HCONH_2$ (a) and NMA (b). The color labeling scheme is: C=black, H=gray, N=blue and O=red. The positive lobes of each molecular orbital are yellow and the negative lobes are green.

π^*

n

π_{nb}
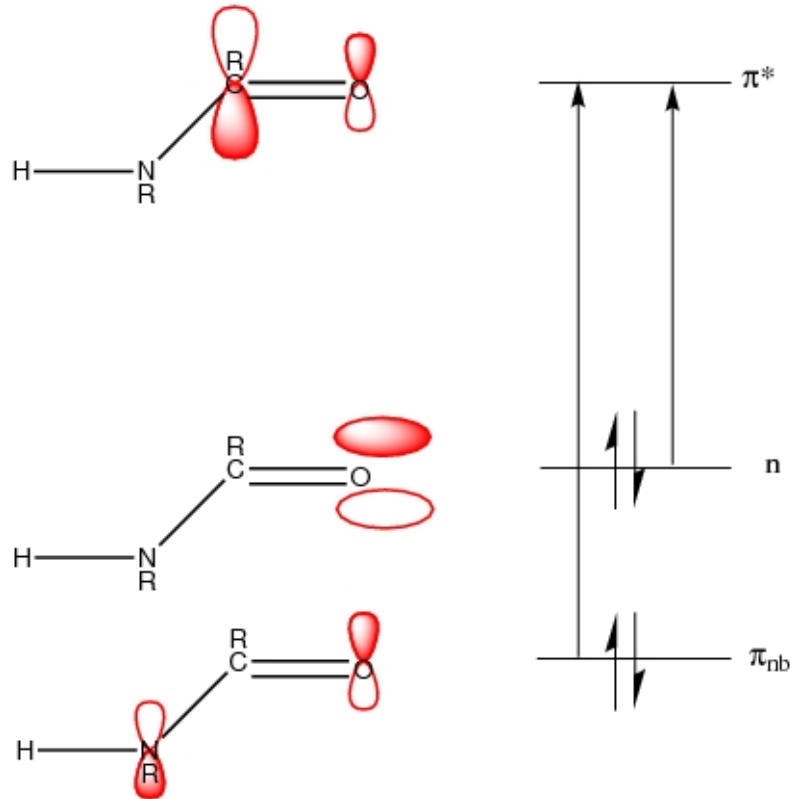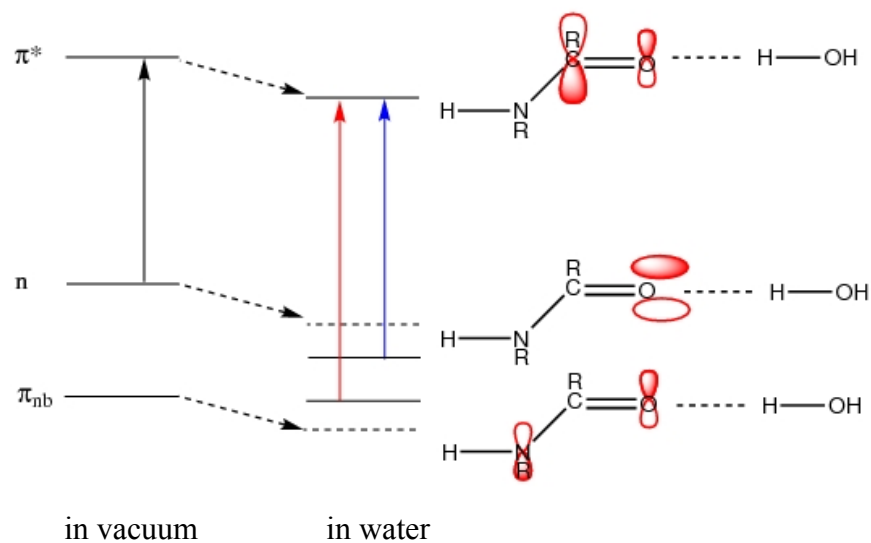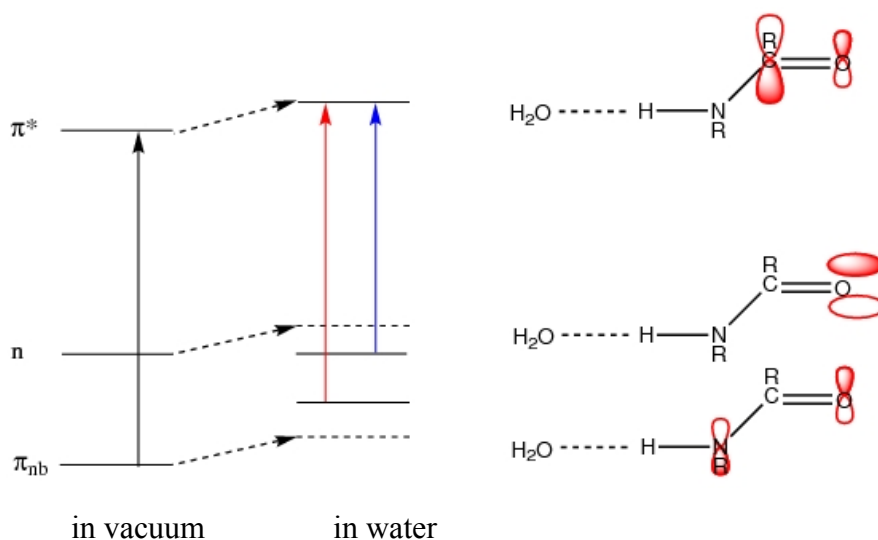
(b)

Figure 4. (continued)

Figure 5. Schematic plots π_{nb}, n, and π^* orbitals, for $HCONH_2$ (R=H) or NMA (R=methyl). Relative vertical excitation energies are indicated with vertical arrows.

(a)

(b)

Figure 6. Schematic energy level diagrams for the vertical excitations in vacuum and solvated systems, indicated with arrows. The dashed lines indicate the situation in which the occupied molecular orbitals (*n* and π_{nb}) have the same electron distribution as the virtual molecular orbital (π^*). The blue and red arrows are used for blue and red -shifts, respectively. Two hydrogen bonding interactions are considered: (a) Interaction type I:

hydrogen bond between water and the carbonyl group and (b) Interaction type II: hydrogen bond between water and the N-H group.
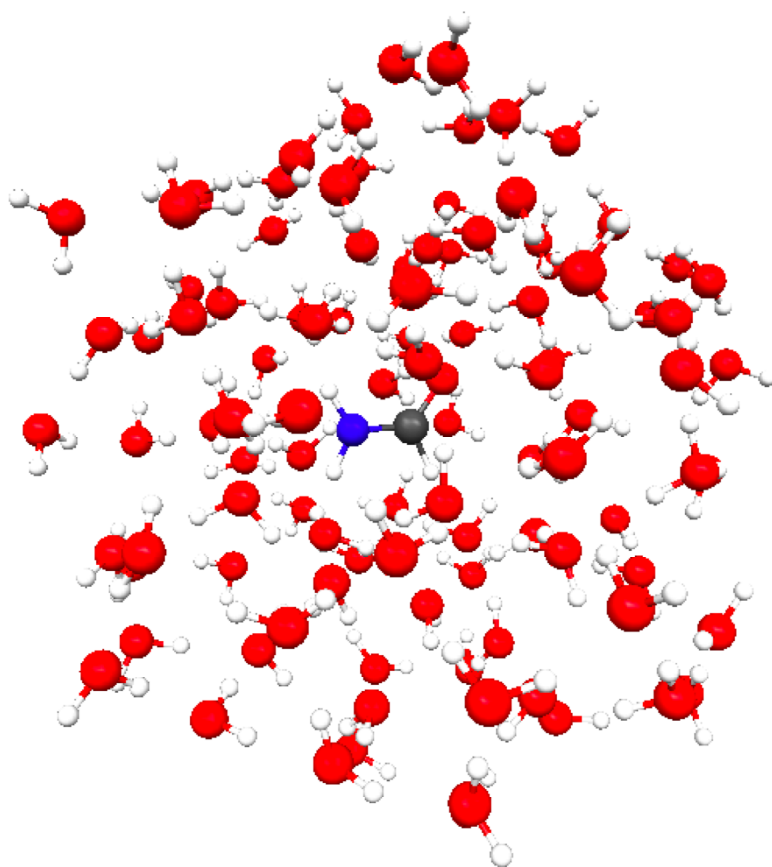

Figure 7. Snapshot of $HCONH_2$ in 100 EFP1 waters during the MD simulation. The hydrogen, carbon, nitrogen and oxygen atoms are colored white, gray, blue and red, respectively.

CHAPTER 5. EXCITED STATE HYDROGEN ATOM TRANSFER REACTION IN SOLVATED 7-HYDROXY-4-METHYLCOUMARIN

Nuwan De Silva, Noriyuki Minezawa, and Mark S. Gordon

Abstract

Excited state enol to keto tautomerization of 7-hydroxy-4-methyl-coumarin (C456) with three water molecules (C456:3H$_2$O), is theoretically investigated using time-dependent density functional theory (TDDFT) combined with the polarizable continuum model and 200 waters explicitly modeled with the effective fragment potential. The tautomerization of C456 in the presence of three water molecules is accompanied by an asynchronous quadruple hydrogen atom transfer reaction from the enol to the keto tautomer in the excited state. TDDFT with the PBE0 functional and the DH(d,p) basis set is used to calculate the excited state reaction barrier height, absorption (excitation) and fluorescence (de-excitation) energies. These results are compared with the available experimental data and theoretical data. In contrast to previous work, it is predicted here that the coumarin 456 system undergoes a hydrogen atom transfer, not a proton transfer. The calculated reaction barrier of the first excited-state of C456:3H$_2$O with 200 water molecules is found to be − 0.23 kcal/mol without zero point energy (− 5.07 kcal/mol with zero point energy i.e. the activation energy).

I. Introduction

The hydrogen atom transfer/proton transfer (HT/PT) reaction is one of the most fundamental reactions occurring in chemistry and biology.[1-6] For example, the excited-state HT/PT relay along the hydrogen-bonded network is a vital reaction in revealing the photoreactivity in green fluorescent protein,[7,8] which is widely used for fluorescence markers in living cells to illuminate a function of a specific gene. The multiple proton relay also plays a critical role in a proton pump across a cell membrane through the proton wire, where the proton transport is achieved against a pH gradient in and out of the membrane. The mechanism of proton transport is also a significant aspect in developing novel polymer electrolyte fuel cells and direct methanol fuel cells, where the multiple proton relay in the water networks may proceed via the Grotthuss mechanism.[9] A full understanding of the mechanisms and dynamics of HT/PT reactions is, therefore, of great importance.

HT/PT reactions can occur either as an intramolecular reaction in which the donor and acceptor groups exist within the same molecule or as an intermolecular reaction in which the donor and acceptor groups are in two different molecules. However, the intramolecular HT/PT reaction cannot spontaneously occur in some molecules because the proton acceptor is not close enough to the proton donor. In such a case, solvent molecules may assist the HT/PT reaction (pseudo-intermolecular reaction) via hydrogen bond formation between the donor and the acceptor and conducting the donor hydrogen

atom or proton to the acceptor. Therefore, in the presence of solvent assistance, the formation of hydrogen bonds along the reaction coordinate can induce a relay of multiple protons or hydrogen atoms from the reactants to the products. However, it is difficult to experimentally determine the characteristic features in a multiple-HT/PT mainly because of thermal fluctuations in the reaction center in the condensed phase.

Often HT/PT reactions are encountered in the excited state. Research on excited state HT and PT (ESHT and ESPT) reactions at the molecular level can be complex due to the structural complexity, very short time scales, and solvent fluctuations involved in the process. Upon electronic excitation, the geometry and acid-base characteristics of a molecule are significantly modulated if ESHT/ESPT occurs. Because the HT/PT process involves motion of the hydrogen atom or proton, the HT/PT transfer process is very sensitive to the degree of hydrogen bonding and also to the dielectric properties of the solvent. Therefore, HT/PT reactions in aqueous solution may involve different reaction pathways and dynamics, depending on the reactants, number of water molecules, and their relative orientations.

Excited-state double HT/PT was discovered by Kasha and co-workers[10] for 7-azaindole (7AI) in alcohol complexes and in a doubly hydrogen-bonded 7AI dimer formed in high concentrations in nonpolar solvents. Since then, the photophysics of bifunctional heteroaromatic compounds has received a great deal of attention. Supersonically jet-cooled hydrogen-bonded clusters in the gas phase are good model

systems to reveal the dynamics of multiple-HT/PT, where the lowering of the temperature significantly suppresses the thermal fluctuations and the cluster size can be controlled.[11] Theoretically, simple model compounds of certain molecules with appropriate protic solvents have been studied to understand the HT/PT process. Kyrychenko, *et al.*[12] have studied the HT/PT reaction of 1H-pyrrolo[3,2-h]quinolone (PQ) with one and two water molecules in the lowest excited singlet states at the TDB3LYP/cc-pVDZ level in the gas phase. They have calculated the excited state PT reaction barrier to be 20.9, 3.0, and 5.6 kcal/mol, respectively, for PQ, PQ:1H_2O, and PQ:2H_2O. Leutwyler and co-workers[13] performed CIS/6-31G(d,p) calculations to investigate the possible competition between HT and PT in 7-hydroxy-quinoline (7HQ) with three NH_3 molecules. They found that barrier for the PT reaction path is 20-25 kcal/mol higher than that for the HT path. Fernandez-Ramos, *et al.*[14] performed complete active space self-consistent field (CASSCF) and multiconfiguration second-order perturbation theory (CASPT2) calculations with the 6-31G(d,p) basis set to investigate the enol to keto tautomerization in the lowest singlet excited state of 7HQ with three NH_3 molecules with *Cs* symmetry in the gas phase. The CASPT2//CASSCF energy barrier for the HT process is ~5 kcal/mol, while the predicted PT pathway has a much larger energy barrier of ~20 kcal/mol.

An early theoretical study on the ESHT reaction of 7AI:1H_2O was performed by Chaban and Gordon,[15,16] in which the CASSCF/DZP method was used for the isolated 7AI molecule and the 7AI:1H_2O complex in the ground and first excited states. 7AI was

predicted to be more stable than the tautomer in the ground state, whereas the relative energies are reversed in the excited state, and the activation energies for tautomerization in both states of 7AI are significantly reduced by the complexation with water.

Most coumarin (1,2-benzopyrone) derivatives have relatively high fluorescence quantum yields.[17-22] Consequently, they are widely used as fluorescent indicators, laser dye colorants, nonlinear optical chromophores, and excellent probes to study the solvation dynamics.[23-29] Among the coumarin dyes, hydroxycoumarin dyes have received the most attention because of their interesting anomalous pH-dependent fluorescence spectra.[30-34] For example depending on the acidity of the solvent 7-hydroxy-4-methyl-coumarin (4-methylumbelliferone), also commercially known as coumarin 456 (C456), exhibits a variety of fluorescence spectra that have been suggested as the basis for the construction of acidity-tunable blue-green lasers.[31,32,34] Henceforth, coumarin 456 will be referred to as C456. C456 is a fluorescent indicator that is colorless at pH 7.0 and exhibits a blue fluorescence at pH 7.5.

Electronic excitation to the S_1 state strongly modifies the acid-base properties of C456, rendering the hydroxyl group more acidic (S_0 (pKa=7.26), S_1 (pKa~0.45)).[35] C456 is a fluorescence indicator and a laser dye whose emission range is exceptionally broad (360-590 nm). In the excited state, C456 exhibits four possible fluorescent species, depending on the solvent and the pH: enol (E*, 380 nm), anionic (A*, 450 nm), cationic (C*, 412 nm), and keto-tautomeric (K*, 480 nm). In the ground state, on the other hand,

the absorption spectra indicate only three species, enol (E), anion (A), and cation (C).[36-38] Therefore, the K* form appears to be an excited-state reaction product, which arises from the E* form through HT/PT from the donor (acidic O−H) to the acceptor (basic C=O) group in the excited state. Direct intramolecular HT/PT in C456 would be difficult because the donor and acceptor components are too far away from each other. Therefore, C456 requires a solvent wire to bridge the donor and acceptor groups. Two different mechanisms of photo-excited tautomerization processes have been discussed in the literature,[33,36,37,39] a dissociative two-step pathway[33,39] via the A* or C* species (reaction intermediates) and a nondissociative[36,37] one-step reaction in water. The latter is considered to be the most probable mechanism.

C456 has been investigated theoretically[40] using the TDB3LYP method and the resolution-of-the-identity coupled-cluster singles-and-doubles (RI-CC2) method with the SVP, SVPD, TZVP, and TZVPD basis sets. The excitation and de-excitation energies of the lowest singlet states for the enol and keto forms were studied in the gas phase and in solution using the polarizable continuum model (PCM)[41,42] for water. The calculations revealed that in PCM water the π-π* state is the lowest lying excited state. Georgieva, *et al*. extended the investigation by studying the PT reaction in C456 along a H-bonded water wire of three water molecules using TDDFT, RI-CC2, and singly excited configuration interaction (CIS) calculations.[43] The calculations suggest the possibility of HT/PT from the enol to the keto form in the excited state. All of the methods used predict that the reaction path occurs in the π-π* state, and no crossing with a Rydberg-type $\pi\sigma$*

state was found. The calculations predict that the S_1 enol- and keto-clusters are separated by a barrier height of 17-20 kcal/mol, although an actual transition state structure was not determined.

In this paper, the excited-state quadruple HT/PT reaction of C456 with three quantum water molecules (C456:3H$_2$O) has been studied. Solvent effects are analyzed by incorporating both the PCM model and the effective fragment potential (EFP) for water.[44-46]

II. Computational Details

The geometries of the enol and keto tautomers of C456 in the ground state (E and K) and the π-π* first excited state (E* and K*) were optimized using PBE0 and TDPBE0,[47-49] respectively, with the DH(d,p)[46] basis set, with no symmetry constrains (C_1 symmetry). The enol tautomer, transition state, and keto tautomer of C456:3H$_2$O as well as C456:3H$_2$O with small clusters of EFP water molecules (C456:3H$_2$O+nEFP n=1−4) in the ground state (E, TS, and K) and the π-π* first excited state (E*, TS*, and K*) were also optimized using the same levels of theory. The geometry optimizations converged the gradient to less than 0.0001 Hartree/Bohr. The Hessian (matrix of energy second derivatives) was calculated and diagonalized at the optimized geometries. All E, K, E*, and K* stationary points of C456, C456:3H$_2$O, and C456:3H$_2$O+nEFP were characterized as true minima by confirming that the all corresponding eigenvalues of the

Hessian are positive. The TS and TS* stationary points were characterized as true saddle points by confirming that there is just one negative Hessian eigenvalue.

The reaction paths in the ground state (S_0) and the first π-π* excited state (S_1) for C456:3H$_2$O and C456:3H$_2$O+nEFP were determined by calculating the intrinsic reaction coordinates (IRC),[50-55] starting from the corresponding transition states. The IRC is the steepest descent path in mass-weighted coordinates and is calculated by propagating the system from the transition state backward and forward towards the reactants (enol tautomer) and products (keto tautomer), respectively.

An additional interpretive tool is provided by the electrostatic potential (ESP)-derived[56,57] TDPBE0/DH(d,p) atomic charges along the excited state IRC path (30 equally spaced points) to determine whether the S_1 reaction is primarily HT or PT in the C456:3H$_2$O system.

The C456 and C456:3H$_2$O systems in the presence of PCM water are denoted C456:PCM and C456:3H$_2$O+PCM, respectively, throughout the remainder of the paper. The stationary points of C456:PCM (E, E*, K, and K*) and C456:3H$_2$O+PCM (E, E*, TS, TS*, K, and K*) were fully optimized and characterized in both S_0 and S_1. The S_0 and S_1 IRC paths of C456:3H$_2$O+PCM were also generated.

The Monte Carlo (MC)[58,59] with simulated annealing (SA)[60] method was used to sample the potential energy surface of C456:3H$_2$O with 200 EFP water molecules (C456:3H$_2$O+200EFP) in S_0 the and the S_1 using PBE0/DH(d,p) and TD-PBE0/DH(d,p), respectively. The gas phase optimized geometries of C456:3H$_2$O and C456:3H$_2$O+nEFP were used as the starting geometries of the MC/SA simulations with 200 EFP water molecules. The MC/SA method with local minimization was used to sample the configuration space. For each global minimum found, the number of structures sampled was on the order of 100000 – 350000. The number of steps taken for each temperature varied from 10 to 1000. The number of steps between local optimizations varied from 10 to 100. The number of fragments moved per step varied from 1 to 20. The starting temperature for the simulated annealing varied from 20000 K to 1000 K and the final temperature varied from 100 K to 300 K.

To obtain the tautomerization activation energy, zero point energy (ZPE) corrections have been obtained using the harmonic frequencies. The S_0 tautomerization barrier height, without ZPE corrections, is $E_{b(E\rightarrow K)} = E_{TS}(S_0) - E_E(S_0)$ where the subscript E refers to the enol tautomer. The barrier height with ZPE corrections yields the 0K activation energy, $E_{a(E\rightarrow K)}$. The barrier height and activation energy in the S_1 excited state are obtained in an analogous manner. These two quantities are denoted as $E_{b(E^*\rightarrow K^*)}$ and $E_{a(E^*\rightarrow K^*)}$, respectively.

Using the optimized geometries, vertical and adiabatic excitation energies (absorption) and vertical de-excitation energies (fluorescence) were carried with TDPBE0/DH(d,p). Only singlet-to-singlet transitions are considered here. The vertical excitation energy corresponds to the electronic excitation from the ground state minimum (S_0) to the first electronic excited S_1 state ($\pi\pi^*$), with no geometry relaxation. The adiabatic excitation energy is the energy difference between the minimum on the S_1 surface and the minimum on the S_0 surface. The vertical de-excitation energy corresponds to the energy difference between the S_0 and S_1 states at the S_1 minimum energy geometry. The ZPE energy corrections to the adiabatic excitation energies were obtained using the zero point energies of the corresponding minima.

All calculations were performed with the general atomic and molecular electronic structure system (GAMESS).[61,62] The structures were visualized with MacMolPlot,[63] a graphical interface to GAMESS.

III. Results and Discussion

The atom labeling of the C456 and C456:3H$_2$O are illustrated in Figure 1. The C456 optimized geometries of the stationary points of S_0 (E and K) and S_1 (E* and K*), respectively, optimized with PBE0/DH(d,p) and TDPBE0/DH(d,p), respectively, are shown in Figure 2. Except for the position of the enol (O20−H21) and keto (C2−H11) functional groups, the main structural difference between the two tautomers is the ring

non planarity of the S_1 state: the E* tautomer is non planar (O1 oxygen atom located out of the fused ring plane) relative to the E, K, and K* tautomers. The zero point energy (ZPE) corrected relative 0K enthalpies (H_{rel}^0) and relative energies without the ZPE correction (E_{rel}) of the C456 tautomers are given in Table I. According to Table 1, H_{rel}^0 of the enol tautomer of C456 is more stable than that of keto in S_0 by 1.09 eV (25.14 kcal/mol). In contrast H_{rel}^0 of the keto tautomer of C456 is more stable in the excited state by 0.23 eV (5.30 kcal/mol). Therefore, the enol to keto tautomerization of C456 is highly endothermic in S_0 and exothermic in S_1. The favorable thermodynamics in S_1 is one of the reasons that the enol to keto tautomerization reaction occurs most likely in the S_1 state. The relative stability of enol in S_0 and keto in S_1 holds for the other C456 complexes in Table 1. The keto-enol energy difference in S_1 is generally rather small, ranging from 0.23 eV when no water is present to 0.03 and 0.05 eV for C456:PCM and C456:3H$_2$O+PCM, respectively. The most important factor for a probable S_1 tautomerization is the lower activation energy compared to the S_0 activation energy (Table II). The location of a transition state was unsuccessful for the isolated C456 system due to the long distance between H21 and O11 (~ 7 Å) in the enol structure and similarly in the keto structure (see Figure 1).

In order to locate the C456 transition state, three quantum water molecules were spatially arranged to bridge the two functional groups via hydrogen bonding. Then, fully optimized transition states were obtained in both the S_0 and S_1 states. C456 requires a minimum of three water molecules (C456:3H$_2$O) to find the enol to keto tautomerization

transition state. The transition state searches for C456 with one, two, and four water molecules were not successful. One and two waters are not sufficient to bridge the two functional groups within C456, while four waters makes the bridge too crowded. The C456:3H$_2$O optimized geometries of the S_0 (E, TS, and K) and S_1 (E*, TS*, and K*) stationary points, optimized, respectively, with PBE0/DH(d,p) and TDPBE0/DH(d,p), are given in Figure 3. In general, the S_1 state C456:3H$_2$O stationary points are somewhat more non planar than those of the S_0 state. The TS and TS* imaginary frequencies are 629i and 601i cm^{-1}, respectively. The IRC paths for the S_0 and S_1 states are shown in Figure 4. Each IRC path confirms that the corresponding transition states do connect the reactants and products as expected. When going from the reactant to the products, four bonds (including three hydrogen bonds) are broken, and four bonds are formed, asynchronously along the reaction coordinates.

The ESP-derived charges are shown in Figure 5 according to the atom labeling in Figure 1. The ESP-derived charges in the excited state enable one to assess whether proton transfer or hydrogen atom transfer occurs during the E* to K* tautomerization. According to Figure 5, the ESP-derived atomic charges on the atoms O20, H21, O22, H23, O24, H25, O26, H27, and O11 do not change significantly on the C456:3H$_2$O S_1 IRC path. However, the charges on atoms O22, O24, and O26 increase from ~ −1.0e to ~ −0.9e in just before the transition state, and then decrease again just after the TS. Moreover, the overall charge on H21 decreases, and the overall charge on H27 increases by ~0.1e before (enol) and after the reaction (keto). It is interesting to note the charge of

the intermediate H23 and H25 transferring atoms in the transition state. The charges on these atoms hardly change throughout the reaction path, remaining at ~0.55e. This is very close to the partial charge on an H atom in a water molecule, as compared to a proton charge of +1. So, the enol-keto excited state process corresponds to a hydrogen atom transfer, not a proton transfer. This is in good agreement with the CIS/SVPD population analysis done by Georgieva et al.[43] on C456:3H$_2$O, where for the S_1 ($\pi\pi^*$) state charges of 0.61e for H23 and H25 has been found. The CIS/6-31(+)G(d,p) population analysis done by Tanner et al.[11,13,64] on 7HQ(NH$_3$)$_3$, predicted for the S_1 ($\pi\pi^*$) state a charge of 0.70e for the NH$_4$ moiety. Therefore, the S_1 state enol to keto tautomerization reaction of C456:3H$_2$O can be interpreted as asynchronized quadruple hydrogen atom transfer reaction, even though the transferring H atoms carry substantial partial charges.

The activation energies for the hydrogen atom transfer from the E to the K tautomeric form in C456:3H$_2$O, C456:3H$_2$O+PCM, and C456:3H$_2$O+200EFP complexes are given in Table II. Table II indicates that the S_0 tautomerization of C456:3H$_2$O in the gas phase is characterized by a high activation energy (0.87 eV) whereas the S_1 state reaction proceeds with a low activation energy (0.23 eV). The inclusion of a small cluster of water molecules decreases the tautomerization activation energy in the S_1 state (Table III). Moreover, hydrogen atom transfer in the excited state C456:3H$_2$O+200EFP is predicted to proceed through a significantly lower activation energy (-0.22 eV with ZPE correction) in the S_1 state. A negative activation energy indicates a barrierless process. The S_0 state activation energy in C456:3H$_2$O+200EFP also decreases two-fold compared

to that of the C456:3H$_2$O. The effect of adding PCM on the C456:3H$_2$O S_0 and S_1 activation energies is small.

The excited state hydrogen atom transfer activation energies of C456:3H$_2$O+nEFP (n=1−4) are given in Table III. In the C456:3H$_2$O+nEFP complexes, the energy barrier is dramatically reduced compared to C456:3H$_2$O, so that upon excitation of the C456:3H$_2$O+nEFP complex, the tautomerization can occur rapidly. Therefore, the hydrogen bond interaction between the EFP molecules and the bridging quantum water molecules further decreases the activation energy. For the C456:3H$_2$O+4EFP system, following the IRC along the that is referenced in Table III, leads to structures that correspond closely to the expected reactants and products (based on direct geometry optimizations), with energy differences that are less than 2 kcal/mol in each case. Therefore, it is likely that the transition structure for the C456:3H$_2$O+4EFP that is described in Table III is a good approximation to the true TS.

The TDPBE0/DH(d,p) absorption, adiabatic, and fluorescence energies for the enol and keto tautomers of the molecular complexes are given in Tables IV and V, respectively. In C456, both absorption and fluorescence energies are higher in the enol tautomer than the corresponding keto tautomer by 1.26 and 1.31 eV, respectively, in the gas phase. In C456:3H$_2$O, both absorption and fluorescence energies are higher in enol tautomer than the corresponding keto tautomer by 0.84 and 0.53 eV, respectively, in the gas phase. In general, the $\pi \rightarrow \pi^*$ vertical excitation, adiabatic, and vertical deexcitation

energies of C456 with water molecules (C456:3H$_2$O and C456:3H$_2$O+200EFP) are red-shifted in the enol tautomer and blue-shifted in the keto tautomer, relative to isolated C456. The global minimum structure of the excited state enol tautomer of C456:3H$_2$O+200EFP is given in Figure 6.

IV. Conclusions

The theoretical study of the ground state and excited state tautomerization reactions in C456 have been presented, using PBE0/DH(d,p) and TDPBE0/DH(d,p), respectively. The transition states of the hydrogen atom transfer reaction were found in C456:3H$_2$O and C456:3H$_2$O with PCM as well as in C456:3H$_2$O with small clusters of EFP waters. The optimized geometries of the corresponding tautomers are also presented. The TDPBE0/DH(d,p) ESP-derived charges along the excited state IRC path predicts that the tautomerization reaction is a hydrogen atom transfer reaction, with hydrogen partial charges of ~0.55 e. The predicted activation energies are in excellent agreement with the experimental evidence. The addition of water molecules to C456 assists the hydrogen atom transfer reaction by decreasing the activation energy in the excited state.

The results in the present work have also been compared with the previous theoretical data reported by Georgieva, *et al*. on the C456:3H$_2$O system. They have considered the S_1 enol to keto tautomerization as a proton transfer reaction; the barrier height was estimated to be 17-20 kcal/mol at the TDB3LYP/SVPD level of theory. In the

present paper, the S_1 enol to keto tautomerization of C456:3H$_2$O was interpreted as a hydrogen atom transfer reaction (not a proton transfer reaction) and the TDPBE0/DH(d,p) barrier height was calculated to be 10.15 kcal/mol (5.30 kcal/mol activation energy).

Acknowledgements

References

1. Douhal, A.; Kim, S. K.; Zewail, A. H. Femtosecond Molecular Dynamics of Tautomerization in Model Base Pairs. *Nature* **1995,** *378*, 260-263.

2. Lu, D. S.; Voth, G. A. Proton Transfer in the Enzyme Carbonic Anhydrase: An Ab Initio Study. *J. Am. Chem. Soc.* **1998,** *120*, 4006-4014.

3. Marx, D.; Tuckerman, M. E.; Hutter, J.; Parrinello, M. The Nature of the Hydrated Excess Proton in Water. *Nature* **1999,** *397*, 601-604.

4. Agarwal, P. K.; Webb, S. P.; Hammes-Schiffer, S. Computational Studies of the Mechanism for Proton and Hydride Transfer in Liver Alcohol Dehydrogenase. *J. Am. Chem. Soc.* **2000,** *122*, 4803-4812.

5. Geissler, P. L.; Dellago, C.; Chandler, D.; Hutter, J.; Parrinello, M. Autoionization in Liquid Water. *Science* **2001,** *291*, 2121-2124.

6. Rini, M.; Magnes, B. Z.; Pines, E.; Nibbering, E. T. J. Real-Time Observation of Bimodal Proton Transfer in Acid-Base Pairs in Water. *Science* **2003,** *301*, 349-352.

7. Zimmer, M. Green Fluorescent Protein (GFP): Applications, Structure, and Related Photophysical Behavior. *Chem. Rev.* **2002,** *102*, 759-781.

8. Stoner-Ma, D.; Jaye, A. A.; Matousek, P.; Towrie, M.; Meech, S. R.; Tonge, P. J. Observation of Excited-State Proton Transfer in Green Fluorescent Protein Using Ultrafast Vibrational Spectroscopy. *J. Am. Chem. Soc.* **2005,** *127*, 2864-2865.

9. Eikerling, M.; Kornyshev, A. A.; Kucernak, A. R. Water in Polymer Electrolyte Fuel Cells: Friend or Foe? *Phys. Today* **2006,** *59*, 38-44.

10. Taylor, C. A.; El-bayoum, M. A.; Kasha, M. Excited-State 2-Proton Tautomerism in Hydrogen-Bonded N-Heterococlic Base Pairs. *Proc. Natl. Acad. Sci. U.S.A.* **1969,** *63*, 253-260.

11. Manca, C.; Tanner, C.; Leutwyler, S. Excited State Hydrogen Atom Transfer in Ammonia-Wire and Water-Wire Clusters. *Int. Rev. Phys. Chem.* **2005,** *24*, 457-488.

12. Kyrychenko, A.; Waluk, J. Excited-State Proton Transfer Through Water Bridges and Structure of Hydrogen-Bonded Complexes in 1H-Pyrrolo 3,2-h Quinoline: Adiabatic Time-Dependent Density Functional Theory Study. *J. Phys. Chem. A* **2006,** *110*, 11958-11967.

13. Tanner, C.; Manca, C.; Leutwyler, S. Probing the Threshold to H Atom Transfer Along a Hydrogen-Bonded Ammonia Wire. *Science* **2003,** *302*, 1736-1739.

14. Fernandez-Ramos, A.; Martinez-Nunez, E.; Vazquez, S. A.; Rios, M. A.; Estevez, C. M.; Merchan, M.; Serrano-Andres, L. Hydrogen Transfer vs Proton Transfer in 7-Hydroxy-Quinoline (NH3)3: A CASSCF/CASPT2 Study. *J. Phys. Chem. A* **2007,** *111*, 5907-5912.

15. Gordon, M. S. Hydrogen Transfer in 7-Azaindole. *J. Phys. Chem.* **1996,** *100*, 3974-3979.

16. Chaban, G. M.; Gordon, M. S. The Ground and Excited State Hydrogen Transfer Potential Energy Surface in 7-Azaindole. *J. Phys. Chem. A* **1998,** *103*, 185-189.

17. Atkins, R. L.; Bliss, D. E. Substituted Coumarins and Azacoumarins - Synthesis and Fluorescent Properties. *J. Org. Chem.* **1978,** *43*, 1975-1980.

18. Schimitschek, E. J.; Trias, J. A.; Hammond, P. R.; Henry, R. A.; Atkins, R. L. New Laser Dyes with Blue-Green Emission. *Opt. Commun.* **1976,** *16*, 313-316.

19. Reynolds, G. A.; Drexhage, K. H. New Coumarin Dyes with Rigidized Structure for Flashlamp-Pumped Dye Lasers. *Opt. Commun.* **1975,** *13*, 222-225.

20. Rechthaler, K.; Kohler, G. Excited-State Properties and Deactivation Pathways of 7-Aminocoumarins. *Chem. Phys.* **1994,** *189*, 99-116.

21. Jones, G.; Jackson, W. R.; Choi, C.; Bergmark, W. R. Solvent Effects on Emission Yield and Lifetime for Coumarin Laser-Dyes - Requirements for a Rotatory Decay Mechanism. *J. Phys. Chem.* **1985,** *89*, 294-300.

22. Jones, G.; Jackson, W. R.; Kanoktanaporn, S.; Halpern, A. M. Solvent Effects on Photophysical Parameters for Coumarin Laser-Dyes. *Opt. Commun.* **1980,** *33*, 315-320.

23. Drexhage, K. H. *Dye-Lasers*. Springer-Verlag: New York, 1990.

24. McCarthy, P. K.; Blanchard, G. J. AM1 Study of the Electronic-Structure of Coumarins. *J. Phys. Chem.* **1993,** *97*, 12205-12209.

25. Jones, G.; Jimenez, J. A. C. Azole-Linked Coumarin Dyes as Fluorescence Probes of Domain-Forming Polymers. *J. Photochem. Photobiol. B* **2001,** *65*, 5-12.

26. Moriya, T. Excited-State Reactions of Coumarins in Aqueous Solutions. III. The Fluorescence Quenching of 7-Ethoxycoumarins by the Chloride Ion in Acidic Solutions. *Bull. Chem. Soc. Jpn.* **1986,** *59*, 961-968.

27. Kaholek, M.; Hrdlovič, P. Spectral Properties of Coumarin Derivatives Substituted at Position 3. Effect of Polymer Matrix. *J. Photochem. Photobiol. A* **1997,** *108*, 283-288.

28. Raju, B. B.; Costa, S. M. B. Excited-State Behavior of 7-Diethylaminocoumarin Dyes in AOT Reversed Micelles: Size Effects. *J. Phys. Chem. B* **1999,** *103*, 4309-4317.

29. Moylan, C. R. Molecular Hyperpolarizabilities of Coumarin Dyes. *J. Phys. Chem.* **1994,** *98*, 13513-13516.

30. Fink, D. W.; Koehler, W. R. pH Effects on Fluorescence of Umbelliferone. *Anal. Chem.* **1970,** *42*, 990-993.

31. Shank, C. V.; Dienes, A.; Trozzolo, A. M.; Myer, J. A. Near UV to Yellow Tunable Laser Emission from an Organic Dye. *Appl. Phys. Lett.* **1970,** *16*, 405-407.

32. Dienes, A.; Shank, C. V.; Trozzolo, A. M. Evidence for Exciplex Laser Action in Coumarin Dyes by Measurements of Stimulated Fluorescence. *Appl. Phys. Lett.* **1970,** *17*, 189-191.

33. Schulman, S. G.; Rosenberg, L. S. Tautomerization Kinetics of 7-Hydroxy-4-Methylcoumarin in the Lowest Excited Singlet State. *J. Phys. Chem.* **1979,** *83*, 447-451.

34. Trozzolo, A. M.; Dienes, A.; Shank, C. V. Excited-State Reactions of a Laser Dye. Evidence for a Two-Step Phototautomerism in 7-Hydroxy-4-Methylcoumarin. *J. Am. Chem. Soc.* **1974,** *96*, 4699-4700.

35. Seixas de Melo, J. S.; Becker, R. S.; Macanita, A. L. Photophysical Behavior of Coumarins as a Function of Substitution and Solvent: Experimental Evidence for the Existence of a Lowest Lying 1(n,.pi.*) State. *J. Phys. Chem.* **1994,** *98*, 6054-6058.

36. Moriya, T. Excited-State Reactions of Coumarins. VII. The Solvent-Dependent Fluorescence of 7-Hydroxycoumarins. *Bull. Chem. Soc. Jpn.* **1988,** *61*, 1873-1886.

37. Moriya, T. Excited-State Reactions of Coumarins in Aqueous-Solutions. I. The Phototautomerization of 7-Hydroxycoumarin and Its Derivative. *Bull. Chem. Soc. Jpn.* **1983,** *56*, 6-14.

38. Kobayashi, T. Picosecond Kinetics of 4-Methylumbelliferone Fluorescence Observed with Mode-Locked Laser and Streak Camera. *J. Phys. Chem.* **1978,** *82*, 2277-2281.

39. Bardez, E.; Boutin, P.; Valeur, B. Photoinduced Biprotonic Transfer in 4-Methylumbelliferone. *Chem. Phys. Lett.* **1992,** *191*, 142-148.

40. Georgieva, I.; Trendafilova, N.; Aquino, A. J. A.; Lischka, H. Excited State Properties of 7-Hydroxy-4-Methylcoumarin in the Gas Phase and in Solution. A Theoretical Study. *J. Phys. Chem. A* **2005,** *109*, 11860-11869.

41. Miertus, S.; Scrocco, E.; Tomasi, J. Electrostatic Interaction of a Solute with a Continuum - A Direct Utilization of Abinitio Molecular Potentials for the Prevision of Solvent Effects. *Chem. Phys.* **1981,** *55*, 117-129.

42. Tomasi, J.; Perisco, M. Molecular Interactions in Solution: An Overview of Methods Based on Continuous Distributions of the Solvent. *Chem. Rev.* **1994,** *94*, 2027-2094.

43. Georgieva, I.; Trendafilova, N.; Aquino, A. J. A.; Lischka, H. Excited-State Proton Transfer in 7-Hydroxy-4-Methylcoumarin Along a Hydrogen-Bonded Water Wire. *J. Phys. Chem. A* **2007,** *111*, 127-135.

44. Day, P. N.; Jensen, J. H.; Gordon, M. S.; Webb, S. P.; Stevens, W. J.; Krauss, M.; Garmer, D.; Basch, H.; Cohen, D. An Effective Fragment Method for Modeling Solvent Effects in Quantum Mechanical Calculations. *J. Chem. Phys.* **1996,** *105*, 1968-1986.

45. Gordon, M. S.; Freitag, A. M.; Bandyopadhyay, P.; Jensen, J. H.; Kairys, V.; Stevens, W. J. The Effective Fragment Potential Method: A QM-Based MM

Approach to Modeling Environmental Effects in Chemistry. *J. Phys. Chem. A* **2001,** *105,* 293-307.

46. Adamovic, I.; Freitag, M. A.; Gordon, M. S. Density Functional Theory Based Effective Fragment Potential Method. *J. Chem. Phys.* **2003,** *118,* 6725-6732.

47. Perdew, J. P.; Burke, K.; Ernzerhof, M. Generalized Gradient Approximation Made Simple. *Phys. Rev. Lett.* **1996,** *77,* 3865-3868.

48. Perdew, J. P.; Burke, K.; Ernzerhof, M. Generalized Gradient Approximation Made Simple *Phys. Rev. Lett.* **1997,** *78,* 1396-1396.

49. Adamo, C.; Barone, V. Toward Reliable Density Functional Methods without Adjustable Parameters: The PBE0 Model. *J. Chem. Phys.* **1999,** *110,* 6158-6170.

50. Ishida, K.; Morokuma, K.; Komornicki, A. The Intrinsic Reaction Coordinate. An Ab Initio Calculation for HNC→HCN and H−+CH4→CH4+H− *J. Chem. Phys.* **1977,** *66,* 2153-2156.

51. Muller, K. Reaction Paths on Multidimensional Energy Hypersurfaces. *Angew. Chem. Int. Ed. Engl.* **1980,** *19,* 1-13.

52. Schmidt, M. W.; Gordon, M. S.; Dupuis, M. The Intrinsic Reaction Coordinate and the Rotational Barrier in Silaethylene. *J. Am. Chem. Soc.* **1985,** *107,* 2585-2589.

53. Garrett, B. C.; Redmon, M. J.; Steckler, R.; Truhlar, D. G.; Baldridge, K. K.; Bartol, D.; Schmidt, M. W.; Gordon, M. S. Algorithms and Accuracy Requirements for Computing Reaction Paths by the Method of Steepest Descent. *J. Phys. Chem.* **1988,** *92,* 1476-1488.

54. Baldridge, K. K.; Gordon, M. S.; Steckler, R.; Truhlar, D. G. Ab Initio Reaction Paths and Direct Dynamics Calculations. *J. Phys. Chem.* **1989,** *93,* 5107-5119.

55. Gonzales, C.; Schlegel, H. B. An Improved Algorithm for Reaction Path Following. *J. Chem. Phys.* **1989,** *90,* 2154-2161.

56. Singh, U. C.; Kollman, P. A, An Approach to Computing Electrostatic Charges for Molecules. *J. Comput. Chem.* **1984,** *5,* 129-145.

57. Bayly, C. I.; Cieplak, P.; Cornell, W. D.; Kollman, P. A. A Well-Behaved Electrostatic Potential Based Method Using Charge Restraints for Deriving Atomic Charges - The Resp Model. *J. Phys. Chem.* **1993,** *97,* 10269-10280.

58. Day, P. N.; Pachter, R.; Gordon, M. S.; Merrill, G. N. A Study of Water Clusters Using the Effective Fragment Potential and Monte Carlo Simulated Annealing. *J. Chem. Phys.* **2000,** *112,* 2063-2073.

59. Metropolis, N.; Rosenbluth, A. W.; Rosenbluth, M. N.; Teller, A. H.; Teller, E. Equation of State Calculations by Fast Computing Machines. *J. Chem. Phys.* **1953,** *21*, 1087-1092.

60. Kirkpatrick, S.; Gelatt, C. D.; Vecchi, M. P. Optimization by Simulated Annealing. *Science* **1983,** *220*, 671-680.

61. Schmidt, M. W.; Baldridge, K. K.; Boatz, J. A.; Elbert, S. T.; Gordon, M. S.; Jensen, J. H.; Koseki, S.; Matsunaga, N.; Nguyen, K. A.; Su, S. *et al.* General Atomic and Molecular Electronic Structure System. *J. Comput. Chem.* **1993,** *14*, 1347-1363.

62. Gordon, M. S.; Schmidt, M. W. *Advances in Electronic Structure Theory: GAMESS a Decade Later*. Elsevier: Amsterdam, The Netherlands, 2005.

63. Bode, B. M.; Gordon, M. S. MacMolPlt: A Graphical User Interface for GAMESS. *J. Mol. Graphics Modell.* **1998,** *16*, 133-138.

64. Tanner, C.; Manca, C.; Leutwyler, S. Exploring Excited-State Hydrogen Atom Transfer Along an Ammonia Wire Cluster: Competitive Reaction Paths and Vibrational Mode Selectivity. *J. Chem. Phys.* **2005,** *122*, 204326-204336.
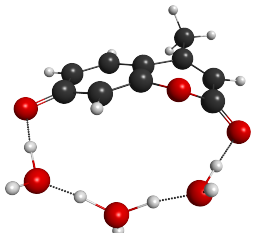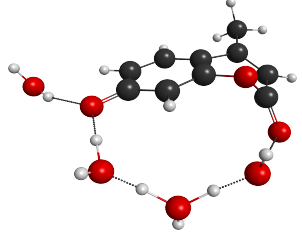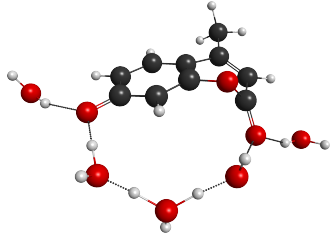
Table I. The 0K relative enthalpies (H_{rel}^0) of the C456 tautomers. The relative energies are given relative to the S_0 state of enol tautomer. The values in parenthesis are relative energies without zero point energy correction (E_{rel}). All values are given in eV.

| | S_0 | | S_1 | |
	Enol	Keto	Keto	Enol
C456	0.00 (0.00)	1.09 (1.11)	3.67 (3.77)	3.90 (4.05)
C456:3H$_2$O	0.00 (0.00)	0.77 (0.80)	3.58 (3.71)	3.72 (3.85)
C456:PCM	0.00 (0.00)	0.93 (0.95)	3.68 (3.78)	3.71 (3.81)
C456:3H$_2$O+PCM	0.00 (0.00)	0.70 (0.71)	3.54 (3.64)	3.59 (3.68)
C456:3H$_2$O+200EFP	0.00 (0.00)	0.24 (0.27)	3.22 (3.34)	3.47 (3.60)

Table II. The S_0 and S_1 0K activation energies ($E_{a(E \to K)}$ and $E_{a(E^* \to K^*)}$) of the enol→keto tautomerization of the C456 complexes. The energies without ZPE corrections are given in parentheses. All values are given in eV.

	S_0	S_1
C456:3H$_2$O	0.87 (1.09)	0.23 (0.44)
C456:3H$_2$O+PCM	0.70 (0.84)	0.20 (0.29)
C456:3H$_2$O+200EFP	0.44 (0.66)	-0.22 (-0.01)

Table III. The excited state activation energy (eV), $E_{a(E^*\to K^*)}$, of the enol→keto tautomerization reaction of C456:3H$_2$O+nEFP.

n	i	$E_{a(E^*\to K^*)}$	TS^*
0	629	0.23 (0.44) [0.38]	
1	541	0.12 (0.33) [0.33]	
2	492	0.11 (0.32) [0.33]	

[a]The barrier height, $E_{b(E^*\to K^*)}$ is given in parenthesis.

[b]The barrier height, $E_{b(E^*\to K^*)}$ calculated using the single point energies on the above structures with PCM are given in square brackets.

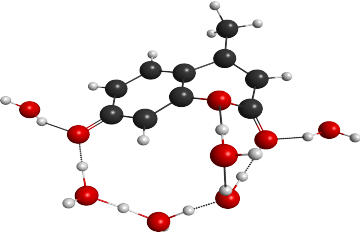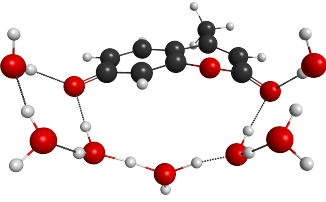[c]The imaginary frequency (i) of the TS* is given in cm^{-1}.

Table III. (continued).

n	i	$E_{a(E^*\to K^*)}$	TS^*
3	599	-0.02 (0.19) [0.21]	
4	353	-0.17 (0.04) [0.07]	

Table IV. The TDPBE0/DH(d,p) vertical excitation (absorption), adiabatic, and vertical de-excitation (fluorescence) energies for the C456 enol tautomer. All energies are given in eV. The adiabatic energies are given with the ZPE correction. The values in parenthesis are the adiabatic energies without the ZPE correction.

Enol tautomer	Vertical	Adiabatic	Fluorescence	Exp
C456	4.28	3.90 (4.05)	3.58	3.88[a]
C456:$3H_2O$	4.04	3.72 (3.85)	3.05	
C456:PCM	4.17	3.71 (3.81)	3.62	
C456:$3H_2O$+PCM	4.03	3.59 (3.68)	3.31	
C456:$3H_2O$+200EFP	4.15	3.47 (3.60)	3.00	

[a]Absorption energy of the enol tautomer of C456 in benzene.[36]

Table V. The TDPBE0/DH(d,p) vertical excitation (absorption), adiabatic, and vertical de-excitation (fluorescence) energies for keto tautomer of C456. All energies are given in eV. The adiabatic energies are given with the ZPE correction. The values in parenthesis are the adiabatic energies without the ZPE correction.

Keto tautomer	Vertical	Adiabatic	Fluorescence	Exp
C456	3.02	2.59 (2.66)	2.27	3.33[a]
C456:3H_2O	3.20	2.81 (2.90)	2.52	
C456:PCM	3.18	2.75 (2.83)	2.59	
C456:3H_2O+PCM	3.24	2.84 (2.93)	2.71	
C456:3H_2O+200EFP	3.64	2.98 (3.07)	3.04	

[a]Fluorescence energy of the keto tautomer of C456 in benzene.[36]
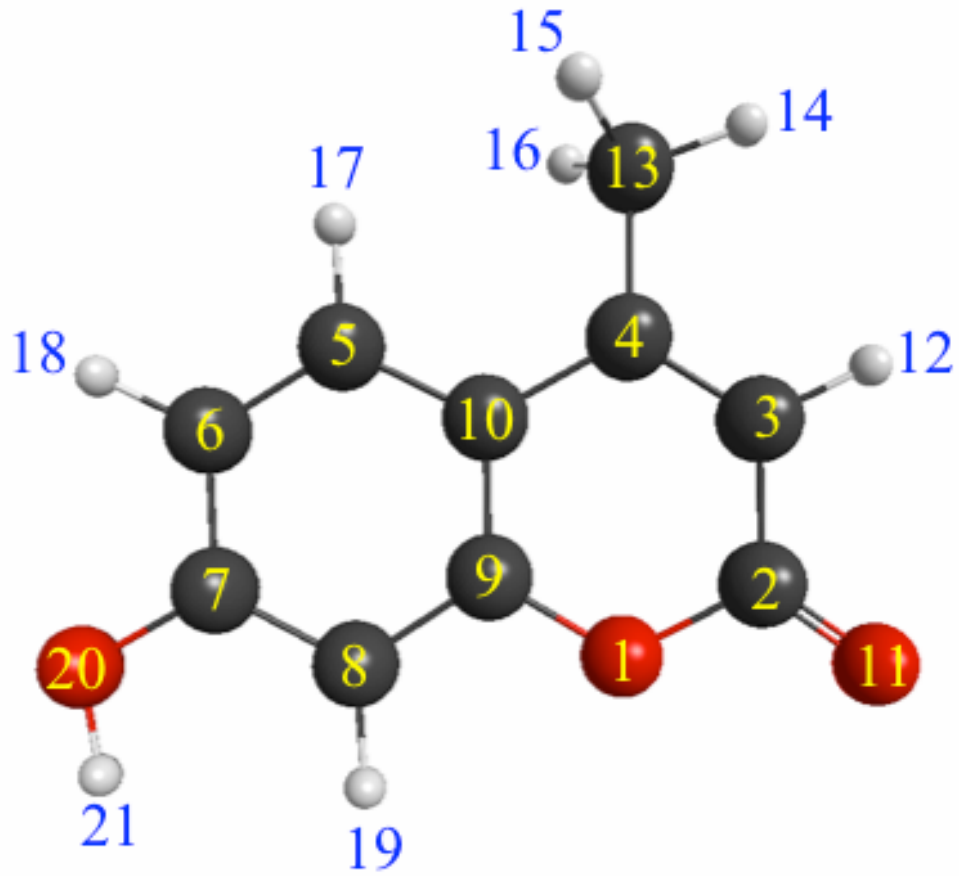
(a) C456

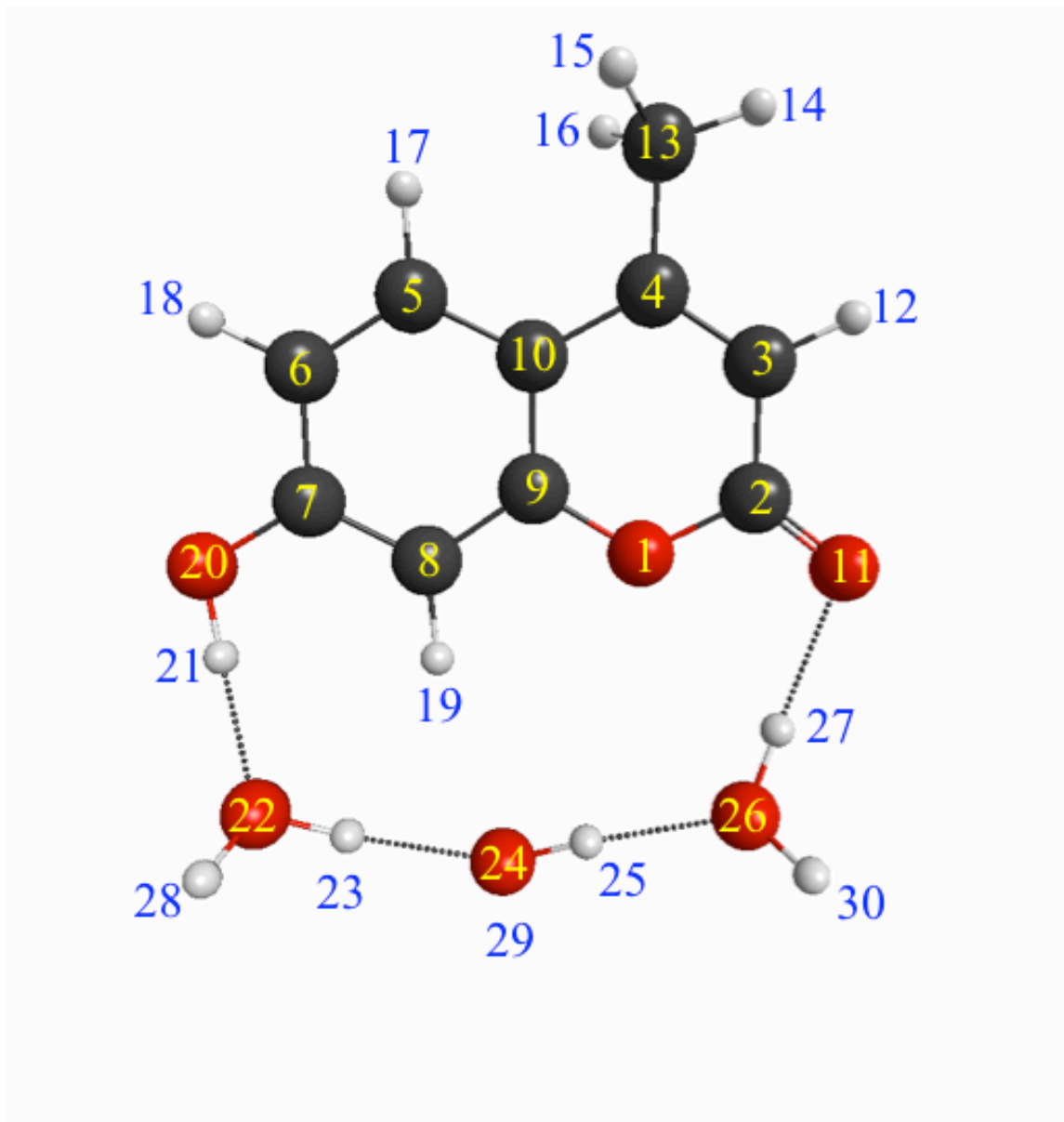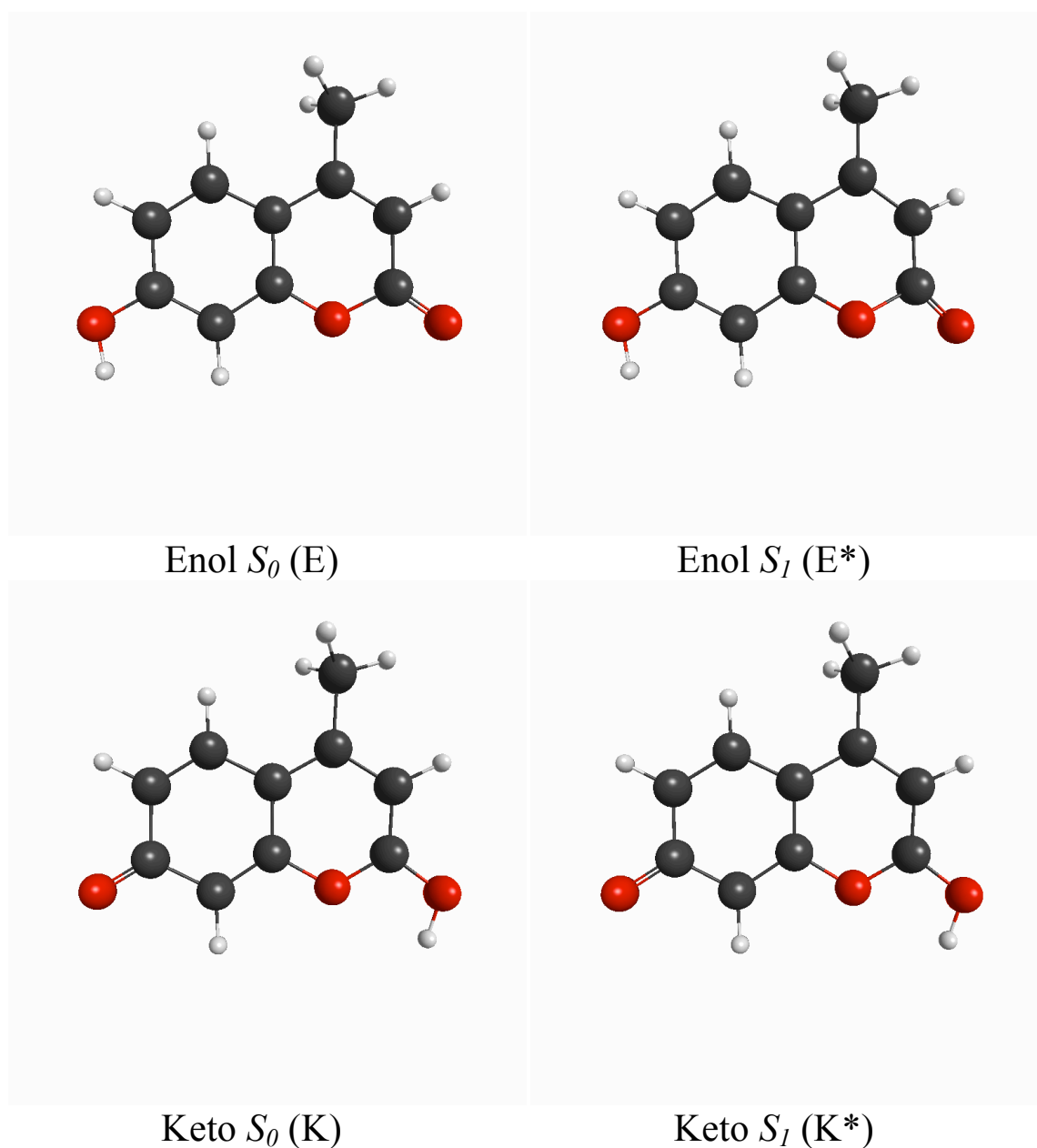**Figure 1.** The atom labeling of the (a) C456 and (b) C456:3H$_2$O.

(b) C456:3H$_2$O

Figure 1. (continued)

Enol S_0 (E)

Enol S_1 (E*)

Keto S_0 (K)

Keto S_1 (K*)

(a) Perpendicular view

Figure 2. The optimized geometries of the C456 stationary points of S_0 (E, TS, and K) and S_1 (E*, TS*, and K*) optimized, respectively, with PBE0/DH(d,p) and TDPBE0/DH(d,p). The molecular geometry is shown in two different views (directions) relative to the molecular fused-ring plane: (a) Perpendicular view and (b) Parallel view.

Enol S_0 (E)

Enol S_1 (E*)

Keto S_0 (K)

Keto S_1 (K*)
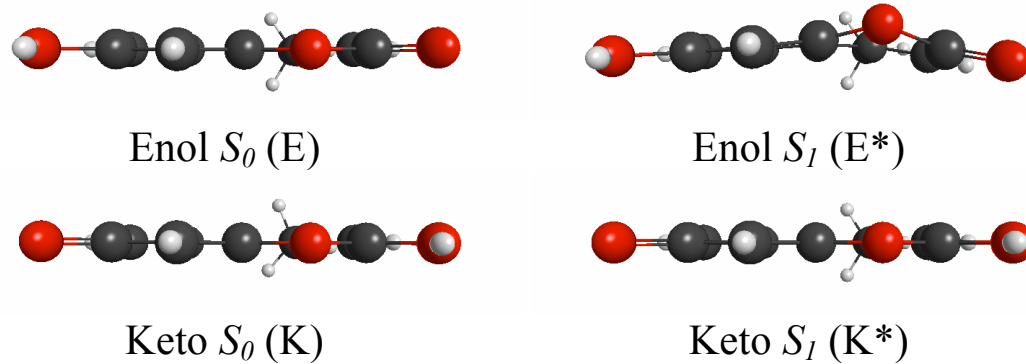
(b) Parallel view

Figure 2. (continued)

Enol S_0 (E)

Enol S_1 (E*)

TS S_0 (TS)

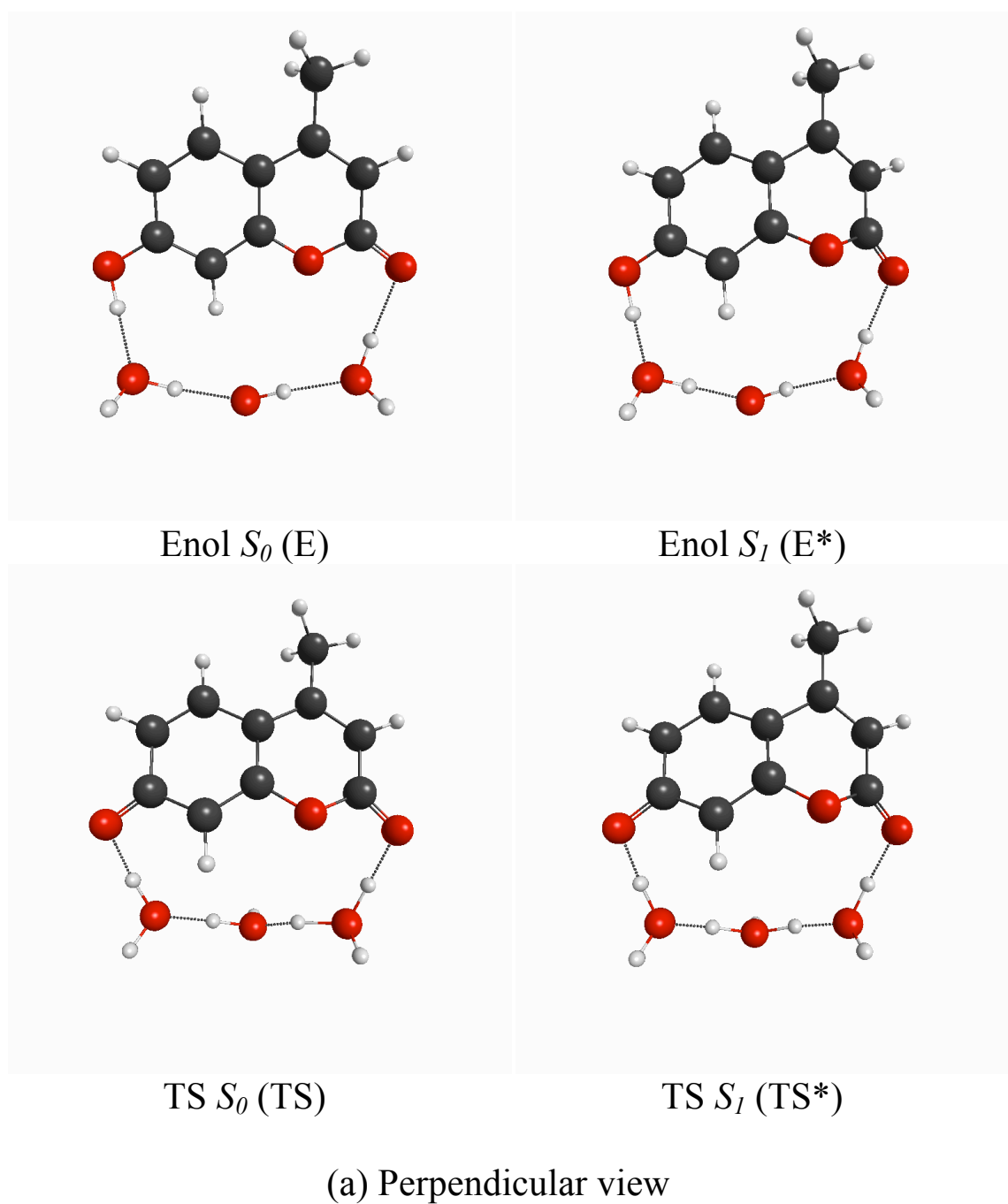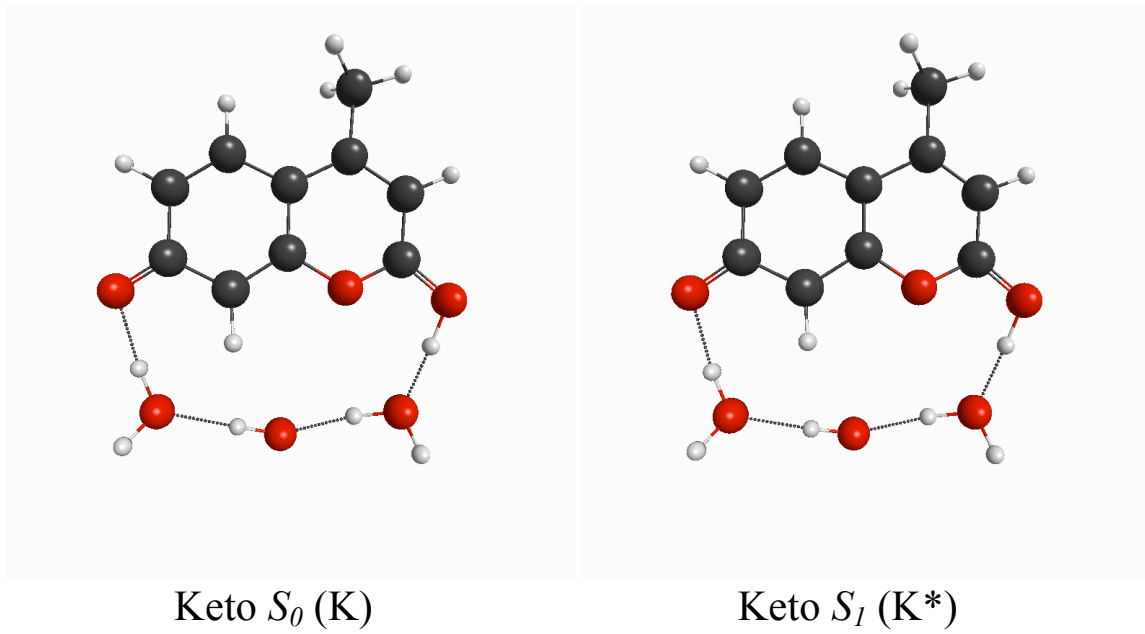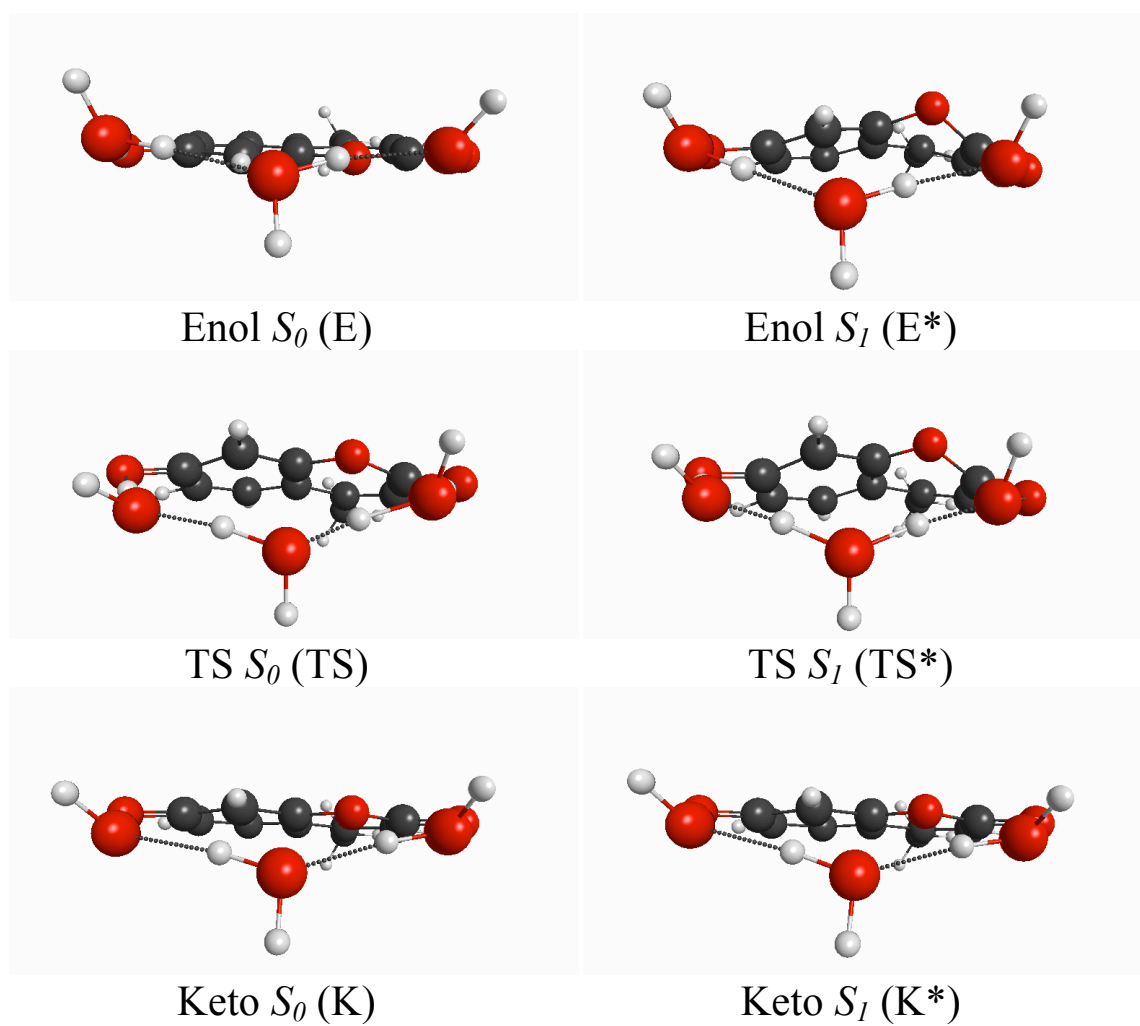TS S_1 (TS*)

(a) Perpendicular view

Figure 3. The geometries of the stationary points of S_0 (E, TS, and K) and S_1 (E*, TS*, and K*) of C456:3H$_2$O optimized, respectively, with PBE0/DH(d,p) and TDPBE0/DH(d,p). The molecular geometry is shown in two different views (directions) relative to the molecular fused-ring plane: (a) Perpendicular view and (b) Parallel view.

Keto S_0 (K)   Keto S_1 (K*)

(a) Perpendicular view

Figure 3. (continued)

Enol S_0 (E)

Enol S_1 (E*)

TS S_0 (TS)

TS S_1 (TS*)

Keto S_0 (K)

Keto S_1 (K*)
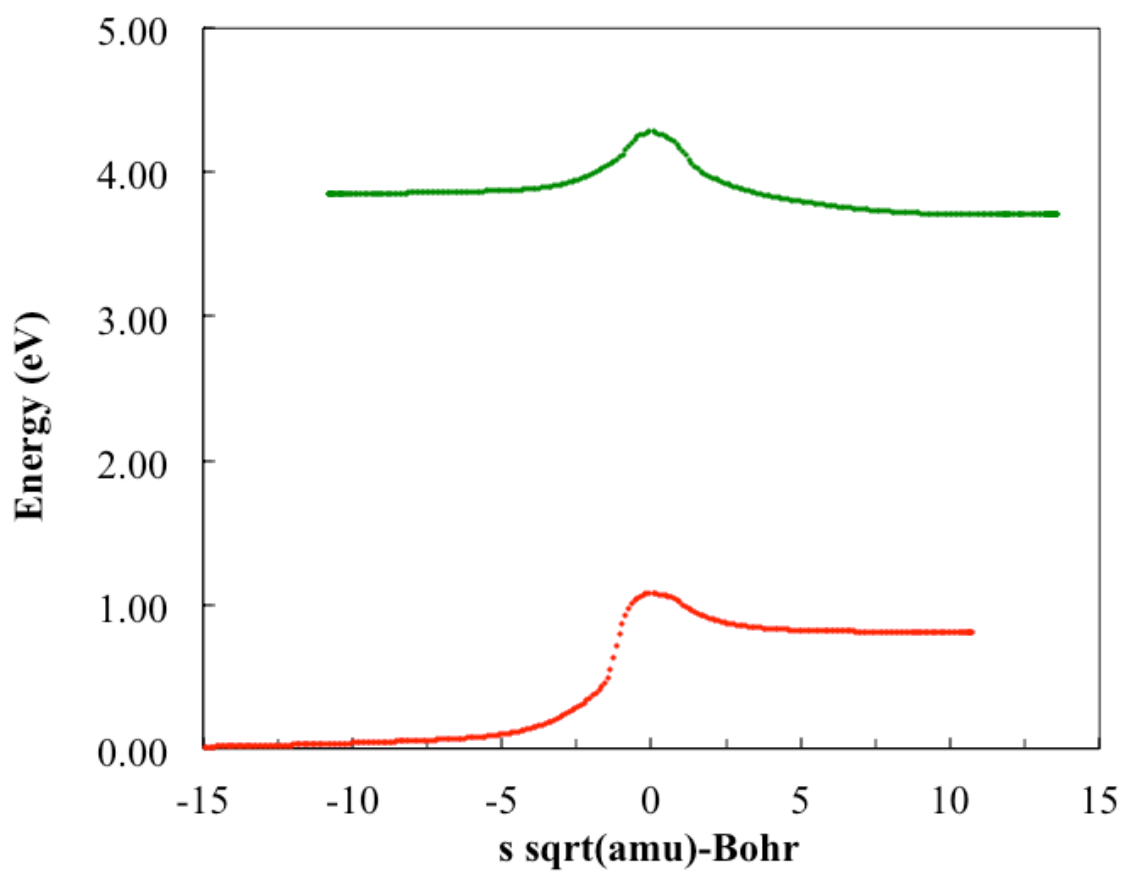
(b) Parallel view

Figure 3. (continued)

Figure 4. The IRC path in the ground state (red) and the first π-π* excited state (green) of C456:3H$_2$O calculated with PBE0/DH(d,p) and TDPBE0/DH(d,p), respectively, starting from the corresponding transition states.
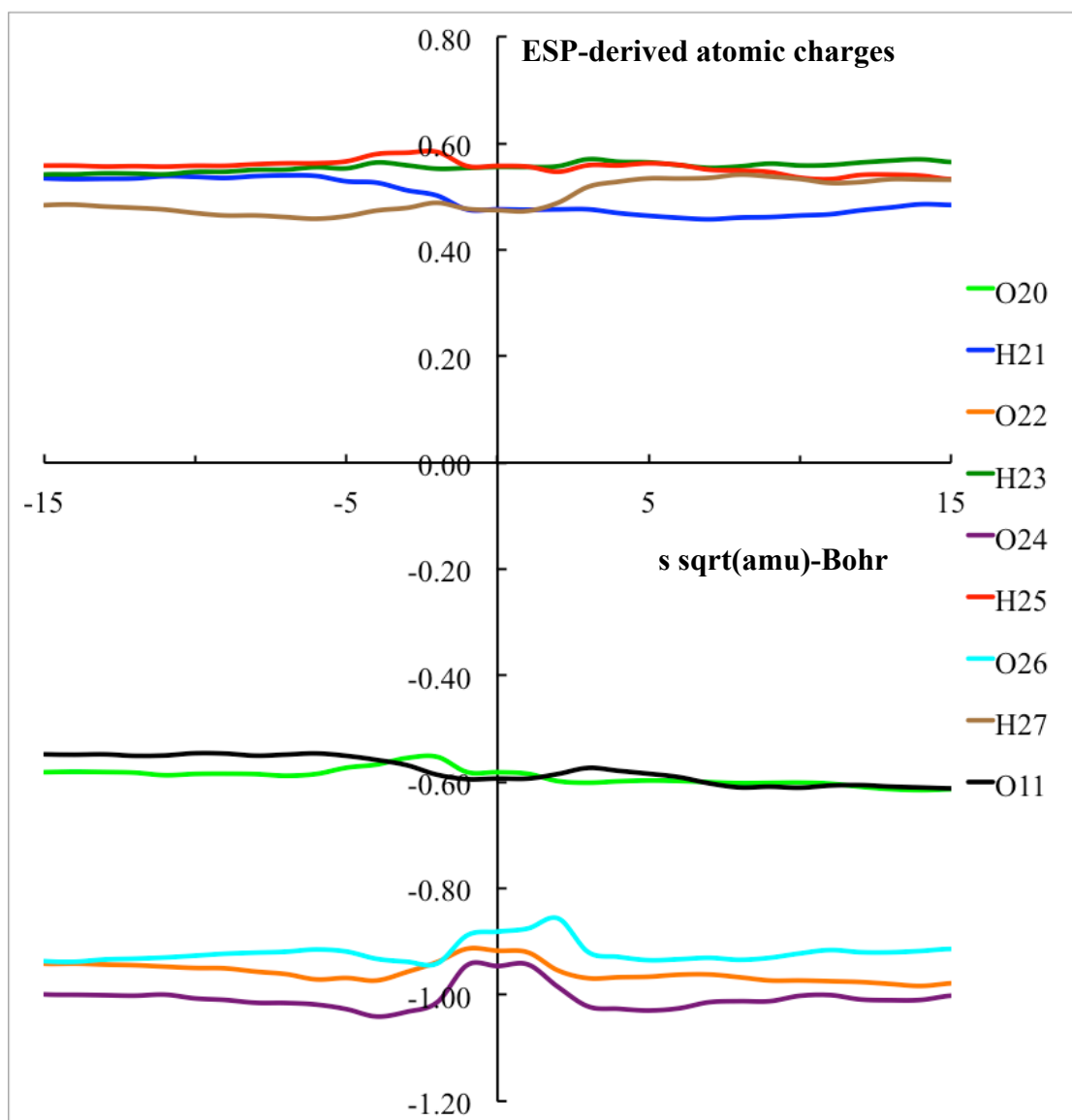
Figure 5. The ESP-derived TDPBE0/DH(d,p) atomic charges on the O20, H21, O22, H23, O24, H25, O26, H27, and O11 atoms along the IRC path of the S_1 state of C456:3H_2O.
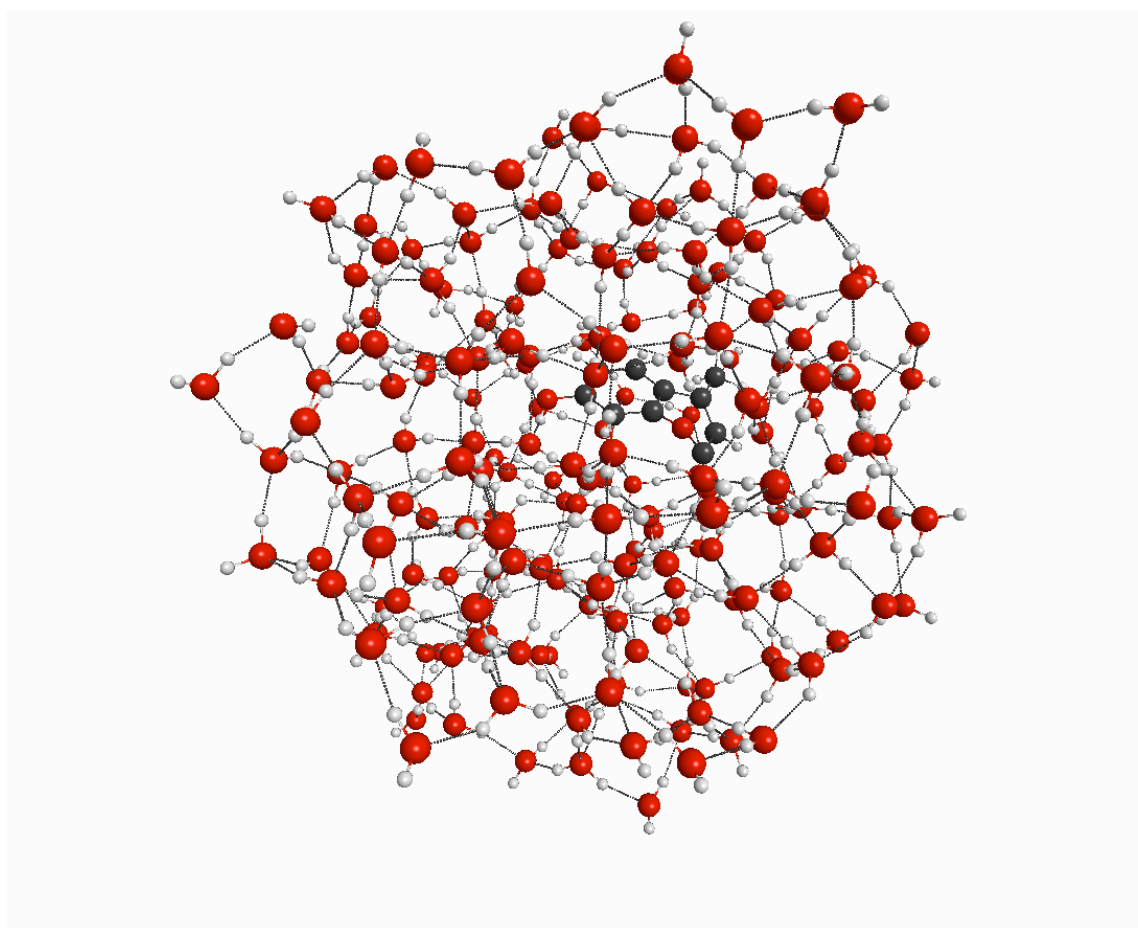
Figure 6. Global minima of the excited state enol tautomer of C456:3H$_2$O in 200 EFP. The hydrogen, carbon and oxygen atoms are colored white, black, and red, respectively.

CHAPTER 6. QM−EFP1 DISPERSION INTERACTION

A paper to be submitted to *The Journal of Physical Chemistry A*

Nuwan De Silva, Luke Roskop, Sarom S. Leang and Mark S. Gordon*

Abstract

An empirical dispersion energy correction for systems that contain the effective fragment potential for water molecules (EFP1) and *ab initio* quantum mechanical (QM) molecules have been implemented in the GAMESS electronic structure code. The interaction energy between QM molecules and EFP1 water molecules using this EFP1−D method were tested using the water dimer and benzene−water clusters. The QM−EFP1−D interaction energies are compared with the predictions obtained using the fully QM Hartree-Fock and second order perturbation theory methods, as well as the generalized effective fragment potential (EFP2) method, all with the 6-311++G(3df,2p) basis set. The results show that the QM−EFP1−D method can capture the essence of the more sophisticated EFP2−EFP2 interaction energies.

I. Introduction

Intermolecular interactions between solute and solvent play a vital role in many applications related to chemistry, physics, and biology. Often the solvent environment alters the solute properties such as reactivity, spectroscopy, and dynamics via solute−solvent intermolecular interactions. The main intermolecular interactions, which contribute to the total intermolecular interaction energy are electrostatics (Coulombic), induction (polarization), van der Waals interactions (dispersion), exchange repulsion, and charge transfer (CT) interactions. The Coulomb, polarization, and dispersion interactions are long-range interactions. The exchange repulsion and CT are short-range interactions. Depending on the physical and chemical nature of the solute and solvent molecules, which take part in the interaction, the contribution from each interaction type to the total interaction energy can vary significantly.

Quantum mechanical (QM) methods such as second-order perturbation theory (MP2)[1] and coupled cluster (CC) theory,[2,3] capture the aforementioned interactions via first principles inclusion of electron correlation. Energy decomposition methods such as symmetry adapted perturbation theory[4,5] and various energy decomposition analysis (EDA) schemes[6-16] help to interpret the total QM interaction energy in terms of physically meaningful components. However, most correlated fully QM calculations are limited to relatively small systems due to the high computational cost of these methods. An alternative approach to the study of intermolecular interactions is to use a model

potential. Some model potentials, sometimes called molecular mechanics (MM) potentials, can account for the range of intermolecular interactions. There are a few model potentials that are mainly classical in nature but are derived from rigorous QM approaches. One such sophisticated model potential is the effective fragment potential (EFP)[17-20] method that is implemented in the GAMESS (General Atomic and Molecular Electronic Structure System) electronic structure package.[21,22]

There are two versions of the EFP method: EFP1 and EFP2. EFP1 is strictly a water potential, while EFP2 is completely general. However, the EFP2 method has not been fully integrated with QM methods. The EFP1 interaction energy[17,18] is written as follows:

$$E\left(\text{EFP1}\right) = E^{Coul} + E^{Pol} + E^{Rem} \tag{1}$$

where E^{Coul} denotes the Coulomb interaction, calculated according to the distributed multipole analysis (DMA) suggested by Stone,[23,24] with the expansion points located at the atom centers and the bond midpoints. The polarization term E^{Pol} is determined using a tensor sum of localized molecular orbital (LMO) polarizability tensors that are centered at the LMO centroids. The third term in Eq. (1), E^{Rem}, is a remainder term that is obtained by subtracting the first two terms from the total QM interaction energy of the water dimer and fitting the remainder to a functional form that depends on whether one is considering a QM−EFP1 interaction or an EFP1−EFP1 interaction. The QM−EFP1 interaction energy has been fitted using Hartree-Fock (EFP1/HF) and density functional theory (DFT) with the B3LYP functional[25,26] [EFP1/DFT].[27] The EFP1 method has

successfully been interfaced with most QM methods. In addition to HF and DFT, these methods include time-dependent DFT (TDDFT),[28] singly excited configuration interaction (CIS),[29] multiconfiguration self-consistent field (MCSCF), MP2 and multireference MP2 (MRPT2),[30] and CC theory. Most applications of the EFP1 method have been devoted to determining aqueous solvent effects on ground and electronically excited state QM properties and processes.[28-62] However, the missing long-range interaction type in the QM−EFP1 formulation is the dispersion interaction energy, since dispersion is not included in the HF or B3LYP methods to which EFP1 was fit. Dispersion can be important in water interactions, including those with nonpolar species such as benzene.[63,64]

The EFP2 interaction energy may be written as follows:

$$E\left(\text{EFP2}\right) = E^{Coul} + E^{Pol} + E^{Exrep} + E^{Disp} + E^{CT} \tag{2}$$

where the E^{Coul} and E^{Pol} terms are determined as described above. The E^{Exrep}, E^{Disp}, and E^{CT} terms are derived from first principles. Hence, there are no empirically fitted parameters in EFP2. Generally, the EFP2 method can represent any solvent. In many applications,[20,65-67 68,69 63,70-72] it has been shown that the EFP2 method can accurately predict the broad range of intermolecular interactions including the dispersion interaction. EFP2 is an attractive method due to its low computational cost. The accuracy of EFP2 for intermolecular interactions is frequently comparable to that of MP2.[73] However, since the QM−EFP2 analytic gradients have not been fully implemented, the use of the QM−EFP2 method is limited. Therefore, it is desirable to improve the accuracy of the EFP1 method

by including dispersion interactions, where the QM−EFP1 analytical gradient is available.

The dispersion interaction arises from an attractive force between atoms and molecules that is caused by the interactions of induced multipoles. Dispersion arises from the correlated movement of electrons; an instantaneous multipole on one molecule may induce a multipole on another molecule.[24,74] Dispersion could be introduced into the EFP1 method in a manner that is analogous to the Grimme dispersion correction to DFT (DFT−D) or HF (HF−D). Such a method can be called EFP1−D. The Grimme dispersion correction [75-77] to the HF or DFT method is summarized below. The EFP1−D method is formulated in the same way. There are three −D implementations: DFT−D,[75] DFT−D2,[76] and DFT−D3.[77] In this paper the DFT−D3 implementation is used. For simplicity of notation, throughout this paper, the DFT−D3 method will be referred to as the −D correction.

The dispersion correction to the HF total electronic energy, HF−D, has the following form:

$$E_{HF-D} = E_{HF} + E^{Disp} \tag{3}$$

where E_{HF} is the HF energy and E^{Disp} is an empirical dispersion correction given by a sum of two- and three-body energies:

$$E^{Disp} = E^{(2)} + E^{(3)} \tag{4}$$

The most important two-body term $E^{(2)}$ is given by

$$E^{(2)} = -\sum_{B>A}^{N} \sum_{n=6,\,8} s_n \frac{C_n^{AB}}{R_{AB}^n} f_{damp}(R_{AB}) \tag{5}$$

where, N denotes the number of atoms in the molecule, C_n^{AB} denotes the averaged nth-order dispersion coefficient (where $n = 6, 8$) for atom pair A and B, and R_{AB} is the internuclear distance between atom pair A and B. The term s_n is a global scaling factor that is set to 1.0 for HF. For DFT, s_6 is 1.0 but s_8 is typically used to adjust the correction to the repulsive behavior of the chosen density functional. To avoid singularities for small R_{AB}, a damping function f_{damp} must be used:

$$f_{damp}(R_{AB}) = \frac{1}{1 + 6\left(R_{AB}/s_{r,n} R_0^{AB}\right)^{-\alpha_n}} \tag{6}$$

where R_0^{AB} is a cutoff radius for atom pair A and B. The $s_{r,n}$ term is an order-dependent scaling factor for the cutoff radii R_0^{AB}. For HF $s_{r,n}$ is set to unity. For DFT $s_{r,n}$ is a density functional-dependent scaling factor[78] The exponent α_n is a constant that determines the steepness of the functions for small R_{AB}. The damping function is important because at small R_{AB} it decays fast enough to zero that the atom-atom dispersion corrections at distances below typical van der Waals distances are negligible.

The three-body term $E^{(3)}$ is given by

$$E^{(3)} = -\sum_{ABC} f_{d,(3)}(\bar{R}_{ABC}) E^{ABC} \tag{7}$$

where the sum is over all atom triples *ABC*. The term $f_{d,(3)}$ is a damping function that is similar to the one in Eq. (6). Geometrically averaged radii between atoms A, B, and C ($\overline{R}_{ABC}$) are used. E^{ABC} is the nonadditive (called Axilrod–Teller–Muto or triple dipole) dispersion term as derived from third-order perturbation theory for three atoms A, B, C: [24] [79]

$$E^{ABC} = \frac{C_9^{ABC}\left(3\cos\theta_a \cos\theta_b \cos\theta_c + 1\right)}{\left(R_{AB}R_{BC}R_{CA}\right)^3} \tag{8}$$

where θ_a, θ_b, and θ_c are the internal angles of the triangle formed by R_{AB}, R_{BC} and R_{CA}, and C_9^{ABC} is the triple-dipole constant approximately defined by

$$C_9^{ABC} \approx -\sqrt{C_6^{AB}C_6^{AC}C_6^{BC}} \tag{9}$$

II. Computational Details

In this study, the water dimer (W2) and benzene with one (BW1) and eight (BW8) water molecules were studied using the dispersion correction to QM−EFP1. All calculations in the present work were performed with the GAMESS electronic structure code. The W2, BW1 and BW8 complexes are fully optimized with HF (QM−QM), MP2 (QM−QM), QM−EFP1/HF and EFP2−EFP2, all using the 6-311++G(3df,2p) basis set, in C_1 symmetry. The water and benzene monomers, as well as the eight-water cluster, were optimized at the corresponding level of theory. The HF−D dispersion correction was made to the interaction energies obtained with HF and EFP1/HF. QM−EFP1 and

EFP2−EFP2 energy decompositions were also performed. The Kitaura–Morokuma interaction energy decomposition analysis[6] was carried out at the HF/6-311++G(3df,2p) level of theory.

III. Results and Discussion

Tables 1−3 summarize the predicted center of mass to center of mass intermolecular distances (R_e) and the interaction energies (D_e) with the energy decomposition analysis for W2, BW1, and BW8 complexes. Figure 1 illustrates the MP2/6-311++G(3df,2p) optimized structures of the W2, BW1, and BW8 complexes.

One water molecule in W2 is a hydrogen donor and the other is a hydrogen acceptor in the hydrogen bond interaction. So, for the QM and EFP1 interaction of W2, there can be two different arrangements: [1] the donor molecule is QM and the acceptor is EFP1 (QM−EFP1), or [2] the donor molecule is EFP1 and the acceptor molecule is QM (EFP1−QM). As shown in Table 1, the HF (QM−QM), QM−EFP1, EFP1−QM, EFP1−EFP1, and EFP2−EFP2 levels predict an optimum inter-monomer separation ~ 0.1 Å wider than that found with MP2 (QM−QM). The EFP1−EFP1 optimum separation for W2 (3.0 Å) is identical to that found with EFP2−EFP2. Compared to MP2 (QM−QM), the EFP2−EFP2 W2 is more strongly bound, by 1.0 kcal/mol.

155

The main attractive term in W2 interactions is the Coulombic energy, because it is an interaction between two polar molecules. However, the W2 interaction also has considerable exchange-repulsion energy. For example, the EFP2−EFP2 Coulomb energy is around −10 kcal/mol but the exchange repulsion is large as +7 kcal/mol. The polarization and the dispersion contributions to D_e are small and they have similar magnitudes to each other. The EFP2−EFP2 dispersion energy is about −1.7 kcal/mol but the −D correction is about −0.8 kcal/mol. Adding the −D correction to the HF (QM−QM) energy, is important to recover the MP2 D_e within about 0.6 kcal/mol.

Inclusion of a −D correction to the QM−EFP1 and EFP1−EFP1 D_e brings their accuracy closer to EFP2−EFP2, within about 0.5 kcal/mol. However, the −D corrected EFP1−QM D_e is still about 1.3 kcal/mol less negative than that of EFP2−EFP2. This may partly be explained by the fact that the basis set used to fit the EFP1 E^{Rem} term is much smaller than the one used in the present work.

The oxygen atom and one of the hydrogen atoms in the water molecule are oriented almost perpendicular to the plane of the benzene ring in the BW1 complex. In the BW1 complex, the negatively charged benzene π-cloud donates electron density to the water hydrogen atom, which is pointed towards the benzene ring. Therefore, the water molecule acts as a hydrogen bond donor and the benzene acts as a hydrogen bond acceptor. The experimental values of the intermolecular distances, (R_e) determined as the distances between the centers of mass in BW1, ranges from 3.32 to 3.35 Å.[80-82] Table 2 shows that MP2 and EFP2−EFP2 underestimate the experimental value by 0.1 Å,

whereas HF and QM−EFP1 overestimate the BW1 experimental value by about 0.4 Å. Experimentally, there is considerable variation in the measured BW1 binding energy (D_0), with a range from −1.63 to −2.78 kcal/mol.[80] Calculated binding energies D_e dramatically depend on the method and basis set used.[63] Feller and coworkers[83] predicted the MP2 D_0 to be 2.9 ± 0.2 kcal/mol (D_0 = 3.9 ± 0.2 kcal/mol and ZPE = 1.0 kcal/mol) with an estimated complete basis set (CBS) limit. The aforementioned ZPE of 1.0 kcal/mol can be used to estimate the QM−EFP1−D D_0 to be −3.7 kcal/mol (The QM−EFP1−D D_e is −4.7 kcal/mol) in very good agreement with the MP2/CBS limit (within 1 kcal/mol) and the experimental values (within 1−2 kcal/mol). The dispersion correction in the BW1 complex is about −2 kcal/mol. The main attractive contribution to the D_e comes from E^{Coul} and E^{Disp} for the binding of the BW1 van der Waals complex.

As shown in Figure 1, the oxygen atoms of the eight water molecules in BW8 are arranged in a cubic structure. The water molecules are arranged in different orientations and bind to each other via hydrogen bonds to form the cubic structure. In the BW8 complex (Figure 1), the water molecules are labeled 1 through 8. One of the water hydrogen atoms in water molecule 1 is pointed towards the benzene ring. Table 3 summarizes the BW8 calculated data in this work. In the BW8 complex the R_e predicted by HF and QM−EFP1 are both almost the same as the EFP2−EFP2 and MP2 R_e. The QM−EFP1−D D_e has almost the same value as the EFP2−EFP2 D_e (within 0.1 kcal/mol). This is important evidence that the accuracy of the QM−EFP1−D interaction energy is very close to that of EFP2–EFP2. The D_e of MP2 in BW8 is about −6 kcal/mol, which is

about 2 kcal/mol more negative than that of BW1. Therefore, the addition of seven water molecules to the BW1 increases its D_e by about 50 percent.

IV. Conclusions

This paper presents a study of water−water (W2) and benzene−water (BW1 and BW8) complexes based on the both *ab initio* and effective fragment potential method. The binding energies in the clusters were evaluated at the HF and MP2 levels of theory with the 6-311++G(3df,2p) basis set. The binding energies also were computed with all possible QM−EFP and EFP−EFP arrangements. The dispersion correction to the QM−EFP1 interaction was introduced empirically and compared to the interaction energies of more general and highly accurate EFP2−EFP2.

The absolute difference in the interaction energies between HF−D (QM−QM) and MP2 (QM−QM) is 0.6 kcal/mol for W2, 0.6 kcal/mol for BW1, and 1.9 kcal/mol for BW8. Interestingly, the absolute difference in the interaction energies between QM−EFP1−D and EFP2−EFP2 is 0.4 kcal/mol for W2, 0.1 kcal/mol for BW1, and 0.1 kcal/mol for BW8. This means that the accuracy of the simple QM−EFP1−D method provides interaction energies that are almost equivalent to the more sophisticated EFP2−EFP2 approach for the dispersion dominant complexes such as benzene-water complexes. It is gratifying that the agreement between HF−EFP1−D and EFP2 for the

complexes studied here is slightly better than the agreement between HF−D and MP2 for the same complexes.

Acknowledgements

References

(1)   Moller, C.; Plesset, M. S. *Phys. Rev.* **1934**, *46*, 618-622.

(2)   Raghavachari, K.; Trucks, G. W.; Pople, J. A.; Head-Gordon, M. *Chem. Phys. Lett.* **1989**, *157*, 479-483.

(3)   Bartlett, R. J.; Musial, M. *Rev. Mod. Phys.* **2007**, *79*, 291-352.

(4)   Jeziorski, B.; Moszynski, R.; Szalewicz, K. *Chem. Rev.* **1994**, *94*, 1887-1930.

(5)   Moszynski, R.; Heijmen, T. G. A.; Jeziorski, B. *Mol. Phys.* **1996**, *88*, 741-758.

(6)   Kitaura, K.; Morokuma, K. *Int. J. Quantum Chem.* **1976**, *10*, 325-340.

(7)   Fedorov, D. G.; Kitaura, K. *J. Comput. Chem.* **2007**, *28*, 222-237.

(8)   Khaliullin, R. Z.; Cobar, E. A.; Lochan, R. C.; Bell, A. T.; Head-Gordon, M. *J. Phys. Chem. A* **2007**, *111*, 8753-8765.

(9)   Chen, W.; Gordon, M. S. *J. Phys. Chem.* **1996**, *100*, 14316-14328.

(10)   Stevens, W. J.; Fink, W. H. *Chem. Phys. Lett.* **1987**, *139*, 15-22.

(11)   Bagus, P. S.; Illas, F. *J. Chem. Phys.* **1992**, *96*, 8962-8970.

(12)   Bagus, P. S.; Hermann, K.; Bauschlicher, C. W., Jr. *J. Chem. Phys.* **1984**, *80*, 4378-4386.

(13)   Glendening, E. D. *J. Phys. Chem. A* **2005**, *109*, 11936-11940.

(14)   Glendening, E. D.; Streitwieser, A. *J. Chem. Phys.* **1994**, *100*, 2900-2909.

(15)   Mo, Y.; Gao, J.; Peyerimhoff, S. D. *J. Chem. Phys.* **2000**, *112*, 5530-5538.

(16)   Van, d. V. A.; Merz, K. M., Jr. *J. Phys. Chem. A* **1999**, *103*, 3321-3329.

(17)   Day, P. N.; Jensen, J. H.; Gordon, M. S.; Webb, S. P.; Stevens, W. J.; Krauss, M.; Garmer, D.; Basch, H.; Cohen, D. *J. Chem. Phys.* **1996**, *105*, 1968-1986.

(18)   Gordon, M. S.; Freitag, M. A.; Bandyopadhyay, P.; Jensen, J. H.; Kairys, V.; Stevens, W. J. *J. Phys. Chem. A* **2001**, *105*, 293-307.

(19)   Gordon, M. S.; Slipchenko, L.; Li, H.; Jensen, J. H. *Annu. Rep. Comput. Chem.* **2007**, *3*, 177-193.

(20)   Ghosh, D.; Kosenkov, D.; Vanovschi, V.; Williams, C. F.; Herbert, J. M.; Gordon, M. S.; Schmidt, M. W.; Slipchenko, L. V.; Krylov, A. I. *J. Phys. Chem. A* **2010**, *114*, 12739-12754.

(21)   Schmidt, M. W.; Baldridge, K. K.; Boatz, J. A.; Elbert, S. T.; Gordon, M. S.; Jensen, J. H.; Koseki, S.; Matsunaga, N.; Nguyen, K. A.; et, al. *J. Comput. Chem.* **1993**, *14*, 1347-1363.

(22)   Gordon, M. S.; Schmidt, M. W. *Theory and Applications of Computational Chemistry: The First Forty Years*; Elsevier: Amsterdam, The Netherlands, 2005.

(23)   Stone, A. J. *Chem. Phys. Lett.* **1981**, *83*, 233-239.

(24)   Stone, A. J. *The Theory of Intermolecular Forces.*; Oxford Univ. Press: New York, 1996.

(25)   Becke, A. D. *J. Chem. Phys.* **1993**, *98*, 5648-5652.

(26)   Lee, C.; Yang, W.; Parr, R. G. *Phys. Rev. B: Condens. Matter* **1988**, *37*, 785-789.

(27)   Adamovic, I.; Freitag, M. A.; Gordon, M. S. *J. Chem. Phys.* **2003**, *118*, 6725-6732.

(28)   Yoo, S.; Zahariev, F.; Sok, S.; Gordon, M. S. *J. Chem. Phys.* **2008**, *129*, 144112-144119.

(29)　Arora, P.; Slipchenko, L. V.; Webb, S. P.; DeFusco, A.; Gordon, M. S. *J. Phys. Chem. A* **2010**, *114*, 6742-6750.

(30)　DeFusco, A.; Ivanic, J.; Schmidt, M. W.; Gordon, M. S. *J. Phys. Chem. A* **2011**, *115*, 4574-4582.

(31)　Chen, W.; Gordon, M. S. *J. Chem. Phys.* **1996**, *105*, 11081-11090.

(32)　Merrill, G. N.; Gordon, M. S. *J. Phys. Chem. A* **1998**, *102*, 2650-2657.

(33)　Webb, S. P.; Gordon, M. S. *J. Phys. Chem. A* **1999**, *103*, 1265-1273.

(34)　Bandyopadhyay, P.; Gordon, M. S. *J. Chem. Phys.* **2000**, *113*, 1104-1109.

(35)　Day, P. N.; Pachter, R.; Gordon, M. S.; Merrill, G. N. *J. Chem. Phys.* **2000**, *112*, 2063-2073.

(36)　Bandyopadhyay, P.; Gordon, M. S.; Mennucci, B.; Tomasi, J. *J. Chem. Phys.* **2002**, *116*, 5023-5032.

(37)　Adamovic, I.; Gordon, M. S. *J. Phys. Chem. A* **2005**, *109*, 1629-1636.

(38)　Mullin, J. M.; Gordon, M. S. *J. Phys. Chem. B* **2009**, *113*, 8657-8669.

(39)　Mullin, J. M.; Gordon, M. S. *J. Phys. Chem. B* **2009**, *113*, 14413-14420.

(40)　DeFusco, A.; Minezawa, N.; Slipchenko, L. V.; Zahariev, F.; Gordon, M. S. *J. Phys. Chem. Lett.* **2011**, *2*, 2184-2192.

(41)　Netzloff, H. M.; Gordon, M. S. *J. Chem. Phys.* **2004**, *121*, 2711-2714.

(42)　Kina, D.; Nakayama, A.; Noro, T.; Taketsugu, T.; Gordon, M. S. *J. Phys. Chem. A* **2008**, *112*, 9675-9683.

(43)　Kina, D.; Arora, P.; Nakayama, A.; Noro, T.; Gordon, M. S.; Taketsugu, T. *Int. J. Quantum Chem.* **2009**, *109*, 2308-2318.

(44)　Atadinc, F.; Gunaydin, H.; Ozen, A. S.; Aviyente, V. *Int. J. Chem. Kinet.* **2005**, *37*, 502-514.

(45)　Ferreira, D. E. C.; Florentino, B. P. D.; Rocha, W. R.; Nome, F. *J. Phys. Chem. B* **2009**, *113*, 14831-14836.

(46)　Bandyopadhyay, P. *Theor. Chem. Acc.* **2008**, *120*, 307-312.

(47)　Kemp, D. D.; Gordon, M. S. *J. Phys. Chem. A* **2005**, *109*, 7688-7699.

(48) Kemp, D. D.; Gordon, M. S. *J. Phys. Chem. A* **2008**, *112*, 4885-4894.

(49) Merrill, G. N.; Webb, S. P. *J. Phys. Chem. A* **2003**, *107*, 7852-7860.

(50) Merrill, G. N.; Webb, S. P.; Bivin, D. B. *J. Phys. Chem. A* **2003**, *107*, 386-396.

(51) Merrill, G. N.; Webb, S. P. *J. Phys. Chem. A* **2004**, *108*, 833-839.

(52) Merrill, G. N.; Fletcher, G. D. *Theor. Chem. Acc.* **2008**, *120*, 5-22.

(53) Chandrakumar, K. R. S.; Ghanty, T. K.; Ghosh, S. K.; Mukherjee, T. *J. Mol. Struct.: THEOCHEM* **2007**, *807*, 93-99.

(54) Petersen, C. P.; Gordon, M. S. *J. Phys. Chem. A* **1999**, *103*, 4162-4166.

(55) Yoshikawa, A.; Morales, J. A. *J. Mol. Struct.: THEOCHEM* **2004**, *681*, 27-40.

(56) Balawender, R.; Safi, B.; Geerlings, P. *J. Phys. Chem. A* **2001**, *105*, 6703-6710.

(57) Safi, B.; Balawender, R.; Geerlings, P. *J. Phys. Chem. A* **2001**, *105*, 11102-11109.

(58) Day, P. N.; Pachter, R. *J. Chem. Phys.* **1997**, *107*, 2990-2999.

(59) Song, J.; Gordon, M. S.; Deakyne, C. A.; Zheng, W. *J. Phys. Chem. A* **2004**, *108*, 11419-11432.

(60) Sok, S.; Willow, S. Y.; Zahariev, F.; Gordon, M. S. *J. Phys. Chem. A* **2011**, *115*, 9801-9809.

(61) De Silva, N.; Willow, S. Y.; Gordon, M. S. *J. Phys. Chem. A, in press. DOI: 10.1021/jp402999p*

(62) De Silva, N.; Minezawa, N.; Gordon, M. S. *J. Phys. Chem. B, in press. DOI: 10.1021/jp404686c*

(63) Slipchenko, L. V.; Gordon, M. S. *J. Phys. Chem. A* **2009**, *113*, 2092-2102.

(64) Pruitt, S. R.; Steinmann, C.; Jensen, J. H.; Gordon, M. S. *J. Chem. Theory Comput.* **2013**, *9*, 2235-2249.

(65) Adamovic, I.; Gordon, M. S. *J. Phys. Chem. A* **2006**, *110*, 10267-10273.

(66) Adamovic, I.; Li, H.; Lamm, M. H.; Gordon, M. S. *J. Phys. Chem. A* **2006**, *110*, 519-525.

(67) Slipchenko, L. V.; Gordon, M. S. *J. Comp. Chem.* **2007**, *28*, 276-291.

(68) Smith, T.; Slipchenko, L. V.; Gordon, M. S. *J. Phys. Chem. A* **2008**, *112*, 5286-5294.

(69) Smith, Q. A.; Gordon, M. S.; Slipchenko, L. V. *J. Phys. Chem. A* **2011**, *115*, 4598-4609.

(70) Smith, Q. A.; Gordon, M. S.; Slipchenko, L. V. *J. Phys. Chem. A* **2011**, *115*, 11269-11276.

(71) Hands, M. D.; Slipchenko, L. V. *J. Phys. Chem. B* **2012**, *116*, 2775-2786.

(72) Pranami, G.; Slipchenko, L.; Lamm, M.; Gordon, M. Coarse-Grained Intermolecular Potentials Derived From The Effective Fragment Potential: Application To Water, Benzene, And Carbon Tetrachloride. In *Multi-scale Quantum Models for Biocatalysis*; York, D., Lee, T.-S., Eds.; Springer Netherlands, 2009; Vol. 7; pp 197-218.

(73) Flick, J. C.; Kosenkov, D.; Hohenstein, E. G.; Sherrill, C. D.; Slipchenko, L. V. *J. Chem. Theory Comput.* **2012**, *8*, 2835-2843.

(74) Amos, R. D.; Handy, N. C.; Knowles, P. J.; Rice, J. E.; Stone, A. J. *J. Phys. Chem.* **1985**, *89*, 2186-2192.

(75) Grimme, S. *J. Comput. Chem.* **2004**, *25*, 1463-1473.

(76) Grimme, S. *J. Comput. Chem.* **2006**, *27*, 1787-1799.

(77) Grimme, S.; Antony, J.; Ehrlich, S.; Krieg, H. *J. Chem. Phys.* **2010**, *132*, 154104-154119.

(78) Jurecka, P.; Cerny, J.; Hobza, P.; Salahub, D. R. *J. Comput. Chem.* **2007**, *28*, 555-569.

(79) Axilrod, B. M.; Teller, E. *J. Chem. Phys.* **1943**, *11*, 299-300.

(80) Gotch, A. J.; Zwier, T. S. *J. Chem. Phys.* **1992**, *96*, 3388.

(81) Gutowsky, H. S.; Emilsson, T.; Arunan, E. *J Chem Phys* **1993**, *99*, 4883.

(82) Suzuki, S.; Green, P. G.; Bumgarner, R. E.; Dasgupta, S.; Goddard, W. A.; Blake, G. A. *Science* **1992**, *257*, 942.

(83) Feller, D. *J. Phys. Chem. A* **1999**, *103*, 7558-7561.

Table 1. Water dimer center of mass to center of mass distance, R_e (Å), and interaction energy, D_e (kcal/mol), Coulomb (E^{Coul}), exchange repulsion (E^{Exrep}), polarization (E^{Pol}), charge transfer (E^{CT}), and dispersion (E^{Disp}) using the 6-311++G(3df,2p) basis set. The interaction energies without the dispersion energies (without the −D corrections) are given in parentheses.

HF//HF	R_e	D_e	E^{Coul}	E^{Exrep}	E^{Pol}	E^{CT}	E^{Disp}
QM − QM[a]	3.04	− 4.73 (− 3.93)	− 6.58	4.10	− 0.87	− 0.95	− 0.80
QM − EFP1[b]	2.97	− 5.90 (− 5.09)	− 7.81	3.95	− 1.25		− 0.81
EFP1 − QM[c]	3.05	− 5.10 (− 4.30)	− 6.21	2.43	− 0.52		− 0.80
EFP1 − EFP1[d]	3.00	− 5.89 (− 5.10)	− 6.67	2.17	− 0.60		− 0.80
EFP2 − EFP2[e]	3.00	− 6.31	− 9.82	7.41	− 1.59	− 0.62	− 1.69
MP2//MP2							
QM − QM[a]	2.91	− 5.32					

[a] Both water molecules are treated as QM.

[b] The hydrogen donor is treated as QM and the hydrogen acceptor is treated as EFP1.

[c] The hydrogen donor is treated as EFP1 and the hydrogen acceptor is treated as QM.

[d] Both water molecules are treated as EFP1.

[e] Both water molecules are treated as EFP2.

Table 2. The benzene-water center of mass to center of mass intermolecular, R_e (Å), and the interaction energy, D_e (kcal/mol), Coulomb (E^{Coul}), exchange repulsion (E^{Exrep}), polarization (E^{Pol}), charge transfer (E^{CT}), and dispersion (E^{Disp}) using the 6-311++G(3df,2p) basis set. The interaction energies without the dispersion energies (without the −D corrections) are given in parentheses.

HF//HF	R_e	D_e	E^{Coul}	E^{Exrep}	E^{Pol}	E^{CT}	E^{Disp}
QM − QM[a]	3.70	− 3.76 (− 1.81)	− 2.15	1.02	− 0.43	− 0.28	− 1.95
QM − EFP1[b]	3.66	− 4.73 (− 2.69)	− 3.02	0.65	− 0.32		− 2.04
EFP2 − EFP2[c]	3.21	− 4.68	− 4.88	4.66	− 1.23	− 0.34	− 2.89
MP2//MP2							
QM − QM[a]	3.26	− 4.32					

[a] Both benzene and water molecules are treated as QM.

[b] The benzene molecule is treated as QM and the water molecule is treated as EFP1.

[c] Both benzene and water molecules are treated as EFP2.

Table 3. The center of mass to center of mass distance between benzene and the eight-water cluster, R_e (Å), and the interaction energy, D_e (kcal/mol), Coulomb (E^{Coul}), exchange repulsion (E^{Exrep}), polarization (E^{Pol}), charge transfer (E^{CT}), and dispersion (E^{Disp}) using the 6-311++G(3df,2p) basis set. The interaction energies without the dispersion energies (without the −D corrections) are given in parentheses.

HF//HF	R_e	D_e	E^{Coul}	E^{Exrep}	E^{Pol}	E^{CT}	E^{Disp}
QM − QM[a]	6.25	− 4.58 (− 2.09)	− 2.25	0.80	− 0.28	− 0.56	− 2.49
QM − EFP1[b]	6.25	− 6.73 (− 4.23)	− 3.10	0.70	− 0.27		− 2.50
EFP2 − EFP2[c]	5.49	− 6.68	− 7.18	8.68	− 2.93	− 0.55	− 4.69
MP2//MP2							
QM − QM[a]	5.28	− 6.44					

[a] Both benzene and eight water molecules are treated as QM.

[b] The benzene molecule is treated as QM and the eight water molecule are treated as EFP1.

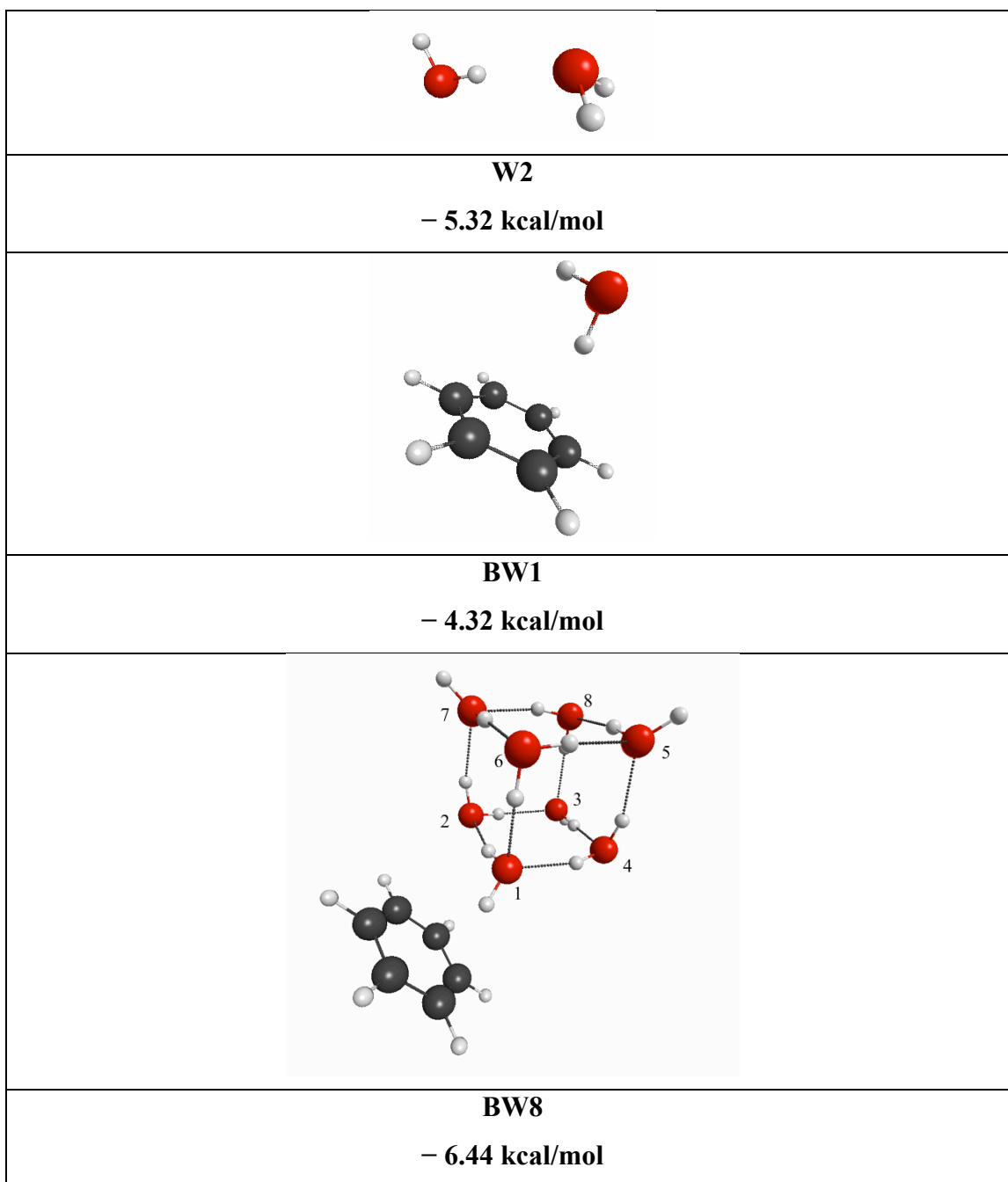[c] Both benzene and eight water molecules are treated as EFP2.

Figure 1. MP2/6-311++G(3df,2p) optimized structures of water dimer (W2), benzene with one water (BW1), and benzene with eight water (BW8) complexes. The interaction energies between solute and solvent complexes are given in kcal/mol. For the W2 case, the "left" molecule is the hydrogen donor and "right" molecule is the hydrogen acceptor. In the BW8 complex the water molecules are labeled 1 through 8.

CHAPTER 7. GENERAL CONCLUSIONS

In chapter 2, theoretical study of anharmonic molecular vibrations and binding energies of Li^+–H_2, Na^+–H_2, B^+–H_2 and Al^+–H_2 complexes using the VSCF method corrected for second order perturbation theory have been presented. The CCSD(T) red shifts and the predicted M^+–H_2 binding energies are in excellent agreement with the experimental values. The unusual relationship between the experimentally observed binding energies and red shifts in the H–H vibrational frequencies is also well reproduced by theory. The fact that the trends in the red shifts do not reflect the binding energy trends is interpreted, using the SAPT method, in terms of a balance between opposing attractive and repulsive interactions.

The anharmonic corrections to the harmonic frequencies are rather different for the three vibrational modes in these M^+–H_2 complexes. For example, the ratio of the VSCF-PT2/harmonic frequencies is 0.94 for the H-H stretch, while this ratio ranges from 0.74 to 0.86 for the symmetric stretch vs. 0.87 to 0.94 for the antisymmetric stretch. This means that one universal scaling factor to scale the harmonic frequencies would not capture the actual anharmonicity that is present in the complexes. So, while calculating VSCF frequencies is more computationally challenging than employing a simple scale factor, the VSCF approach is more accurate.

In chapter 3, The PT2-VSCF approach is employed at the CCSD(T) level of theory to compute the vibrational spectrum of $Li^+–(H_2)_n$ complexes, for $n = 1,2,3$. The H_2 subunits are predicted to be weakly bound (~5 kcal/mol) to the lithium cation. The strength of the metal–H_2 complex interaction mainly depends on the number of H_2 subunits attached to the metal cation, where the interaction decreases with increasing n. The calculated H–H frequency red shifts are in good agreement with the available experimental data. The downward shifts of the H–H frequency are correlated with the complexation energy per H_2. The H–H stretching frequency varies according to the delocalization of the H–H electron density toward the metal cation and the consequent weakening of the H–H bond, compared to the frequency of the isolated H_2 molecule. The amount of delocalization of the electron density per H_2 subunit towards the metal cation decreases with n, resulting in a less red-shifted H–H stretching frequency.

In the $Li^+–(H_2)_n$ complexes ($n = 1,2,3$), the modest 5 kcal/mol interaction energy might be suitable for a hydrogen storage system with favorable H_2 loading and unloading kinetics. In order to load or unload the H_2 to/from the Li^+, one needs pay attention to the Li^+–H stretching modes. Among the Li^+–H stretching modes, the most IR active modes (v_3 of Li^+–H_2, v_5 of Li^+–$(H_2)_2$, and degenerate v_7 and v_8 of Li^+–$(H_2)_3$), are responsible for dissociation of an H_2 from the Li^+ Therefore, one might increase the temperature or provide the correct amount of energy to the most IR active Li^+–H stretching modes in order to release H_2 and vice versa.

In chapter 4, four different levels of theory CIS, EOM-CCSD, CR-EOMCCSD(T), and TDDFT (PBE0 functional) with cc-pVDZ basis set is used to study the explicit solvent effect on the electronic spectra for the of $HCONH_2$:$n(H_2O)$ and NMA:$n(H_2O)$ complexes (n = 1~3). These computational results provide the *qualitative* interpretation of the solvent effects on the electronic absorption spectra of amides. In addition, the simulated electronic spectra are calculated through the QM/EFP1 MD simulation combined with TDDFT/EFP1. The calculated water solvent effect on the $n{\rightarrow}\pi^*$ and $\pi_{nb}{\rightarrow}\pi^*$ vertical excitations exhibits *quantitative* blue and red -shifts in the amides, which are consistent with the experimental observation.

The schematic energy level diagrams are used to understand the solvent induced blue and red -shift vertical excitation of the amides. In summary, the physical origin of the solvent effect on $n{\rightarrow}\pi^*$ (blue-shift) and $\pi_{nb}{\rightarrow}\pi^*$ (red-shift) vertical excitations of amides could be understood as how the energies of occupied molecular orbitals are changed relative to that of the π^* due to stabilizing (or destabilizing) electronic interaction of water with the electronic densities of the amides.

In chapter 5, the theoretical study of the ground state and excited state tautomerization reaction in C456 have been presented, using PBE0/DH(d,p) and TDPBE0/DH(d,p), respectively. The transition states of the hydrogen atom transfer reaction was found in C456:$3H_2O$, C456:$3H_2O$ with PCM as well as C456:$3H_2O$ with small clusters of EFP waters. The optimized geometries of the corresponding tautomers

were also presented. The TDPBE0/DH(d,p) ESP-derived charges along the excited state IRC path predicts that the tautomerization reaction is a hydrogen atom transfer reaction, with hydrogen partial charges ~0.55 e. The predicted activation energies are in excellent agreement with the experimental evidences. The addition of water molecules to C456 assists the hydrogen atom transfer reaction by decreasing the activation energy in the excited state.

The results in the present work have also been compared with the previous theoretical data reported by Georgieva, *et al.* on the C456:3H$_2$O system. They have considered the S_1 enol to keto tautomerization as a proton transfer reaction; the barrier height was estimated to be 17-20 kcal/mol at the TDB3LYP/SVPD level of theory. In the present paper, the S_1 enol to keto tautomerization of C456:3H$_2$O was interpreted as a hydrogen atom transfer reaction (not a proton transfer reaction) and the TDPBE0/DH(d,p) barrier height was calculated to be 10.15 kcal/mol (5.30 kcal/mol activation energy).

In chapter 6, presents a study of water−water (W2) and benzene−water (BW1 and BW8) complexes based on the both *ab initio* and effective fragment potential method. The binding energies in the clusters were evaluated at the HF and MP2 levels of theory with the 6-311++G(3df,2p) basis set. The binding energies also were computed with all possible QM−EFP and EFP−EFP arrangements. The dispersion correction to the

QM−EFP1 interaction was introduced empirically and compared to the interaction energies of more general and highly accurate EFP2−EFP2.

The absolute difference in the interaction energies between HF−D (QM−QM) and MP2 (QM−QM) is 0.6 kcal/mol for W2, 0.6 kcal/mol for BW1, and 1.9 kcal/mol for BW8. Interestingly, the absolute difference in the interaction energies between QM−EFP1−D and EFP2−EFP2 is 0.4 kcal/mol for W2, 0.1 kcal/mol for BW1, and 0.1 kcal/mol for BW8. This means that the accuracy of the simple QM−EFP1−D method provides interaction energies that are almost equivalent to the more sophisticated EFP2−EFP2 approach for the dispersion dominant complexes such as benzene-water complexes. It is gratifying that the agreement between HF−EFP1−D and EFP2 for the complexes studied here is slightly better than the agreement between HF−D and MP2 for the same complexes.